Astronomy Letters, Vol. 30, No. 12, 2004, pp. 803–815. Translated from Pis'ma v Astronomicheskiĭ Zhurnal, Vol. 30, No. 12, 2004, pp. 883–896.

A Hydrodynamic Model for Asymmetric Explosions of Rapidly Rotating Collapsing Supernovae with a Toroidal Atmosphere

V. S. Imshennik and K. V. Manukovskii*

Institute for Theoretical and Experimental Physics, ul. Bol'shaya Cheremushkinskaya 25, Moscow, 117259 Russia

Received June 28, 2004

Abstract—We numerically solved the two-dimensional axisymmetric hydrodynamic problem of the explosion of a low-mass neutron star in a circular orbit. In the initial conditions, we assumed a nonuniform density distribution in the space surrounding the collapsed iron core in the form of a stationary toroidal atmosphere that was previously predicted analytically and computed numerically. The configuration of the exploded neutron star itself was modeled by a torus with a circular cross section whose central line almost coincided with its circular orbit. Using an equation of state for the stellar matter and the toroidal atmosphere in which the nuclear statistical equilibrium conditions were satisfied, we performed a series of numerical calculations that showed the propagation of a strong divergent shock wave with a total energy of $\sim 0.2 \times 10^{51}$ erg at initial explosion energy release of $\sim 1.0 \times 10^{51}$ erg. In our calculations, we rigorously took into account the gravitational interaction, including the attraction from a higher-mass ($1.9M_\odot$) neutron star located at the coordinate origin, in accordance with the rotational explosion mechanism for collapsing supernovae. We compared in detail our results with previous similar results of asymmetric supernova explosion simulations and concluded that we found a lower limit for the total explosion energy.

Key words: *plasma astrophysics, hydrodynamics, shock waves.*

INTRODUCTION AND FORMULATION OF THE HYDRODYNAMIC PROBLEM

We previously solved the two-dimensional axisymmetric problem of the formation of a toroidal atmosphere during the collapse of the rotating iron core and outer layers of a high-mass star by a numerical method identical to that used here (Imshennik *et al.* 2003). Our numerical calculations demonstrated the stability of the formed hydrostatically equilibrium toroidal atmosphere on characteristic hydrodynamic time scales: the calculations were performed up to times much longer than the hydrodynamic time of the problem (the final time of the main calculation is $t_{\rm f} = 29.034$ s, while the characteristic hydrodynamic time is $t_{\rm hd} = 0.517$ s). Our calculations on finer computational meshes (the number of mesh points in all directions was increased by factors of 1.5 and 2) revealed the possibility of the sporadic fragmentation of this atmosphere even after a hydrostatic equilibrium was established. The fragmentation found took place once over the entire computational time and led only to a minor mass loss by the atmosphere. This fragmentation is most likely attributable to a restructuring of the toroidal atmosphere that results in its being roughly isentropic. This property of the atmosphere ($\nabla S \simeq 0$) and the distribution of specific angular momentum in it (which satisfies the condition $\partial j^2/\partial \tilde{r} > 0$, where $\tilde{r}$ is the cylindrical radius) derived previously (Imshennik *et al.* 2003) are necessary and sufficient conditions for the Viertoft–Lebowitz dynamical stability criterion to be fulfilled (Tassoul 1978). All of this allows the toroidal atmosphere obtained previously (Imshennik *et al.* 2003) to be deemed a long-lived structure with a total lifetime that is comparable, at least, to the evolution time of a neutron-star binary ($\gtrsim$1 h) considered in the context of a rotational explosion mechanism for collapsing supernovae (Imshennik and Popov 1994; Imshennik and Ryazhskaya 2004).

Recall that the rotational mechanism implies a crucial role of the rotation effects in explaining the explosions of collapsing supernovae (Imshennik 1992). As was roughly estimated by Aksenov *et al.* (1997), for high-mass ($M > 10M_\odot$) main-sequence stars, the equatorial rotational velocities of their iron cores at the final stages of their existence could be close

*E-mail: manu78@inbox.ru

in magnitude to the parabolic velocity. In the presence of such fast rotation, the iron core collapses to form a rapidly rotating protoneutron star that is generally unstable against the quadrupole dynamical rotational mode $m = 2$ (Aksenov *et al.* 1995) or, in other words, against its fragmentation. The neutron-star binary formed through such fragmentation (in the simplest case) evolves due to the losses of energy and angular momentum via the emission of gravitational waves, and the orbit of the binary becomes circular by the time the low-mass companion fills its Roche lobe almost independently of the initial eccentricity of the binary (Imshennik and Popov 1994). The filling of a Roche lobe with known characteristics (Paczynski 1971) leads to intense mass transfer from the less massive component to the more massive component of a neutron star binary that ends with the explosive destruction of the light component when it reaches the minimum possible neutron star mass, $\simeq 0.1 M_\odot$ (Blinnikov *et al.* 1984, 1990; Colpi *et al.* 1989, 1991, 1993). It should be emphasized that the process of mass transfer in a neutron star binary, which was considered in detail by Imshennik and Popov (1998), was simplified by using the so-called conservative approximation in which the possible formation of an accretion disk around the high-mass component was disregarded (Imshennik and Popov 2002). The existence of such an accretion disk during the mass transfer between the components of the binary under consideration was recently analyzed by Colpi and Wasserman (2002). Based on the standard theory of such disks in close binaries (see Lubow and Shu 1975; Bildsten and Cutler 1992), they modeled the evolution of a close neutron star binary in the opposite limiting case where all of the matter from the low-mass component is transferred to the accretion disk rather than is attached to the high-mass component. In the absence of reliable data on the characteristic dissipative disk destruction times, the analysis by Colpi and Wasserman (2002) is certainly of great interest. It not only does not restrict the rotational explosion mechanism for collapsing supernovae, but also enhances its capabilities through the emergence of a new scenario with earlier fragmentation of the rotating collapsar.

Taking into account the aforesaid, we formulate below the axisymmetric hydrodynamic problem of the explosion of the low-mass component in a neutron-star binary that moves in a circular orbit in the presence of a rotating, hydrostatically equilibrium toroidal atmosphere with previously determined parameters (Imshennik *et al.* 2003). Below, we arbitrarily call the higher-mass component of the binary a pulsar (p) by also taking into account the possibility that this component turns into a black hole, which is not fundamentally important from the viewpoint of the problem considered here. The parameters of circular orbits in a binary are defined by Kepler's simple formulas. Thus, the orbital velocity of the low-mass neutron star (ns) is (Aksenov *et al.* 1997)

$$V_{\rm ns} = \frac{m_{\rm p}}{M_{\rm t}}(GM_{\rm t})^{1/2}a^{-1/2}, \quad (1)$$

where $M_{\rm t} = m_{\rm p} + m_{\rm ns}$ is the total mass of the binary, $m_{\rm p}$ is the mass of the pulsar, $m_{\rm ns}$ is the mass of the low-mass neutron star, and a is the separation between the components. It is convenient to express the basic parameters of the problem in terms of the pulsar's velocity $V_{\rm p}$, which should be considered an observable parameter (Aksenov *et al.* 1997). The separation between the components is then

$$a = \left(\frac{m_{\rm ns}}{M_{\rm t}}\right)^2 \frac{GM_{\rm t}}{V_{\rm p}^2}. \quad (2)$$

The velocity and orbital radius of the low-mass neutron star can be determined from (1) and (2) and the obvious equality between the orbital periods of the two binary components

$$\frac{V_{\rm ns}}{V_{\rm p}} = \frac{a_{\rm ns}}{a_{\rm p}} = \frac{m_{\rm p}}{m_{\rm ns}}. \quad (3)$$

We take the results of the main numerical calculation from our previous paper (Imshennik *et al.* 2003) as the model of a toroidal atmosphere. This calculation was performed in a spherical layer whose inner boundary, as can be easily verified, is located along the radius outside the region of space occupied by the neutron star binary. The toroidal atmosphere computed previously (Imshennik *et al.* 2003) definitely lies outside this region. We also took the total mass of the binary $M_{\rm t}$ from this calculation; the sum of the masses of the protoneutron star embryo ($\sim 1 M_\odot$) and the matter accreted through the inner computational boundary onto this embryo over the formation time of the toroidal atmosphere should be taken as this mass. Meeting this requirement ensures an approximate satisfaction of the hydrostatic equilibrium conditions for the toroidal atmosphere. To completely determine the parameters of the binary, it remains only to specify the pulsar's velocity and the relationship between the masses of the pulsar and its lighter companion.

A similar problem of the explosion of a low-mass neutron star was studied by Aksenov *et al.* (1997) and Imshennik and Zabrodina (1999). Nevertheless, these studies had a number of fundamental differences from the problem considered here. First, there is a difference in the formulations of the hydrodynamic problem, although the numerical simulations are two-dimensional and axisymmetric in both cases. In the papers mentioned above, the axis of symmetry of the problem coincided with the velocity vector of the rotating low-mass neutron star in a circular orbit at the time of its explosion. The gravitational interaction was completely ignored. Clearly, the latter assumptions are asymptotically valid at distances $r \gg a$. Aksenov *et al.* (1997) interpreted this formulation of the problem as the artificial turn of the velocity direction for the exploding star through $\pi/2$, and the estimates obtained confirmed that the gravitational interaction effects were negligible. However, these effects could be rigorously taken into account only in the three-dimensional formulation of the problem (see the next section), although, as was noted above, the problem asymptotically becomes two-dimensional at $r \gg a$. In this paper, as in the preceding paper on the formation of a toroidal atmosphere, we also use the two-dimensional axisymmetric approximation, but the axis of symmetry coincides with the axis of orbital rotation of the neutron star binary (rather than being perpendicular to it!). In this formulation of the problem, the only way of reducing the fundamentally three-dimensional problem of the explosion of a low-mass neutron star to a two-dimensional problem is to "spread" the rotating neutron star over its orbit or, in other words, to represent it as an exploding torus with a circular cross section. In fact, as Aksenov's preliminary calculations show,[1] the light component of the binary traverses less than a quarter of the orbital circumference since the onset of destruction before leaving it. It may be asserted that replacing the low-mass neutron star with an exploding torus is a forced, but quite relevant approximation, especially since a significant difference of this work is the direct allowance for the pulsar's gravitational influence, along with the allowance for the self-consistent gravitational field produced by the distributed matter throughout the computational region by directly solving the Poisson equation (see below). As was noted above, Aksenov *et al.* (1997) and Imshennik and Zabrodina (1999) disregarded the gravitational interaction in their numerical solution.

Another significant difference of the hydrodynamic problem in question from the previous problems is the use of spherical coordinates, whereas the above authors performed their numerical calculations in cylindrical coordinates. In addition, Aksenov *et al.* (1997) used computational meshes of two types, adaptive (LM) and fixed (PPM), to mutually check the accuracy, while Imshennik and Zabrodina (1999) used only adaptive (LM) meshes, which are recognized to be more adequate. Finally, matter with the simplest (uniform) density distribution was located on the path of the divergent shock wave in the above papers. In this paper, a toroidal atmosphere with a nonuniform density distribution was naturally located on the path of the shock wave.

[1] We are grateful to A.G. Aksenov for this private communication.

INITIAL CONDITIONS: THE HYDRODYNAMIC MODEL

At the end of the numerical solution ($t_\mathrm{f} = 29.034$ s), the toroidal atmosphere obtained previously (Imshennik *et al.* 2003) (the main calculation [1]) had the following parameters (see Table 3 in the above paper): the maximum density is $\rho_\mathrm{max} = 0.396 \times 10^7$ g cm^{-3}, the position of the density maximum is a point on the equator (in the cylindrical ($\tilde{r}$, z) coordinate plane) with a radius of $\tilde{r}_\mathrm{max} = 0.955 \times 10^8$ cm, and the total mass of the atmosphere is $M_\mathrm{atm} = 0.117 M_\odot$. The inner computational boundary in calculation [1] was located at a spherical radius of $r^*_\mathrm{min} = 0.876 \times 10^8$ cm, which, as was shown previously (Imshennik *et al.* 2003), may be considered as the inner boundary of the toroidal atmosphere. The mass of the matter located below the radius r^*_min (outside the computational region) at the final time t_f was $M_\mathrm{in} = M_\mathrm{t} = 1.931 M_\odot$. Note that M_t agrees well with the typical iron core masses of high-mass stars, M_Fe ($1.2M_\odot < M_\mathrm{Fe} < 2M_\odot$), and surprisingly closely matches the value of $M_\mathrm{t} = 1.9 M_\odot$ used by Aksenov *et al.* (1997).

For the pulsar's velocity V_p, we take a reasonable value (Lyne and Lorimer 1994):

$$V_\mathrm{p} = 1000 \text{ km s}^{-1}. \qquad (4)$$

We take the mass of the exploding torus (the low-mass neutron star at the time of its destruction) from Aksenov *et al.* (1997); i.e., we assume that $m_\mathrm{ns} = 0.1 M_\odot$. According to (2), the separation between the components of the binary is then $a = 6.98 \times 10^7$ cm ≈ 700 km, which is below identified with the orbital radius of the low-mass neutron star: $a_\mathrm{ns} = a$. The radius of the torus r_t can be determined by assuming that the volumes of the neutron star (a sphere of radius r_0) and the torus with a circular cross section (in the approximation $r_\mathrm{t} \ll a$) are equal:

$$V_\mathrm{torus} \simeq 2\pi a \pi r_\mathrm{t}^2 = \frac{4}{3}\pi r_0^3. \qquad (5)$$

As r_0, Aksenov *et al.* (1997) took $0.1 R_\mathrm{Fe}$, where $R_\mathrm{Fe} = 4.38 \times 10^8$ cm is the initial radius of the iron core. The radius of the circular torus is then

$$r_\mathrm{t} = \left(\frac{2r_0^3}{3\pi a}\right)^{1/2} = 1.60 \times 10^7 \text{ cm} = 160 \text{ km}. \qquad (6)$$

It thus follows that the low-mass neutron star considered in the form of a circular torus at the onset of its explosion is contained within a sphere with a radius of $\sim$860 km, which is slightly smaller than the radius of the inner boundary of the toroidal atmosphere identified above with the radius of the computational region $r^*_{\rm min}$ (Imshennik *et al.* 2003). Apart from the representation of the low-mass neutron star as a torus, we assume that the higher-mass component of the binary (a pulsar) is at the coordinate origin, i.e., $a_{\rm p} = 0$, which naturally agrees with the above equality $a_{\rm ns} = a$. An additional justification for this assumption is the strong inequality $V_{\rm p}/V_{\rm ns} = a_{\rm p}/a_{\rm ns} = 1/18 \approx 0.0556 \ll 1$, as implied by (3). The satisfaction of the hydrostatic equilibrium condition for a circular torus in the gravitational field of a stationary pulsar is also appropriate in the initial conditions for the hydrodynamic problem under consideration. This requires determining the velocity of the low-mass neutron star using the formula $V_{\rm ns} = (Gm_{\rm p}/a)^{1/2}$, which yields 18.5×10^3 instead of 18×10^3 km s^{-1} obtained from (3) and (4).

It is pertinent to independently estimate the gravitational interaction between the matter of the exploded low-mass neutron star and the higher-mass component. This can be done by following the three-dimensional model in the dust approximation by Colpi and Wasserman (2002) in the limit $m_{\rm ns} \ll m_{\rm p}$ that holds in the case under consideration. According to these authors, the pulsar's kick velocity is

$$V_{\rm kick} = \eta \frac{m_{\rm ns}}{m_{\rm p}} V_{\rm expl},$$

where $V_{\rm expl} = 18.5 \times 10^3$ km s^{-1} is the orbital velocity of the exploded star with respect to the center of inertia, $\eta = \eta(w_0')$ is the gravitational deceleration coefficient, and $w_0' = w_0/(Gm_{\rm p}/a)^{1/2}$ with $w_0 = (2E_0/m_0)^{1/2} = 3.01 \times 10^9$ cm s^{-1} at $E_0 = 4.7$ MeV/nucleon ($m_0 = 1.66 \times 10^{-24}$ g). At $m_{\rm p} = 1.8M_\odot$ and $a = 7 \times 10^7$ cm, $w_0' = 1.63$ and, accordingly, $\eta = 0.73$ (see Fig. 1 from Colpi and Wasserman 2002). It thus immediately follows that $V_{\rm kick} = 750$ km s^{-1} instead of $V_{\rm kick} = 1000$ km s^{-1} from (4). Thus, the initial kick velocity of the pulsar decreases, although only slightly, and still agrees with the observational data on the high velocities of pulsars (Lyne and Lorimer 1994).

Let us consider the choice of initial conditions in the region of energy release in more detail. This question was discussed in detail by Imshennik and Zabrodina (1999) and Zabrodina and Imshennik (2000), who made important refinements. In their hydrodynamic calculation of the explosive destruction of a self-gravitating neutron star with a critical mass, Blinnikov *et al.* (1990) obtained the internal energy of the explosion products, $E_0 = 4.70$ MeV/nucleon $= 4.5 \times 10^{18}$ erg g^{-1}. Below, we use this value as the basis for determining the specific energy release[2]. According to the equation of state used here (see the next section), part of the internal energy of the matter is contained in the rest energy of the nuclides (if the iron mass fraction $X_{\rm Fe}$ is less than unity). Below, the specific internal energy minus this part is denoted by e_0. In addition, E_0 can decrease appreciably due to neutrino radiation and allowance for the final times of β-processes. Therefore, it is appropriate to use ξE_0, where $\xi \leq 1$ is the explosion attenuation coefficient, in place of E_0. Formally, this coefficient may be set larger than unity ($\xi > 1$), bearing in mind the possibility of errors in the quantity E_0 itself in the cited paper. Such cases will also be presented below. The coefficient α that specifies the initial value of the specific internal energy of the matter in the region of energy release introduced above, $e_0 = \alpha E_0$, can then be estimated using the formula (Zabrodina and Imshennik 2000)

$$\alpha = \xi - 2.012(1 - X_{\rm Fe}) + 1.654X_{\rm He} + 0.2771X_{\rm p}, \tag{7}$$

where $X_{\rm Fe}$, $X_{\rm He}$, and $X_{\rm p}$ are the mass fractions of $^{56}_{26}$Fe, $^4_2$He, and protons, respectively, which are known functions of the thermodynamic quantities e_0 and ρ_0. For $X_{\rm Fe} = 1$ ($X_{\rm He} = X_{\rm p} = 0$), we obtain $\alpha = \xi$ from (7), as would be expected. Thus, to find the initial thermodynamic state of the low-mass neutron star, we must determine the coefficient $\alpha = \alpha(\xi, e_0, \rho_0)$ using (7) by numerically solving the equation

$$e_0 = \alpha(\xi, e_0, \rho_0)E_0. \tag{8}$$

Under the assumption of a uniform initial density distribution over the entire circular torus of mass $m_{\rm ns} = 0.1M_\odot$ with the parameters a and $r_{\rm t}$ specified above, i.e., for the mean density $\rho_0 = 5.66 \times 10^8$ g cm^{-3} and the coefficient $\xi = 1$, Eq. (8) yields the initial internal energy of the neutron star matter $e_0 = 3.14 \times 10^{18}$ erg g^{-1} (see Table 1), which determines all of the remaining initial-state parameters for the region of energy release (the first column). This result was previously obtained by Zabrodina and Imshennik (2000) (see the table in the cited paper) and, naturally, closely matches the above value of e_0 for the equation of state used in this paper. For a uniform distribution of the density and other thermodynamic parameters, the total internal energy of the neutron star is $\varepsilon_0 = e_0 m_{\rm ns} = \alpha m_{\rm ns} E_0$. For a nonuniform distribution, it

[2]It should be borne in mind that the equation of state in the cited paper was a simple interpolation between the equation of state for cold catalyzed matter $P_0(\rho)$ and $E_0(\rho)$ (Baym *et al.* 1971) and the equation of state for an ideal gas as a temperature additive in place of the equation of state for nonideal nuclear matter with a nonzero temperature (Lattimer and Swesty 1989).

was obtained by integration over the entire volume of the torus, which pertains to the second and third columns in Table 1.

For the subsequent numerical solution, we had to fill the space of the iron-core cavity around the exploded neutron star (down to the radius $r^*_{\min}$) with low-density (10^6 g cm^{-3}) matter. To reduce the initial jump in density that arises in this case at the contact discontinuity between the explosion products and the matter of the iron-core cavity, the initial distribution of thermodynamic quantities was smoothed out near the boundary of the circular torus within which the density distribution became nonuniform. To keep the total mass of the low-mass neutron star constant ($m_{\rm ns} = 0.1M_\odot$), the central density of the circular torus was artificially increased by a factor of 1.5 ($\rho_0' = 8.36 \times 10^8$ g cm^{-3}). Naturally, this entailed changes in other initial parameters in the region of energy release. This set of, strictly speaking, central parameters (with the same e_0) was chosen as the initial state of the exploding neutron star in the main calculation (the second column in Table 1). A comparison of the first two columns in Table 1 shows that the mass fractions of the nuclides $X_{\rm Fe}$, $X_{\rm He}$, $X_{\rm p}$, and $X_{\rm n}$ were almost identical, while the parameters α and ξ, which characterize the degree of energy release, proved to be equal to their previous values, to within small corrections. The initial pressure P_0 and temperature T_0 are slightly higher in the second column. Nevertheless, the total internal energy of the neutron star in the case under consideration proved to be even slightly lower ($\varepsilon_0 = 0.53 \times 10^{51}$ erg). As a result, these changes in the initial conditions of the problem seem negligible.

The third column of Table 1 gives a set of initial parameters for the formal case $\xi = 1.84$ (the case of highly overestimated initial energy release with $\xi E_0 = 8.28 \times 10^{18}$ erg g^{-1}), which was used in our auxiliary calculation (see "Discussion of Numerical Results"). In this case, according to the chosen equation of state, the matter of the low-mass neutron star initially consists of predominantly helium and a small fraction of free neutrons, while the iron mass fraction $X_{\rm Fe}$ is equal to zero. In essence, this case ignores the expenditure of energy on overcoming the self-gravity of the exploding neutron star, but is still consistent with the total energy release during the recombination of neutron matter into iron, $E_0 \approx 9.2$ MeV/nucleon $= 8.8 \times 10^{18}$ erg g^{-1}.

THE METHOD OF NUMERICAL SOLUTION

When the explosion of a low-mass neutron star is modeled, the system of ideal hydrodynamic equations in the axisymmetric case ($\partial/\partial\varphi, g_\varphi = 0$) in spherical coordinates (r, θ, φ) that was described in detail previously (Imshennik *et al.* 2002) is solved numerically. We numerically solved the system of hydrodynamic equations using an algorithm that is based on the PPM method (Colella and Woodward 1984) and that is a modification of Godunov's method (Godunov *et al.* 1976). The method has been repeatedly described previously (see, e.g., Imshennik *et al.* 2002).

Table 1. Initial-state parameters for the region of energy release at various central densities ρ_0 and specific internal energies e_0

ξ	1.00	1.01	1.84
α	0.700	0.701	1.186
ε_0, 10^{51} erg	0.63	0.53	0.90
e_0, 10^{18} erg g^{-1}	3.14	3.14	5.31
ρ_0, 10^8 g cm^{-3}	5.66	8.36	8.36
T_0, 10^9 K	8.88	9.63	11.95
P_0, 10^{26} erg cm^{-3}	3.73	6.07	8.79
$X_{\rm Fe}$	0.385	0.370	0.000
$X_{\rm He}$	0.566	0.579	0.814
$X_{\rm n}$	4.65×10^{-2}	4.79×10^{-2}	0.123
$X_{\rm p}$	2.58×10^{-3}	2.95×10^{-3}	5.74×10^{-2}

The gravity $\mathbf{g} = \mathbf{g}_{\rm p} + \mathbf{g}_{\rm env}$ that acts on the matter in the problem under consideration is the sum of two parts: the first is attributable to the gravitational field of the pulsar placed exactly at the coordinate origin:

$$\mathbf{g}_{\rm p} = \left(-\frac{Gm_{\rm p}}{r^2}, 0, 0\right), \tag{9}$$

while the second is attributable to the gravitational field of the matter of the computational region, whose gravity is defined by the standard equation $\mathbf{g}_{\rm env} = -\nabla\Phi$, and the potential satisfies the Poisson equation

$$\Delta\Phi = 4\pi G\rho. \tag{10}$$

An efficient algorithm designed for use on stationary meshes in spherical coordinates is used to solve the Poisson equation (10) and to determine the gravity $\mathbf{g}_{\rm env}$. This algorithm is based on the expansion of the integral representation of the gravitational potential Φ in terms of associated Legendre polynomials (Aksenov 1999). In our calculations, the potential was expanded in terms of the first twenty associated Legendre polynomials. The necessary boundary condition for the gravitational potential, $\Phi \to -(GM)/r$ for $r \to \infty$, is automatically satisfied in this algorithm of solving the Poisson equation.

The matter over the temperature range under consideration is assumed to be a mixture of an ideal

Boltzmann gas of free nucleons n, p and nuclides $^4_2$He, $^{56}_{26}$Fe as well as an ideal Fermi–Dirac electron–positron gas together with equilibrium blackbody radiation. The equation of state is subject to the nuclear statistical equilibrium conditions with a fixed ratio of the mass fractions of the neutrons and protons, including those bound in the helium and iron nuclides, equal to 30/26. The specific internal energy of the matter is defined by the formula (see Eq. (9) from Imshennik and Zabrodina (1999))

$$e = e_- + e_+ + e_\mathrm{r} + e_\mathrm{id} + \left[\frac{Q_\mathrm{Fe} + 26\Delta Q_\mathrm{n}}{56m_0}(1 - X_\mathrm{Fe}) - \frac{Q_\mathrm{He} + 2\Delta Q_\mathrm{n}}{4m_0}X_\mathrm{He} - \frac{\Delta Q_\mathrm{n}}{m_0}X_\mathrm{p}\right], \tag{11}$$

where e_- and e_+ are the contributions of the electrons and positions to the internal energy of the matter, respectively; e_r is the contribution of the blackbody radiation; and e_id is the contribution of the ideal Boltzmann gas of nuclides. The expression in the brackets is the part of the internal energy of the matter that is contained in the rest energy of the nuclides and that has a direct bearing on the choice of an initial state for the exploding neutron star (see above). In the solution, the equation of state is tabulated, which increases appreciably the speed of the numerical method. In addition, the dependence of the matter pressure on density ρ and specific internal energy e is locally simulated by a binomial approximation (see, e.g., Imshennik *et al.* 2003).

The system of units from our previous paper (Imshennik *et al.* 2003) is used in the numerical solution. The numerical scales of the physical quantities in this system are

$$[r] = 10^8\ \mathrm{cm}, \quad [M] = 10^{32}\ \mathrm{g}, \tag{12}$$
$$[V_\mathrm{r}] = [V_\theta] = [V_\varphi] = 2.583 \times 10^8\ \mathrm{cm\ s^{-1}},$$
$$[c] = 7.958 \times 10^6\ \mathrm{g\ cm^{-3}}, \quad [t] = 3.871 \times 10^{-1}\ \mathrm{s},$$
$$[P] = 5.310 \times 10^{23}\ \mathrm{erg\ cm^{-3}},$$
$$[E] = 6.674 \times 10^{16}\ \mathrm{erg}, \quad [T] = 2.894 \times 10^9\ \mathrm{K}.$$

The region of solution of the problem or the computational region is in the shape of a spherical envelope with $r_\mathrm{min} \le r \le r_\mathrm{max}$, $r_\mathrm{min} = 5 \times 10^7$ cm, $r_\mathrm{max} = 1.000168 \times 10^9$ cm. The inner boundary at the radius $r = r_\mathrm{min}$ is assumed to be transparent, which is roughly achieved by setting the gradients of all physical quantities ($\mathbf{V}, \rho$, and e) equal to zero in the radial direction. At the radius $r = r_\mathrm{max}$, the boundary condition simulates a vacuum outside the computational region: (nearly zero) background values are assigned to the thermodynamic quantities (ρ, e, and P). The boundary conditions are sufficient for the difference scheme used, and their influence on the solution is assumed to be negligible.

In view of the equatorial symmetry along with the axial symmetry, it will suffice to find the solution only in one quadrant. Therefore, the angle θ for the computational region varies over the range 0 to $\pi/2$. At the boundary $\theta = \pi/2$, the velocity component V_θ is set equal to zero (and again the derivatives of all thermodynamic quantities become equal to zero). Thus, the choice of boundary conditions does not differ in any way from their choice in our previous papers (Imshennik *et al.* 2002, 2003).

DISCUSSION OF NUMERICAL RESULTS

In all probability, the following three calculations represent our main results most completely. Calculations [1] and [2] use the set of values from the second column of Table 1 as the initial state of the low-mass neutron star. Calculation [3] models an explosion with significantly overestimated energy release (the third column of Table 1). In all our calculations, we used the same computational mesh. The outer boundary of the computational region was located at the dimensionless radius $r_\mathrm{max} = 10.00168$, whose choice was discussed previously (Imshennik *et al.* 2003). There was arbitrariness in choosing the location of the inner computational boundary. The dimensionless radius in all our calculations was $r_\mathrm{min} = 0.5$, so the low-mass neutron star modeled in the form of a torus with a circular cross section (see above) was completely within the computational region. The spherical layer from r_min to $r^*_\mathrm{min} = 0.876$ was broken down into 40 equal zones in the radial direction. The computational mesh in the region from r^*_min to r_max was taken from our previous main calculation (Imshennik *et al.* 2003) (100 zones in the radial direction), which made it unnecessary to recalculate the spatial distribution of thermodynamic quantities in an equilibrium toroidal atmosphere for the new problem. The total number of zones in the direction in which the polar angle changed was 30 in all our calculations. A distinctive feature of calculation [2] is the replacement of an equilibrium toroidal atmosphere by an atmosphere with uniform density and temperature distributions with the integrated parameters of the matter (its total mass and internal energy) kept constant.

The numerical solution in all our calculations was performed up to a time of ~1.3 s, i.e., longer than the calculations by Aksenov *et al.* (1997) and Imshennik and Zabrodina (1999). Figure 1 presents the results of these calculations for a certain characteristic time, $t = 0.4$ s, the choice of which was justified by the convenience of comparing it with our previous calculations (to be more precise, the main results in

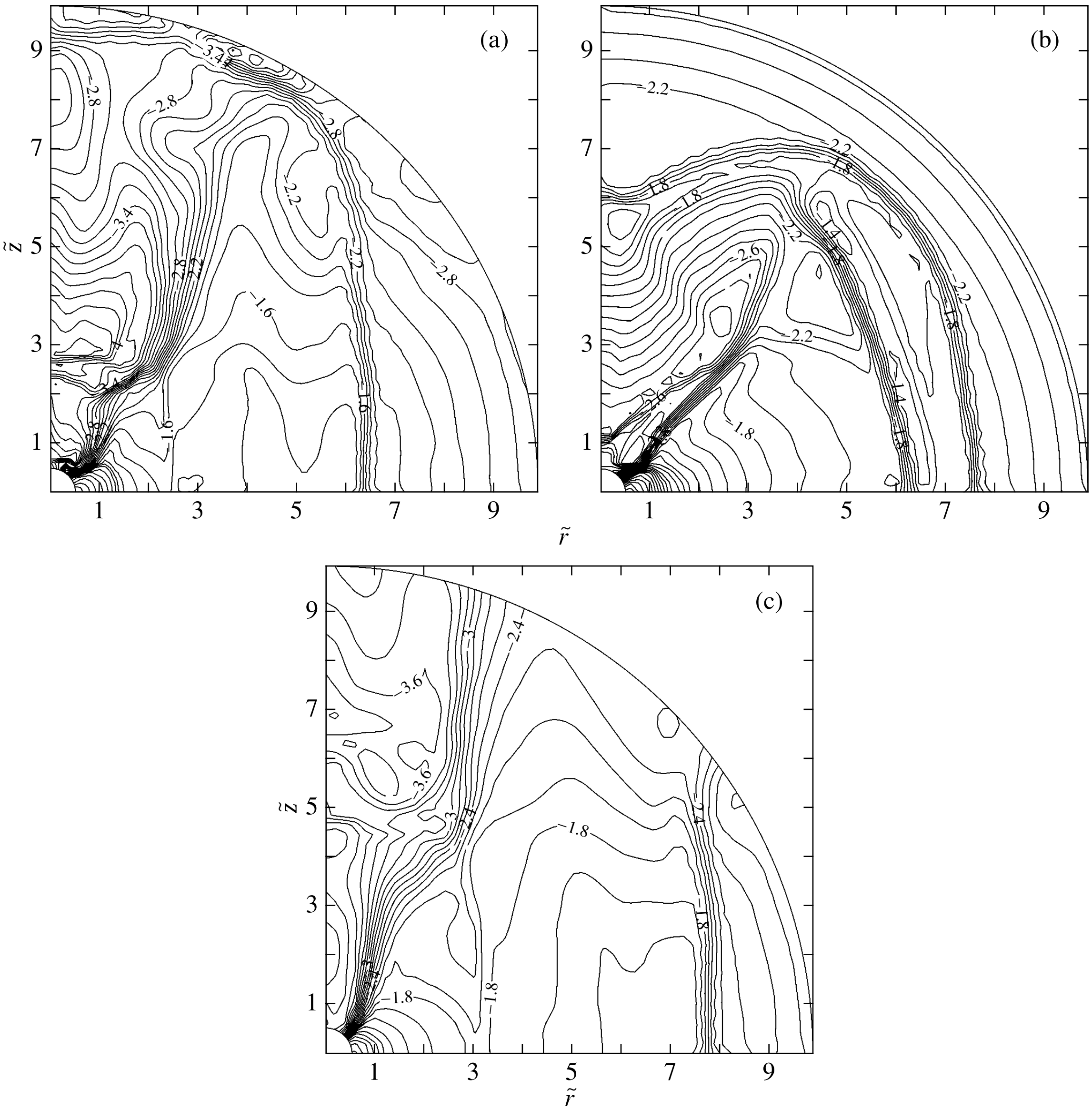

Fig. 1. Lines of constant logarithm of the density $\log \rho$ as a function of the cylindrical coordinates $\tilde{r}$ and $\tilde{z}$ for calculations [1] (a), [2] (b), and [3] (c) and for the time $t = 0.4$ s.

these papers are presented for a time of $t \approx 0.43$ s). Figures 1a–1c show the lines of constant logarithm of the dimensionless density for calculations [1–3], respectively. We see from these figures that the shape of the shock front generated by the explosion of a low-mass neutron star deviates from a sphere, particularly for calculations [1] and [3]. In contrast, this deviation is less pronounced for a homogeneous atmosphere (calculation [2]). For calculation [1], the velocities of the shock front characterized by a large velocity gradient in the equatorial plane and along the rotation axis differ by more than a factor of 1.5 and are equal to $\sim 1.2 \times 10^9$ and $\sim 2 \times 10^9$ cm s^{-1}, respectively. By the time under consideration, the leading part of the shock front (the upper part of Fig. 1a) reaches the outer spherical boundary of the computational region. In calculation [3], this part of the shock front is already outside the computational region by this time ($t = 0.4$ s). The current locations of the shock front on the equator at the time under consideration in calculations [2] and [3] almost coincide and correspond to a radius of $r_{\rm sw} \approx 7.8$, while in calculation [1], $r_{\rm sw} \approx 6.6$.

In the main calculation by Imshennik and Zabrodina (1999) (see Fig. 4 from their paper) with the corresponding initial internal energy $\varepsilon_0 = 0.675 \times 10^{51}$ erg (calculation II of Table 1 from their paper), the shock front reached a radius of $r_+ = z_{\rm max} \approx 12$ in the leading direction by this time, while the corresponding

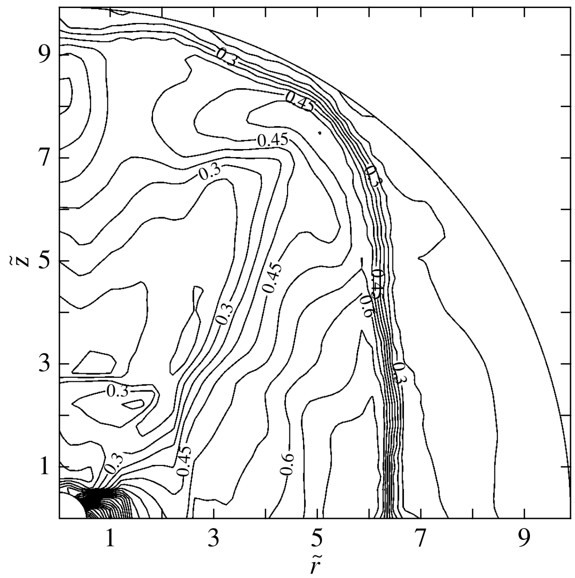

Fig. 2. Lines of constant temperature T as a function of the cylindrical coordinates $\tilde{r}$ and $\tilde{z}$ for calculation [1] and for the time $t = 0.4$ s.

radius in the trailing direction is $r_- = |z_{\min}| \approx 3.0$. Thus, the mean radius of the divergent and almost spherical shock front was $r_{\mathrm{sw}} = (r_- + r_+)/2 \approx 7.5$. In their main calculation, Aksenov *et al.* (1997) (see Fig. 8 from their paper) obtained a slightly larger value of $r_{\mathrm{sw}} \approx 8.2$, but their equation of state differed significantly from that used here and by Imshennik and Zabrodina (1999), although the final values of the energy release (0.9×10^{51} erg) in these calculations were approximately equal between themselves and to those in our calculations [1] and [2]. It seems natural that the radii from the previous papers being compared quantitatively matched most closely the radius in calculation [2] with a uniform density distribution, and not in calculation [1] with a nonuniform density distribution of the toroidal atmosphere. In the latter case, however, there is good agreement with the model of a weak explosion in the paper by Zabrodina and Imshennik (2000), where the lower initial internal energy (0.38×10^{51} erg) corresponded to the decrease in final energy release by exactly a factor of 2 ($\varepsilon_0 = 0.45 \times 10^{51}$ erg). Indeed, according to Fig. 2 from Zabrodina and Imshennik (2000), $r_+ \approx 12$, while $r_- \approx 2.2$ and, hence, $r_{\mathrm{sw}} \approx 7.1$.

In all three calculations, the shock front reaches the radius $r_{\max}$ in the equatorial plane approximately at the same time, ~0.6–0.7 s, with a small delay of 0.1 s for calculation [1]. In contrast to calculations [1] and [3], in which an extended region with almost constant density and temperature distributions is formed behind the shock front, a spherical layer of dense hot matter is formed in calculation [2]. Figure 2 shows the temperature distribution for calculation [1] at the time $t = 0.4$ s, which, as can be seen from the figure, resembles the density distribution, with the only difference that the lines of constant temperature behind the shock front are directed predominantly along the rotation axis (the temperature changes mainly in the equatorial direction), while the lines of constant density are more likely parallel to the equatorial plane.

Figure 3 shows the profiles of the logarithm of the density, temperature, and radial velocity for calculation [1] as a function of the cylindrical radius $\tilde{r}$ for $\theta = \pi/2$ (in the equatorial plane) at consecutive times from $t = 0$ to $t = 0.7$ s. At the initial time, the densities and temperatures are hind inside the circular torus (Figs. 3a and 3b). As we pointed out above, almost constant densities and temperatures are established behind the shock front at later times ($t > 0.4$ s), while at $t < 0.4$ s, the distributions exhibit minima that roughly correspond to the contact boundary between the matter of the toroidal atmosphere and the explosion products of the low-mass neutron star. In addition, we see from Fig. 3b that, starting from a time of $t \approx 0.1$ s, the temperature of the toroidal atmosphere does not exceed its critical value T_{cr}, which is determined by the well-known theoretical temperature minimum ($3-5 \times 10^9$ K) for the approximation of nuclear statistical equilibrium to be applicable. Imshennik and Zabrodina (1999) assumed T_{cr} to be 4.17×10^9 K. For convenience, we will use a close dimensionless value of $T_{\mathrm{cr}} = 1.5$. It also follows from the computed data on the chemical composition that all of the matter in the computational region almost completely recombines into iron ($X_{\mathrm{Fe}} \simeq 1$) by the time $t = 0.1$ s in all our calculations, including calculation [3] of a strong explosion. This once again confirms the previous conclusion that the effect of iron dissociation into free nucleons is negligible (see, e.g., Zabrodina and Imshennik 2000).

The velocity of the matter behind the shock front decreases to $\sim 9 \times 10^8$ cm s^{-1} by a time of $t \approx 0.3$ s and subsequently increases only slightly to 10^9 cm s^{-1} (see Fig. 3c). The velocity of the matter in calculation [3] behaves similarly, changing over a narrow range, $(1.3-1.5) \times 10^9$ cm s^{-1}. In contrast, its behavior in calculation [2] differs markedly: the velocity is high at the initial expansion phase, $\sim 1.8 \times 10^9$ cm s^{-1}, but subsequently, starting from a time of $t \approx 0.4$ s, it rapidly decreases by a factor of 2 to 10^9 cm s^{-1}. In all our calculations, a moderate rarefaction wave is formed in the region adjacent to the inner computational boundary. The maximum of the absolute velocity of the matter in the rarefaction wave is about 10^9 cm s^{-1} and lies well to the right from the radius $\tilde{r}_{\max}$ for the initial maximum of the atmospheric density.

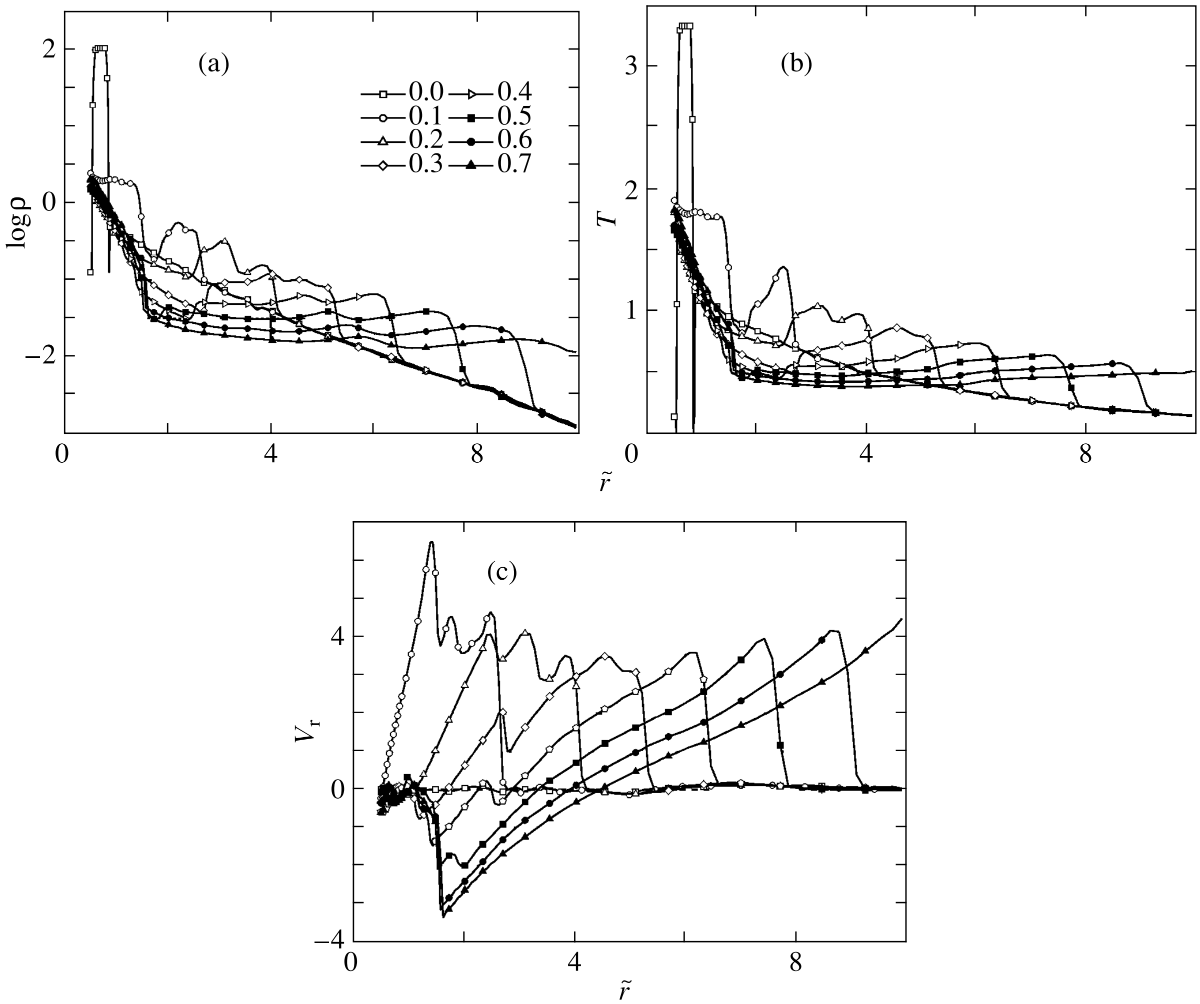

Fig. 3. Profiles of the logarithm of the density $\log\rho$ (a), temperature T (b), and radial velocity V_r (c) as a function of the cylindrical radius $\tilde{r}$ at $\theta = \pi/2$ for calculation [1] at sequential times from the beginning of our calculation $t = 0$ up to 0.7 s. The notation in panels (b) and (c) is the same as that in panel (a).

In Fig. 4, the integral of the total energy flux ($\varepsilon_{\rm tot}$) through the outer boundary of the computational region is plotted against time. We calculated $\varepsilon_{\rm tot}$ as the sum of the total internal and kinetic energies of the matter. The kinetic energy also includes the rotational kinetic energy; however, its contribution is negligible. As we see from Fig. 4, the curves reach constant values starting from a time of $t \simeq 1.0$ s. The asymptotic values of the total energy were found to be 2.3×10^{50}, 2.6×10^{50}, and 5.5×10^{50} erg for calculations [1–3], respectively. Thus, the total energy $\varepsilon_{\rm tot}$ for calculation [1], which is most justifiable in terms of the final energy release, is appreciably lower than the characteristic total energy of supernova explosions ($\sim 10^{51}$ erg). At the same time, in general, the problem of a deficit in total energy did not arise in the hydrodynamic calculations of an asymmetric explosion (Zabrodina and Imshennik 2000). In this paper, the initial kinetic energy of the low-mass neutron star ($E_{\rm k} \approx 3.5 \times 10^{50}$ erg) is entirely contained in the azimuthal velocity V_φ, which is specified in the initial data in such a way as to balance the exploding torus in the pulsar's gravitational field. In contrast, the orbital kinetic energy of the low-mass component of the binary in the hydrodynamic model of an asymmetric explosion (Aksenov *et al.* 1997; Imshennik and Zabrodina 1999) was essentially an appreciable contribution to the total energy release. In addition, the gravitational interaction with the pulsar, which hampered the development of an explosion to some (small) extent, was disregarded in the previous papers. It should therefore probably recognized that the explosion energy was overestimated, most likely only slightly, in that model. In contrast, the value obtained here, $\varepsilon_{\rm tot} = 2.3 \times 10^{50}$ erg, should be considered as a lower limit on the total energy of an asymmetric

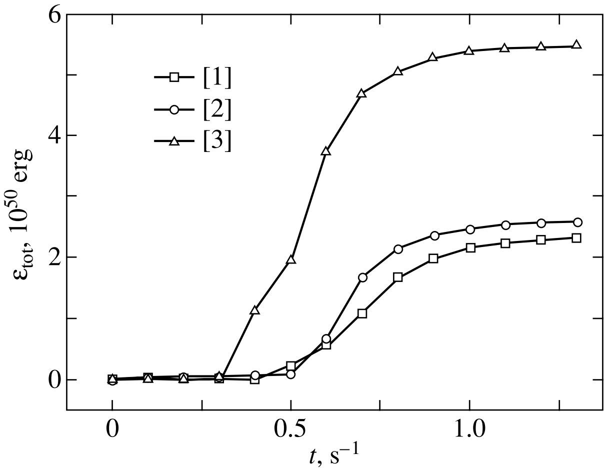

Fig. 4. Integral of the total energy flux ε_{tot} through the outer boundary of the computational region versus time t for calculations [1–3].

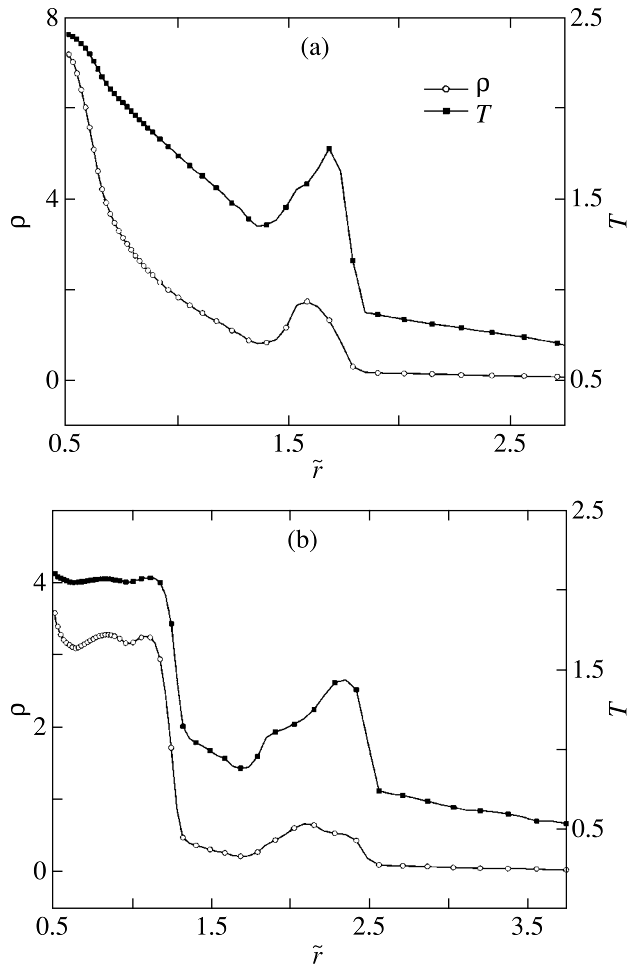

Fig. 5. Profiles of the density ρ and temperature T as a function of the cylindrical radius $\tilde{r}$ at $\theta = \pi/2$ for calculation [1] and for the times $t =$ (a) 0.05 and (b) 0.09 s.

supernova explosion for given initial energy release (within the framework of the rotational mechanism).

It may also be noted that an explosive synthesis of radioactive nickel $^{56}_{28}$Ni is possible behind the shock front. Using the simple reasoning behind explosive nucleosynthesis (Thielemann *et al.* 1990), we may assert that the $^{56}_{28}$Ni nuclide is predominantly produced among the iron-peak elements if the local temperature exceeds its critical value T_{cr}. In the presupernova shells composed of α-particle nuclei, radioactive nickel is synthesized outside the iron core (the shells of $^{28}_{14}$Si, $^{16}_{8}$O, $^{12}_{6}$C, etc.) in very short hydrodynamic times when the nuclear statistical equilibrium conditions are established. However, as was shown above, the post-shock temperature drops below its critical value by a time of $t \approx 0.1$ s. The radius of the shock front is $r_{sw} \approx 2.5$ (see above); i.e., it is smaller than the initial radius of the iron core $R_{Fe} = 4.38$. Nevertheless, we have reason to believe that the $^{56}_{28}$Ni nuclide is still synthesized.

Indeed, having studied the entropy distribution for a toroidal atmosphere (Imshennik *et al.* 2003), we showed that the atmosphere for a given rotation law is predominantly formed from the matter of the silicon presupernova shell rather than from the outer iron core. Thus, if the toroidal atmosphere is assumed to have a silicon composition, then we can obtain a threshold estimate for the synthesized nickel mass. Estimating this mass is complicated by the difficulty of accurately determining the location of the contact boundary between the explosive destruction products of the low-mass neutron star and the matter of the toroidal atmosphere when using the Eulerian difference scheme. The location of the contact boundary on the equator can be roughly determined from the local minimum in the density and temperature distributions. Figure 5 shows the profiles of these thermodynamic quantities at $\theta = \pi/2$ as a function of the cylindrical radius $\tilde{r}$ for two early times, $t = 0.05$ s and $t = 0.09$ s. The sought location of the contact boundary on the equator can be determined from them: $r_{cb}(0.05) \approx 1.35$ and $r_{cb}(0.09) \approx 1.70$. At the early times under consideration, the shock front is nearly spherical in shape. In addition, the toroidal atmosphere is located near the equatorial plane, i.e., at angles $\theta > \pi/4$, and, hence, the behavior of the contact boundary far from the equator affects only slightly the synthesized nickel mass being estimated. Therefore, it would be natural to assume that outside the equator, the section of the contact surface by the plane passing through the rotation axis is a circumference with the center at $\tilde{r}(t) = r_{min}$ and the radius $r(t) = r_{cb}(t) - r_{min}$. The synthesized nickel mass of interest is calculated in the region of space outside

Table 2. Masses of the atmospheric matter whose local temperature (behind the shock front) exceeds $T_{\rm cr}$ at various times

t, s	$M_{T>T_{\rm cr}}$, $M_\odot$
0.03	0.011
0.04	0.021
0.05	0.017
0.07	0.008
0.09	0.000

this toroidal volume. Table 2 gives the masses of the atmospheric matter whose local temperature (behind the shock front) exceeds $T_{\rm cr}$ for several early times. Clearly, the maximum mass in Table 2 is an upper limit on the synthesized $^{56}_{28}$Ni mass. This result is in satisfactory agreement with the estimates by Zabrodina and Imshennik (2000): $M_{\rm Ni} = 0.0185 M_\odot$ for the iron core radius $R_{\rm Fe} = 4.38$ and $M'_{\rm Ni} = 0.0277 M_\odot$ for $R_{\rm Fe} = 2.37$.

CONCLUSIONS

In the hydrodynamic theory of asymmetric supernova explosions, this work serves as a supplement that can be developed in terms of the rotational explosion scenario for collapsing supernovae (Aksenov *et al.* 1997; Imshennik and Zabrodina 1999; Zabrodina and Imshennik 2000). In this case, the important assumption of an axisymmetric explosion remains valid, because so far we have had to restrict our analysis to two-dimensional hydrodynamic models. The extreme complexity of the passage to three-dimensional models, which, of course, are the only ones that completely fit the rotational explosion scenario for collapsing supernovae, prompted us to investigate another hydrodynamic explosion model while remaining within the framework of the axisymmetric two-dimensional problem. In essence, this is because certain progress in describing the structure of the distribution of matter around a collapsed iron core had been made previously (Imshennik and Manukovskii 2000; in particular, Imshennik *et al.* 2003). The presence of stationary toroidal iron atmospheres instead of the rough assumption made in previous papers about a uniform iron gas distribution, which is essentially nonstationary on the long evolution time scales of neutron-star binaries considered in the above scenario, made this additional series of hydrodynamic calculations appropriate.

At the same time, much in the formulation of the problem remains unchanged. First, the unique choice of initial parameters of the circular orbit for an exploding low-mass neutron star with a critical mass is preserved thanks to the assumption that the kick velocity of the high-mass component in the binary (a pulsar) is 1000 km s^{-1}, in agreement with the observed high velocities of young pulsars. Second, the same equation of state in the approximation of nuclear statistical equilibrium is used for the explosion products of the neutron star and the surrounding gas of the toroidal atmosphere; i.e., in particular, the possible large expenditure of energy on the dissociation of iron nuclei into free nucleons is taken into account under the justified conservation condition for the neutron-to-proton number ratio, 30/26, typical of ^{56}Fe nuclides (Imshennik and Zabrodina 1999). Nevertheless, the two-dimensional peculiarities of the axisymmetric model under consideration make it necessary to change the direction of the z coordinate axis to a perpendicular direction that coincides with the rotation axis of the toroidal atmosphere obtained; in turn, the latter is clearly the given rotation axis of the entire star before its collapse. Instead of describing an exploding neutron star in the shape of a sphere, we had to specify it in the shape of a torus in this case. It is qualitatively clear that this change in initial conditions excluded the possibility of the development of a directed asymmetry with the leading direction of the velocity vector of the exploded neutron star in the problem. In this model, the explosion is attributable only to energy release as the low-mass neutron star is destroyed. In this case, there is absolutely no contribution from the kinetic energy of the translational motion of the exploding star, because the orbital velocity becomes the rotational velocity of the torus introduced in the initial conditions for which the corresponding centrifugal force is exactly balanced by the attractive force of the pulsar placed at the coordinate origin. In this formulation of the problem, we rigorously took into account the gravitational interaction that was not included in previous papers on the hydrodynamic theory of asymmetric explosions at all. Thus, it is quite clear that the final explosion energy as the total energy that passed through the outer boundary of the computational region of the divergent shock wave will be appreciably lower than the energy obtained previously by Aksenov *et al.* (1997) and Imshennik and Zabrodina (1999), which is approximately equal to a characteristic value of 10^{51} erg. The main calculation of this paper, which is close in its final energy release to 10^{51} erg (the second column of Table 1), should be used for comparison. Indeed, the final energy is $\sim 0.2 \times 10^{51}$ erg (see Fig. 4). The leading sector of the shock wave in this calculation is located in the axial direction, which is attributable to a decrease in the matter density there rather than to the directed motion of the exploded neutron star, as was the case in previous models. Nevertheless, the numerical solution of this problem undoubtedly yielded a considerable lower limit for the final explosion energy. This is of great importance, because, first, it is still far from the characteristic supernova explosion energy ($\sim 10^{51}$ erg) obtained rigorously using the hydrodynamic theory for SN 1987A (Blinnikov 1999; Utrobin 2004) and, second, it is much higher than its value in the one-dimensional spherically symmetric hydrodynamic models of collapsing supernovae. For example, in the model by Imshennik and Nadezhin (1977), this energy was found to be only 3×10^{46} erg due to the rotation effect that was taken into account in the form of a centrifugal force averaged over the polar angle.

In discussing our results, we repeatedly touched on the closeness of the physical parameters obtained here to the parameters of the so-called model of a weak explosion (with half the initial internal energy) from Zabrodina and Imshennik (2000). The final explosion energy in the cited paper is even slightly larger than 10^{51} erg (see Fig. 6 from this paper). However, the following critical remark regarding this parameter can be made. The initial energy of the electron component of the degenerate iron gas, $\sim 0.4 \times 10^{51}$ erg, contributes significantly to it. This value just corresponds to a large mass of this gas, $\sim M_\odot$ (with the density $\rho = 5.66 \times 10^5$ g cm^{-3} and the mean shock front radius $R_{\rm sw} \simeq 10^9$ cm), while this mass is an order of magnitude lower, $\sim (0.1{-}0.2) M_\odot$, under the formation conditions of a toroidal atmosphere. Accordingly, the energy contribution from this effect should be disregarded, so a value of $\sim 0.5 \times 10^{51}$ erg was actually obtained in the model of a weak explosion. The results under discussion must be compared with it; otherwise, they indeed differ little.

Our comparison suggests that the hydrodynamic model under consideration demonstrates an appreciable attenuation of the divergent shock wave, although, strictly speaking, the direct (see above) comparison of our results in the equatorial plane with those of the previous hydrodynamic model in the axial direction is conditional. Only a three-dimensional model will probably allow us to establish which of the two-dimensional hydrodynamic models being compared is suitable. Of course, in such a three-dimensional model, it will be unnecessary to "spread" the exploding neutron star into a torus, because the natural spherical shape adopted by Aksenov *et al.* (1997) and Imshennik and Zabrodina (1999) may be preserved in this case.

ACKNOWLEDGMENTS

We thank M.S. Popov for his assistance in tabulating the equation of state and for a helpful discussion of our results. This work was supported in part by the Russian Foundation for Basic Research (project no. 00-15-96572) and the Federal program Research and Development on Priority Fields of Science and Technology (contract no. 40.022.1.1.1103) and an additional agreement from January 31, 2003.

REFERENCES

1. A. G. Aksenov, Pis'ma Astron. Zh. **25**, 226 (1999) [Astron. Lett. **25**, 185 (1999)].
2. A. G. Aksenov, S. I. Blinnikov, and V. S. Imshennik, Astron. Zh. **72**, 717 (1995) [Astron. Rep. **39**, 638 (1995)].
3. A. G. Aksenov, E. A. Zabrodina, V. S. Imshennik, and D. K. Nadezhin, Pis'ma Astron. Zh. **23**, 779 (1997) [Astron. Lett. **23**, 677 (1997)].
4. G. Baym, C. Petchick, and P. Sutherland, Astrophys. J. **170**, 299 (1971).
5. L. Bildsten and C. Cutler, Astrophys. J. **400**, 175 (1992).
6. S. I. Blinnikov, Pis'ma Astron. Zh. **25**, 424 (1999) [Astron. Lett. **25**, 359 (1999)].
7. S. I. Blinnikov, V. S. Imshennik, D. K. Nadezhin, *et al.*, Astron. Zh. **67**, 1181 (1990) [Sov. Astron. **34**, 595 (1990)].
8. S. I. Blinnikov, I. D. Novikov, T. V. Perevodchikova, and A. G. Polnarev, Pis'ma Astron. Zh. **10**, 422 (1984) [Sov. Astron. Lett. **10**, 177 (1984)].
9. P. Colella and P. R. Woodward, J. Comput. Phys. **54**, 174 (1984).
10. M. Colpi, S. L. Shapiro, and S. A. Teukolsky, Astrophys. J. **339**, 318 (1989).
11. M. Colpi, S. L. Shapiro, and S. A. Teukolsky, Astrophys. J. **369**, 422 (1991).
12. M. Colpi, S. L. Shapiro, and S. A. Teukolsky, Astrophys. J. **414**, 717 (1993).
13. M. Colpi and I. Wasserman, Astrophys. J. **581**, 1271 (2002).
14. S. K. Godunov, A. V. Zabrodin, M. Ya. Ivanov, *et al., Numerical Solvation of Multidimensional Gas-Dynamic Problems* (Nauka, Moscow, 1976) [in Russian].
15. V. S. Imshennik, Pis'ma Astron. Zh. **18**, 489 (1992) [Sov. Astron. Lett. **18**, 194 (1992)].
16. V. S. Imshennik and K. V. Manukovskiĭ, Pis'ma Astron. Zh. **26**, 917 (2000) [Astron. Lett. **26**, 788 (2000)].
17. V. S. Imshennik, K. V. Manukovskiĭ, D. K. Nadezhin, and M. S. Popov, Pis'ma Astron. Zh. **28**, 913 (2002) [Astron. Lett. **28**, 821 (2002)].
18. V. S. Imshennik, K. V. Manukovskiĭ, and M. S. Popov, Pis'ma Astron. Zh. **29**, 934 (2003) [Astron. Lett. **29**, 831 (2003)].
19. V. S. Imshennik and D. K. Nadezhin, Pis'ma Astron. Zh. **3**, 353 (1977) [Sov. Astron. Lett. **3**, 188 (1977)].
20. V. S. Imshennik and M. S. Popov, Pis'ma Astron. Zh. **20**, 620 (1994) [Astron. Lett. **20**, 529 (1994)].
21. V. S. Imshennik and M. S. Popov, Pis'ma Astron. Zh. **24**, 252 (1998) [Astron. Lett. **24**, 206 (1998)].

22. V. S. Imshennik and M. S. Popov, Pis'ma Astron. Zh. **27**, 101 (2001) [Astron. Lett. **27**, 81 (2001)].
23. V. S. Imshennik and M. S. Popov, Pis'ma Astron. Zh. **28**, 529 (2002) [Astron. Lett. **28**, 465 (2002)].
24. V. S. Imshennik and O. G. Ryazhskaya, Pis'ma Astron. Zh. **30**, 17 (2004) [Astron. Lett. **30**, 14 (2004)].
25. V. S. Imshennik and E. A. Zabrodina, Pis'ma Astron. Zh. **25**, 123 (1999) [Astron. Lett. **25**, 93 (1999)].
26. J. M. Lattimer and F. D. Swesty, Bull. Am. Astron. Soc. **21**, 1078 (1989).
27. S. H. Lubow and F. H. Shu, Astrophys. J. **198**, 383 (1975).
28. A. Lyne and D. R. Lorimer, Nature **369**, 127 (1994).
29. B. Paczynski, Annu. Rev. Astron. Astrophys. **9**, 183 (1971).
30. J.-L. Tassoul, *Theory of Rotating Stars* (Princeton Univ. Press, Princeton, 1978; Mir, Moscow, 1982).
31. F.-K. Thielemann, M. Hashimoto, and K. Nomoto, Astrophys. J. **349**, 222 (1990).
32. V. P. Utrobin, Pis'ma Astron. Zh. **30**, 334 (2004) [Astron. Lett. **30**, 293 (2004)].
33. E. A. Zabrodina and V. S. Imshennik, Pis'ma Astron. Zh. **26**, 665 (2000) [Astron. Lett. **26**, 572 (2000)].

Translated by V. Astakhov

Astronomy Letters, Vol. 30, No. 12, 2004, pp. 816–823. Translated from Pis'ma v Astronomicheskiĭ Zhurnal, Vol. 30, No. 12, 2004, pp. 897–904.

The Maximum Energy and Spectra of Cosmic Rays Accelerated in Active Galactic Nuclei

A. V. Uryson*

Lebedev Physical Institute, Russian Academy of Sciences, Leninskii pr. 53, Moscow, 117924 Russia
Received March 16, 2004

Abstract—We computed the energy spectra of the incident (on an air shower array) ultrahigh-energy ($E > 4 \times 10^{19}$ eV) cosmic rays (CRs) that were accelerated in nearby Seyfert nuclei at redshifts $z \leq 0.0092$ and in BL Lac objects. These were identified as possible CR sources in our previous works. For our calculations, we took the distribution of these sources over the sky from catalogs of active galactic nuclei. In accordance with the possible particle acceleration mechanisms, the initial CR spectrum was assumed to be monoenergetic for BL Lac objects and a power law for Seyfert nuclei. The CR energy losses in intergalactic space were computed by the Monte Carlo method. We considered the losses through photopion reactions with background radiation and the adiabatic losses. The artificial proton statistic was 10^5 for each case considered. The maximum energy of the CRs incident on an air shower array was found to be 10^{21} eV, irrespective of where they were accelerated. The computed spectra of the particles incident on an air shower array agree with the measurements, which indirectly confirms the adopted acceleration models. At energies $E \geq 5 \times 10^{19}$ eV, the spectrum of the protons from nearby Seyfert nuclei that reached an air shower array closely matches the spectrum of the particles from BL Lac objects. BL Lac objects are, on average, several hundred Mpc away. Therefore, it is hard to tell whether a blackbody cutoff exists by analyzing the shape of the measured spectrum at $E \geq 5 \times 10^{19}$ eV. *© 2004 MAIK "Nauka/Interperiodica".*

Key words: *cosmic rays, ultrahigh-energy cosmic rays, active galactic nuclei.*

INTRODUCTION

At present, cosmic rays (CRs) with energies $E > 4 \times 10^{19}$ eV are generally believed to be extragalactic in origin, but their sources have not been firmly established. Various astrophysical objects, cosmological defects, decaying superheavy primordial particles of cold dark matter, and gamma-ray bursts are considered in the literature as their possible sources (see the review by Nagano and Watson (2000) and references therein). In the first case, the CR sources can be identified if the CR arrival directions are known and if the particles are assumed to propagate in the intergalactic magnetic fields almost rectilinearly. We directly identified the possible sources of ultrahigh-energy CRs previously (Uryson 1996, 2001a, 2004a) and found them to be Seyfert nuclei at redshifts $z \leq 0.0092$ and BL Lac objects. BL Lac objects were also identified with possible CR sources by Gorbunov *et al.* (2002). Kardashev (1995) and Uryson (2001b, 2004b) suggested a particle acceleration mechanism in BL Lac objects and moderately active galactic nuclei, respectively. According to these authors, CRs can be accelerated in BL Lac objects up to $10^{27} Z$ eV, where Z is the particle charge, and, if there are energy losses in the sources, up to $10^{21} Z$ eV. In Seyfert nuclei, particles can be accelerated up to an energy of 8×10^{20} eV. In intergalactic space, particles interact with background radiation; as a result, they inevitably lose their energy (Greisen 1966; Zatsepin and Kuzmin 1966). Particles of different energies traverse different distances without significant energy losses. These distances for ultrahigh-energy CRs were estimated by Stecker (1968, 1998). The redshifts $z \leq 0.0092$ of Seyfert nuclei correspond to distances up to 40 Mpc (for the Hubble constant $H = 75$ km s^{-1} Mpc^{-1}), in agreement with the results of Stecker (1968, 1998). The BL Lac objects identified as possible CR sources are far (up ~1000 Mpc (Veron-Cetty and Veron 2001)) away. Therefore, the question arises as to whether the particles with an energy of 3×10^{20} eV (the maximum recorded CR energy (Bird *et al.* 1995)) accelerated in BL Lac objects can reach an air shower array. In this paper, we computed the energies of the particles from BL Lac objects that reached an air shower array and the energy spectra of the incident (on an air shower array) CRs that escaped from active galactic nuclei (AGNs) with power-law and

*E-mail: uryson@sci.lebedev.ru

monoenergetic spectra. We compared the computed and measured spectra. For our calculations, we took the distribution of AGNs from the catalog by Veron-Cetty and Veron (2001).

DESCRIPTION OF THE MODEL

According to the model by Kardashev (1995), particles in BL Lac objects are accelerated in the electric field induced near a supermassive black hole with a mass of $\sim 10^9 M_\odot$. Particles are accelerated in this field up to an energy of $10^{27} Z$ eV; the particle energy can decrease through curvature radiation to $10^{21} Z$ eV. Based on this acceleration mechanism, we assume in our calculations that the initial spectrum of the protons accelerated in BL Lac objects is monoenergetic with an initial energy of 10^{27} and 10^{21} eV. Since particles in Seyfert nuclei may be accelerated at shock fronts (Uryson 2001b), we assume that the initial spectrum of the particles from them is a power law ($\sim E^{-\chi}$) with a spectral index of $\chi = 2.6$ and 3.0. Particles in Seyfert nuclei can be accelerated up to an energy of 8×10^{20} eV.

The composition of CRs with energies $E \approx 4 \times 10^{19}$–$3 \times 10^{20}$ eV is not yet completely known. In accordance with the data of Shinozaki *et al.* (2003), we assume that CRs with energies as high as 10^{21} eV are particles rather than gamma-ray photons.

The propagation of CRs in intergalactic space was considered under the following assumptions. The nuclei disintegrate into nucleons through their interactions with background radiation, traveling no more than 100 Mpc from their source (Puget *et al.* 1976; Stecker 1998). Therefore, if the CR sources are much farther than 100 Mpc, then, for simplicity, we may assume that the nuclei completely fragment near the source and consider only the propagation of protons in intergalactic space. Since the overwhelming majority of BL Lac objects are $R > 400$ Mpc away (Veron-Cetty and Veron 2001), this assumption is justified for the CRs emitted by BL Lac objects. For simplicity, we assume that only protons propagate from Seyfert nuclei as well.

We computed the CR energy losses in intergalactic space under the following assumptions. Protons interact with primordial and infrared photons. Protons with energies $E > 4 \times 10^{19}$ eV lose their energy mainly through the photopion reactions $\mathrm{p} + \gamma \to \mathrm{N} + \pi$; the losses through the electron–positron pair production are negligible (Blumenthal 1970; Berezinsky *et al.* 1990). The density spectrum for primordial photons with energy ε is described by the Planckian distribution

$$n(\varepsilon)d\varepsilon = \varepsilon^2 d\varepsilon / [\pi^2 \square^3 c^3 (\exp(\varepsilon/kT) - 1)] \qquad (1)$$

with the temperature $T = 2.7$ K, the mean photon energy is $\langle\varepsilon\rangle \approx 6 \times 10^{-4}$ eV, and their mean density is $\langle n_\mathrm{o}\rangle \approx 400$ cm^{-3}. For the photons of the high-energy tail in the Planckian distribution, the mean energy is $\langle\varepsilon_\mathrm{t}\rangle \approx 1 \times 10^{-3}$ eV and the mean density is $\langle n_\mathrm{t}\rangle \approx 42$ cm^{-3}.

The energy range of the infrared radiation is 2×10^{-3}–0.8 eV; at present, there are no detailed spectral measurements. We assumed that the infrared radiation spectrum is described by the numerical expression (Puget *et al.* 1976; Stecker 1998)

$$n(\varepsilon) = 7 \times 10^{-5} \varepsilon^{-2.5}\ \mathrm{cm}^{-3}\ \mathrm{eV}^{-1}, \qquad (2)$$

the mean energy of the infrared photons is $\langle\varepsilon_\mathrm{IR}\rangle \approx 5.4 \times 10^{-3}$ eV, and their mean density is $\langle n_\mathrm{IR}\rangle \approx 2.28$ cm^{-3}.

The photopion reactions are threshold ones. The threshold energy of the photon in the proton frame of reference is $\varepsilon^*_\mathrm{th} \approx 145$ MeV; the threshold inelasticity coefficient is $K_\mathrm{th} \approx 0.126$ (Stecker 1968). The cross section σ and the inelasticity coefficient K of the photoprocesses depend on the energy of the photon in the proton frame of reference ε^*. The dependences $\sigma(\varepsilon^*)$ and $K(\varepsilon^*)$ were taken from Particle Data Group (2002) and Stecker (1968). The values of σ and K used in our calculations are given in the table.

In addition to the photopion reactions, protons lose their energy through the expansion of the Universe. The adiabatic losses of a proton that propagates with an initial energy E from a point with a redshift z to a point with $z = 0$ are

$$-dE/dt = H(1+z)^{3/2}E. \qquad (3)$$

The cosmological evolution of the Universe was taken into account in the CR propagation. We used the Einstein–de Sitter model with $\Omega = 1$, in which the time and the redshift are related by

$$t = 2/3H^{-1}(1+z)^{-3/2}; \qquad (4)$$

the distance to an object at redshift z is

$$r = 2/3cH^{-1}[1 - (1+z)^{-3/2}]\ \mathrm{Mpc}. \qquad (5)$$

At the epoch with a redshift z, the primordial photon density and energy were, respectively, a factor of $(1+z)^3$ and $(1+z)$ higher than those at $z = 0$ (Berezinsky *et al.* 1990).

We assumed that the particles propagate in the intergalactic magnetic fields almost rectilinearly.

The sources of ultrahigh-energy CRs, BL Lac objects and Seyfert nuclei at $z \leq 0.0092$, were assumed to be distributed in redshift in accordance with the catalog by Veron-Cetty and Veron (2001). The z distributions of these objects at declinations $\delta \geq -15°$ are shown in Figs. 1 and 2.

Cross sections σ and inelasticity coefficients K from Particle Data Group (2002) and Stecker (1998) used in our calculations

ε^*, GeV	0.145	0.2	0.3	0.33	0.4	0.5	0.6	0.7	0.8	0.9	1.0	1.4	2.0	3.0	4.0	5.0
K	0.13	0.145	0.2	0.215	0.23	0.25	0.3	0.33	0.35	0.38	0.4	0.46	0.5	0.5	0.5	0.5
σ, mbarn	0.05	0.08	0.4	0.43	0.35	0.23	0.22	0.215	0.2	0.19	0.17	0.125	0.14	0.095	0.073	0.07

CALCULATIONS

The calculations were performed as follows. First, we generated the redshift z_0 of a source by the Monte Carlo method in accordance with the distributions shown in Figs. 1 and 2. Subsequently, we calculated the distance to the source. Since the energy losses of the CRs depend on the distances that they traverse in intergalactic space, we determined them by two methods to reach reliable conclusions. The first method uses formula (5). The second method assumes that $r = czH^{-1}$ (Mpc) for $z < 0.4$ (Pskovskii 1990) and uses formula (5) for higher z. The calculations were performed with $H = 75$ and 100 km s^{-1} Mpc^{-1}. Next, we randomly generated the proton energy E and the angle θ in the laboratory frame and determined the photon energy in the proton frame

$$\varepsilon^* = \gamma\varepsilon(1 - \beta\cos\theta), \qquad (6)$$

where γ is the Lorentz factor of the proton, and $\beta = (1 - 1/\gamma^2)^{1/2}$. If $\varepsilon^* < \varepsilon^*_{\rm th}$, then the proton interacted with photons of the high-energy tail in the Planckian distribution. If, alternatively, the photon energy ε^* was also below its threshold value in this case, then the proton interacted with infrared photons. The cross section σ and the inelasticity coefficient K for this interaction were determined from the value of ε^*. Subsequently, we calculated the proton mean free path $\langle\lambda\rangle = (\langle n\rangle\sigma)^{-1}$, where $\langle n\rangle = \langle n_{\rm o}\rangle$, $\langle n_{\rm t}\rangle$, or $\langle n_{\rm IR}\rangle$, depending on which photon the proton interacted with. Next, we generated the proton mean free path L by the Monte Carlo method and calculated the redshift z_1 of the proton after it traversed the distance L. At the point with z_1, the proton energy decreased due to its interaction with the photon by $(\Delta E)_{\rm ph} = EK$. The decrease in energy due to the adiabatic losses is

$$(\Delta E)_{\rm ad} = E(z_0 - z_1)/(1 + z_0). \qquad (7)$$

This procedure was then repeated. In our calculations of the adiabatic losses at the point with redshift z_2, the point of the preceding interaction with redshift z_1 in formula (7) was taken in place of the point with z_0, the point with z_2 was taken in place of the point with z_1, an so on. The procedure ended if the proton reached the Earth (the point with $z_i = 0$) or if its energy decreased to $E < 4 \times 10^{19}$ eV.

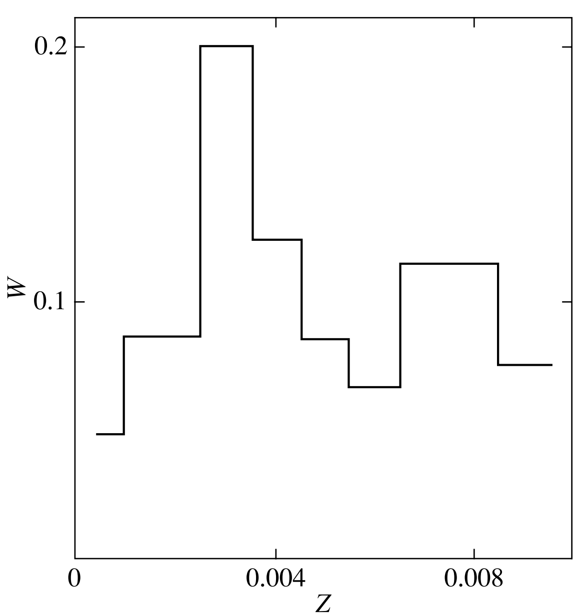

Fig. 1. Redshift distribution of nearby ($z \leq 0.0092$) Seyfert nuclei normalized to the total number of objects.

RESULTS

The Maximum Particle Energy in a Source

Aharonian *et al.* (2002) and Medvedev (2003) theoretically estimated the maximum CR energy in

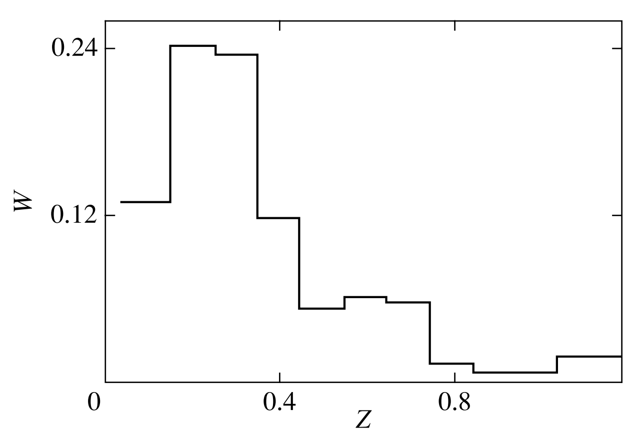

Fig. 2. Redshift distribution of BL Lac objects normalized to the total number of objects.

sources to be $\sim 10^{21}$ eV. The initial proton energy in BL Lac objects without and with the inclusion of curvature losses in the source is, respectively, 10^{27} and 10^{21} eV (Kardashev 1995). These estimates can be easily compared with the CR data by calculating the mean energies of the protons with initial energies of 10^{27} and 10^{21} eV incident on an air shower array. We computed the energies of the incident (on an air shower array) protons from BL Lac objects that were distributed as in Fig. 2, and that had the above initial energies, using the Monte Carlo method. In each case, the artificial proton statistic was 10^4. The mean proton energies on Earth were found to be 10^{24} and 6×10^{19} eV, respectively. The first value is in conflict with the experimental data (recall that, based on the possible CR acceleration mechanism (Kardashev 1995), we assumed the initial spectrum in BL Lac objects to be monoenergetic), the calculation with an initial energy of 10^{21} eV is consistent with the measurements, in agreement with its theoretical estimate (Aharonian *et al.* 2002; Medvedev 2003). This value is close to the maximum energy, 8×10^{20} eV, of the particles emitted by Seyfert nuclei (Uryson 2001b, 2004b). For the subsequent analysis, let us consider the proton spectra on Earth.

The Spectra of the Protons Incident on an Air Shower Array

The measured CR spectrum at $E > 4 \times 10^{19}$ eV exhibits a flat component and a bump that are probably attributable to the CR energy losses in intergalactic space: these losses lead to the "transfer" of particles to the range of lower energies provided that the energy losses decrease with decreasing energy (Hillas 1968; Hill and Shramm 1985). Berezinsky and Grigor'eva (1988), Berezinsky *et al.* (1989), and Yoshida and Teshima (1992) computed the CR spectrum and analyzed its shape. The closer the source, the higher the energy at which a bump appears in the spectrum. We analyzed the shape of the measured spectrum in the energy range 10^{18}–10^{20} eV previously (Uryson 1997).

Since the energies of the particles that trigger air showers are measured by different methods, the CR spectra measured on different air shower arrays differ in intensity. The combined spectra normalized using measurements on a particular air shower array are given in the literature. Here, we compare the computed spectra with published measurements.

The differential ultrahigh-energy CR spectra measured on different air shower arrays and normalized in different ways are shown in Fig. 3: the spectra from Nagano and Watson (2000) normalized using AGASA data are shown in Figs. 3a and 3c; the spectra obtained on the same air shower arrays and on the HiRes array and normalized using the Fly's Eye array are shown in Fig. 3b (Bahcall and Waxman 2003). The computed spectra normalized using measurements are shown in the same figures. The artificial proton statistic is 10^5 for each curve. Let us first consider the spectra in Fig. 3a. The large measurement errors make it difficult to compare the computed curves with the experimental data. However, two models are clearly inconsistent with the measurements: those with a monoenergetic initial spectrum in Seyfert nuclei and with a power-law initial spectrum in BL Lac objects. The models with a monoenergetic initial spectrum in BL Lac objects and with a power-law initial spectrum in Seyfert nuclei are suitable for describing the data, but the initial spectral index, 3.0 or 2.6, is difficult to determine due to the large errors. This is consistent with the possible particle acceleration conditions in these sources.

The measured spectrum in Fig. 3b agrees with these curves, except for the HiRes data points at $E < 10^{20}$ eV. The HiRes data are best described by the model with a power-law spectrum in BL Lac objects at $\chi = 2.0$ and by the model with a power-law spectrum in Seyfert nuclei at $\chi = 3$.

Figure 3c shows the same data as in Fig. 3a, but the curves were computed for $H = 100$ km s^{-1} Mpc^{-1} where the distances were determined by the second method (see the section "Calculations"). In this case, the measurements are also described by the models with a monoenergetic initial spectrum in BL Lac objects and with a power-law initial spectrum in Seyfert nuclei.

Thus, the data from different air shower arrays are described by the model in which the CR sources are nearby Seyfert nuclei with a power-law initial spectrum. The model in which the CR sources are BL Lac objects with a monoenergetic initial spectrum is also suitable for describing the data, except for the HiRes data.

At $E > 10^{20}$ eV, the spectra computed in the models with a monoenergetic spectrum in BL Lac objects and with a power-law spectrum in nearby Seyfert nuclei satisfactorily describe the measurements and are very similar. The computed CR spectra in these models will differ greatly if 2% of the BL Lac objects at redshifts $z < 0.1$ are assumed to be at the distance with $z = 0.01$ (according to the catalog by Veron-Cetty and Veron (2001), the minimum redshift for BL Lac objects is $z = 0.02$). The spectra computed under this assumption are shown in Fig. 3c.

It follows from the above analysis that the models for both far and nearby sources account for the measured CR spectrum at energies $E > 4 \times 10^{19}$ eV.

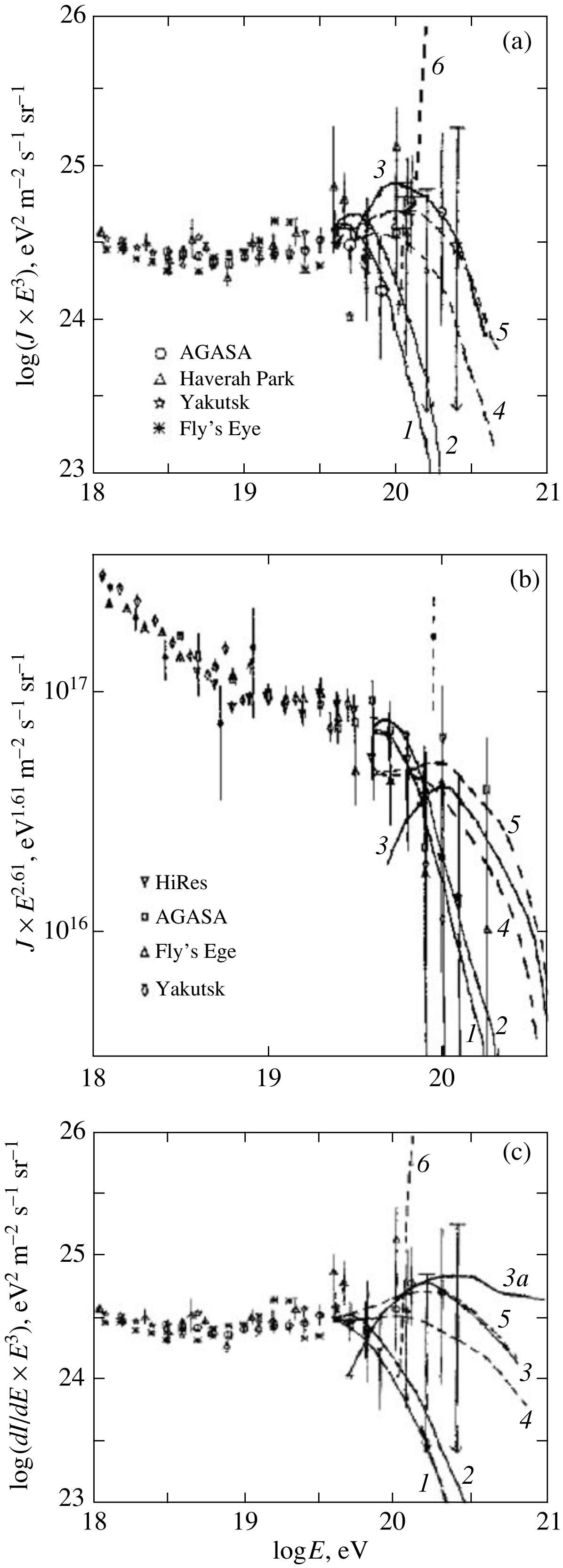
(a)
$\log(J \times E^3)$, eV^2 m^{-2} s^{-1} sr^{-1}
AGASA
Haverah Park
Yakutsk
Fly's Eye
(b)
$J \times E^{2.61}$, eV$^{1.61}$ m^{-2} s^{-1} sr^{-1}
HiRes
AGASA
Fly's Ege
Yakutsk
(c)
$\log(dI/dE \times E^3)$, eV^2 m^{-2} s^{-1} sr^{-1}
$\log E$, eV

Fig. 3. (a) Differential CR energy spectra as measured on different air shower arrays (Haverah Park, Fly's Eye, AGASA, and Yakutsk) from Nagano and Watson (2000). The curves represent the spectra computed for $H = 75$ km s^{-1} Mpc^{-1} where the distances were determined by the first method; the solid lines indicate the spectra of the CRs arrived from BL Lac objects: a power-law initial spectrum in the sources with $\chi = 3.0$ (*1*), a power-law initial spectrum with $\chi = 2.6$ (*2*), and a monoenergetic initial spectrum (*3*); the dashed lines indicate the spectra of the CRs arrived from Seyfert nuclei: a power-law initial spectrum with $\chi = 3.0$ (*4*), a power-law initial spectrum with $\chi = 2.6$ (*5*), and a monoenergetic initial spectrum (*6*). (b) The differential CR energy spectra as measured on different air shower arrays (Haverah Park, Fly's Eye, HiRes, AGASA, and Yakutsk) from Bahcall and Waxman (2003). The spectra were computed in the same way as those in Fig. 3a. The solid lines indicate the spectra of the CRs arrived from BL Lac objects: a power-law initial spectrum in the source with $\chi = 2.6$ (*1*), a power-law initial spectrum with $\chi = 2.0$ (*2*), and a monoenergetic initial spectrum (*3*); the dashed lines indicate the spectra of the CRs arrived from Seyfert nuclei: a power-law initial spectrum with $\chi = 3.0$ (*4*) and a power-law initial spectrum with $\chi = 2.6$ (*5*). (c) The same as Fig. 3a, but the spectra were computed for $H = 100$ km s^{-1} Mpc^{-1} where the distances were determined by the second method. The letter a mark the spectra of the CRs arrived from BL Lac objects for $z_{\min} = 0.01$; in the remaining cases, the spectra from BL Lac objects were computed for $z_{\min} = 0.02$.

Therefore, analyzing the spectrum in this energy range, we currently cannot determine whether it has a blackbody cutoff. In addition, AGASA, HiRes, Fly's Eye, Haverah Park, and Yakutsk data indirectly confirm our model of particle acceleration in nearby sources. Data from the air shower arrays, except for HiRes, also confirm the model of particle acceleration in BL Lac objects.

At energies below 10^{19} eV, the spectrum may be shaped by particles from distant sources (Berezinsky *et al.* 1990; Yoshida and Teshima 1992). According to the currently available data (Veron-Cetty and Veron 2001), the total number of Seyfert nuclei and BL Lac objects is several thousand and several hundred, respectively.

Estimates of the CR Luminosity for Sources

We estimated the CR luminosity of Seyfert nuclei previously (Uryson 2001, 2004): $(L_{\rm CR})_{\rm S} \approx 10^{40}$ erg s^{-1} for $\chi = 3$ in the power-law initial CR spectrum and $(L_{\rm CR})_{\rm S} \approx 10^{42}$ erg s^{-1} for $\chi = 3.1$. The actual power spent on the CR acceleration in a source is a factor of $\sim$300 higher due to the curvature radiation of particles in the source.

Let us estimate the observed CR luminosity for BL Lac objects $(L_{\rm CR})_{\rm BL\ LAC}$:

$$(L_{\rm CR})_{\rm BL\ LAC} = U_{\rm CR}/(NT), \tag{8}$$

where $U_{\rm CR}$ is the total energy of the CRs emitted by BL Lac objects, N is the total number of BL Lac objects, and T is the CR lifetime. We can determine $U_{\rm CR}$ from the energy balance equation:

$$U_{\rm CR} = (U_{\rm CR})_{\rm measured} + (U_{\rm CR})_{\rm lost}, \tag{9}$$

where $(U_{\rm CR})_{\rm measured}$ is the energy of the CRs that reached the air shower array, and $(U_{\rm CR})_{\rm lost}$ is the CR energy that was lost during the CR propagation from the source to the air shower array. The initial CR energy in the source is $E_0 = 10^{21}$ eV; the bulk of the CRs on the air shower array have an energy of $E = 5 \times 10^{19}$ eV. Assuming that

$$(U_{\rm CR})_{\rm measured}/U_{\rm CR} \approx E/E_0 \approx 0.05, \tag{10}$$

we obtain

$$U_{\rm CR} \approx 20(U_{\rm CR})_{\rm measured}. \tag{11}$$

We define $(U_{\rm CR})_{\rm measured}$ as

$$(U_{\rm CR})_{\rm measured} = \int\limits_E I(E)EdE4\pi/cV, \tag{12}$$

where $I(E)$ is the computed intensity of the CRs from BL Lac objects, and V is the CR-filled volume. The integral in (12) is equal to 4 eV cm^{-2} s^{-1} sr^{-1}. Most of the BL Lac objects have redshifts $z \le 0.35$ (see Fig. 2); i.e., they are $r \le 1000$ Mpc away. The CRs emitted by these sources reach an air shower array in a time $T \le 2 \times 10^{17}$ s. Assuming that the CRs fill a sphere with a radius $r \approx 1000$ Mpc and reach an air shower array in a time $T \approx 2 \times 10^{17}$ s, we find that the total power of the sources is $U_{\rm CR}/T \approx 2 \times 10^{44}$ erg s^{-3}. The number of sources at redshifts $z \le 0.35$ is $N \approx 100$ (Veron-Cetty and Veron 2001). Therefore, the CR luminosity of a single source is $(L_{\rm CR})_{\rm BL\ LAC} \approx 2 \times 10^{42}$ erg s^{-3}. (The number of BL Lac objects may be much larger; the luminosity $(L_{\rm CR})_{\rm BL\ LAC}$ is then lower than the value obtained above.)

The power spent on the CR acceleration in a source is higher than its observed value, 2×10^{48} erg s^{-3}, because we assumed in our estimates that the initial particle energy is 10^{21} eV, while these particles are accelerated in the source up to 10^{27} eV. According to the model by Kardashev (1995), CRs emerge from a source with an energy of 10^{21} eV due to the curvature losses, and the bulk of the energy is spent on gamma-ray radiation.

DISCUSSION

The maximum CR energy is 10^{21} eV, irrespective of where they were accelerated, in Seyfert nuclei or in BL Lac objects. This energy is close to the values obtained in the models by Haswell *et al.* (1992), Berezinsky *et al.* (1997), and Totani (1998): $\sim 10^{21}$ eV for the CRs accelerated in an accretion disk around a black hole with a mass of $\sim 10^7 M_\odot$, $\sim 3 \times 10^{21}$ eV if the particles are produced in the decays of metastable superheavy particles of cold dark matter, and $\sim 10^{21}$ eV if the CRs are accelerated in gamma-ray bursts. The maximum accelerated-particle energy of 10^{21} eV was also obtained by Aharonian *et al.* (2002) and Medvedev (2003). The value of $\sim 10^{20}$ eV predicted in the model by Kichigin (2003) appears to be incorrect. In this model, CRs are accelerated in the galactic magnetic fields by a surfatron mechanism. However, particles at energies of 10^{19} eV are not confined by the Galactic magnetic fields, and their capture by suitable (for the subsequent surfatron acceleration) shock waves probably becomes impossible.

CONCLUSIONS

The observed CR luminosity for Seyfert nuclei is $(L_{\rm CR})_{\rm S} \approx 10^{40}$ erg s^{-1} if $\chi = 3$ in the power-law initial CR spectrum; for BL Lac objects, the observed CR luminosity is $(L_{\rm CR})_{\rm BL\,LAC} \approx 2 \times 10^{42}$ erg s^{-3}. The power spent on the CR acceleration in sources is much higher: 3×10^{42} erg s^{-3} for Seyfert nuclei and 2×10^{48} erg s^{-3} for BL Lac objects. The bulk of the energy lost in the source is spent on gamma-ray radiation.

The model in which CRs are accelerated with a power-law initial spectrum in nearby Seyfert nuclei satisfactorily describes the AGASA, HiRes, Fly's Eye, Haverah Park, and Yakutsk measurements. Data from the air shower arrays, except for HiRes, also confirm the model in which CRs are accelerated with a monoenergetic initial spectrum in BL Lac objects. The maximum CR energy is 10^{21} eV.

The models for both far and nearby sources satisfactorily describe the measured CR spectrum. Consequently, there is no paradox in the fact that far BL Lac objects have been identified as possible CR sources. In addition, in the model at $E \geq 5 \times 10^{19}$ eV, the spectrum of the particles arrived from nearby Seyfert nuclei is similar to the particle spectrum from far BL Lac objects. Therefore, analyzing the spectrum in this energy range, we cannot determine whether it has a blackbody cutoff.

It follows from these results that the ultrahigh-energy CR spectrum can be an additional test for the models of sources used here: whether the acceleration conditions in them are indeed such that the initial spectrum is monoenergetic in BL Lac objects and a power law in Seyfert nuclei.

The ultrahigh-energy CR spectrum is determined with a higher energy resolution and a larger statistic in HiRes, Auger, and Telescope Array measurements as well as in satellite measurements (Nagano and Watson 2000; Chechin *et al.* 2002).

ACKNOWLEDGMENTS

I wish to thank N.S. Kardashev for his discussion of the AGN models and V.A. Tsarev for his discussion of the ultrahigh-energy CR data. I am grateful to the referees for their remarks.

REFERENCES

1. F. A. Aharonian, A. A. Belyanin, E. V. Derishev, *et al.*, Phys. Rev. D **66**, 023005 (2002).
2. J. N. Bahcall and E. Waxman, Phys. Lett. B **556**, 1 (2003).
3. V. S. Berezinsky, S. V. Bulanov, V. L. Ginzburg, *et al., Astrophysics of Cosmic Rays,* Ed. by V. L. Ginzburg (Nauka, Moscow, 1990) [in Russian].
4. V. S. Berezinsky and S. I. Grigor'eva, Zh. Éksp. Teor. Fiz. **93**, 812 (1988).
5. V. S. Berezinsky, S. I. Grigor'eva, and V. A. Dogel', Zh. Éksp. Teor. Fiz. **96**, 798 (1989) [Sov. Phys. JETP **69**, 453 (1989)].
6. V. Berezinsky, M. Kachelries, and A. Vilenkin, Phys. Rev. Lett. **79**, 4302 (1997).
7. D. Bird, S. C. Corbato, H. Y. Dai, *et al.*, Astrophys. J. **441**, 144 (1995).
8. G. R. Blumenthal, Phys. Rev. D **1**, 1596 (1970).
9. V. A. Chechin, E. L. Feinberg, K. A. Kotelnikov, *et al.*, Nucl. Phys. B (Proc. Suppl.) **113**, 111 (2002).
10. D. S. Gorbunov, P. G. Tinyakov, I. I. Tkachev, and S. V. Troitsky, Astrophys. J. Lett. **577**, L93 (2002).
11. K. Greisen, Phys. Rev. Lett. **16,** 748 (1966).
12. C. A. Haswell, T. Tajima, and J.-I. Sakai, Astrophys. J. **401**, 495 (1992).
13. G. T. Hill and D. N. Shramm, Phys. Rev. D **31**, 564 (1985).
14. A. M. Hillas, Can. J. Phys. **46**, 5623 (1968).
15. N. S. Kardashev, Mon. Not. R. Astron. Soc. **276**, 515 (1995).
16. N. G. Kichigin, Dokl. Akad. Nauk **392,** 470 (2003) [Dokl. Phys. **48**, 565 (2003)].
17. M. V. Medvedev, Phys. Rev. E **67**, 045401 (2003).
18. M. Nagano and A. A. Watson, Rev. Mod. Phys. **72**, 689 (2000).
19. Particle Data Group, Phys. Rev. D **69**, 269 (2002).
20. Yu. P. Pskovskii, *Space Physics,* Ed. by S. B. Pikel'ner (Sov. Éntsiklopediya, Moscow, 1990), p. 569 [in Russian].
21. J. L. Puget, F. W. Stecker, and J. H. Bredekamp, Astrophys. J. **205**, 638 (1976).

22. K. Shinozaki, M. Chikawa, M. Fukushima, *et al., Proc. of the 28th ICRC* (2003), p. 401.
23. F. W. Stecker, Phys. Rev. Lett. **21**, 1016 (1968).
24. F. W. Stecker, Phys. Rev. Lett. **80**, 1816 (1998).
25. T. Totani, Astrophys. J. Lett. **502**, L13 (1998).
26. A. V. Uryson, Pis'ma Zh. Éksp. Teor. Fiz. **64**, 71 (1996) [JETP Lett. **64**, 77 (1996)].
27. A. V. Uryson, Pis'ma Zh. Éksp. Teor. Fiz. **65**, 729 (1997) [JETP Lett. **65**, 763 (1997)].
28. A. V. Uryson, Astron. Astrophys. Trans. **20**, 347 (2001a).
29. A. V. Uryson, Pis'ma Astron. Zh. **27**, 901 (2001b) [Astron. Lett. **27**, 775 (2001b)].
30. A. V. Uryson, Astron. Astrophys. Trans. **23**, 43 (2004a).
31. A. V. Uryson, Astron. Zh. **81**, 99 (2004b) [Astron. Rep. **48**, 81 (2004b)].
32. M.-P. Veron-Cetty and P. Veron, Astron. Astrophys. **374**, 92 (2001).
33. S. Yoshida and M. Teshima, Progr. Theor. Phys. **89**, 833 (1992).
34. G. T. Zatsepin and V. A. Kuzmin, Pis'ma Zh. Éksp. Teor. Fiz. **4**, 114 (1966) [JETP Lett. **4**, 78 (1966)].

Translated by V. Astakhov

Astronomy Letters, Vol. 30, No. 12, 2004, pp. 824–833. Translated from Pis'ma v Astronomicheskiĭ Zhurnal, Vol. 30, No. 12, 2004, pp. 905–914.

Broadband Observations of the Transient X-ray Pulsar SAX J2103.5+4545

E. V. Filippova[1], A. A. Lutovinov[1*], P. E. Shtykovsky[1], M. G. Revnivtsev[1,2], R. A. Burenin[1], V. A. Aref'ev[1], M. N. Pavlinsky[1], and R. A. Sunyaev[1,2]

[1]*Space Research Institute, Russian Academy of Sciences, Profsoyuznaya ul. 84/32, Moscow, 117810 Russia*

[2]*Max Planck Institut für Astrophysik, Karl Schwarzschild Str. 1, Postfach 1317, D-85741 Garching, Germany*

Received July 1, 2004

Abstract—We investigated the optical, X-ray, and gamma-ray variability of the pulsar SAX J2103.5+4545. Our timing and spectral analyses of the X-ray and gamma-ray emissions from the source using RXTE and INTEGRAL data show that the shape of its spectrum in the energy range 3–100 keV is virtually independent of its intensity and the orbital phase. Based on XMM-Newton data, we accurately (5″) localized the object and determined the optical counterpart in the binary. We placed upper limits on the variability of the latter in the $H\alpha$ line on time scales of the orbital and pulse periods, respectively. © *2004 MAIK "Nauka/Interperiodica"*.

Key words: *X-ray pulsars, neutron stars, Be stars.*

INTRODUCTION

The X-ray transient SAX J2103.5+4545 was discovered by the BeppoSAX observatory during its outburst in 1997 (Hulleman *et al.* 1998). Almost immediately, coherent pulsations with a period of ≈358 s were detected in the source, which allowed it to be classified as a transient X-ray pulsar. RXTE observations of the source during the next outburst in 1999 revealed another type of periodicity attributable to the orbital motion of the compact object. Based on these observations, Baykal *et al.* (2000) found the pulsar to be a member of a binary and to have an elliptical orbit with an eccentricity of $e \simeq 0.4$ and an orbital period of ∼12.68 days. Subsequently, Baykal *et al.* (2002) estimated the distance to the source, ∼3.2 kpc, and its X-ray luminosity, $L_{\rm x} \sim 6 \times 10^{34}$–$10^{36}$ erg s^{-1}.

An analysis of the light curves for the object showed that the intensity of the pulsar is highly variable within one orbital cycle and peaks near the periastron (Baykal *et al.* 2000). Such behavior of the light curves is typical of binaries with relatively high eccentricities and high-mass companions—early-type (O–B) stars. Hulleman *et al.* (1998) suggested that the star HD 200709 could be the optical counterpart. However, the position of this star outside the BeppoSAX error region and its spectral type (B8 V) made this candidacy highly questionable. Using the localizations of SAX J2103.5+4545 by the BeppoSAX observatory and by the IBIS and JEM-X telescopes of the INTEGRAL observatory as well as the observations of this region at the Skinakas observatory (Crete), Reig *et al.* (2004) pointed to another candidate; their error region for the source is then ∼30″.

In this paper, we make an attempt to investigate the variability of the source on time scales from several hundred seconds (the spin period of the neutron star) to several days (the orbital period of the binary) over a wide energy range, from optical (RTT-150) to hard X-rays (RXTE and INTEGRAL). In addition, using XMM-Newton data, we were able to increase the localization accuracy for the X-ray pulsar to 5″.

OBSERVATIONS

RTT-150

Optical observations of SAX J2103.5+4545 were performed in the fall of 2003 with the Russian–Turkish 1.5-m telescope (RTT-150, TUBITAK National Observatory, Turkey, Mount Bakyrly, 2547 m, $2^{\rm h}01^{\rm m}20^{\rm s}$ E, 36°49′30″ N). The observations were carried out with a back-illuminated Andor Technologies 2 × 2 CCD array placed at the Cassegrain focus of the telescope (1 : 7.7). A median zero-exposure frame and dark current were subtracted from all images, and then the images were divided by a flat field. We reduced the images using the IRAF (Image

*E-mail: aal@hea.iki.rssi.ru

Reduction and Analysis Facility) standard software package[1] and our own software.

XMM-Newton

To improve the celestial coordinates of the source, we used data from the XMM-Newton observatory. Its main instruments are three grazing-incidence X-ray telescopes with (MOS1, MOS2, PN) CCD arrays placed at the foci. The typical angular size of a point source on the detectors is on the order of several arcseconds, which allows the coordinates of the source to be determined with high accuracy. Here, we used data from the EPIC MOS instruments operating in the energy range 0.15–12 keV.

INTEGRAL

The International gamma-ray observatory INTEGRAL (Winkler *et al.* 2003) was placed into a high-apogee orbit by the Russian Proton Launcher from the Baikonur Cosmodrome on October 17, 2002 (Eismont *et al.* 2003). The payload of the satellite includes the SPI gamma-ray spectrometer, the IBIS gamma-ray telescope, the JEM-X X-ray monitor, and the OMC optical monitor (for more details, see Winkler *et al.* (2003) and references therein). We used data from the IBIS telescope, its upper ISGRI detector (Lebrun *et al.* 2003), and data from the JEM-X X-ray monitor (Lund *et al.* 2003). Both instruments operate on the principle of a coded aperture. The field of view is $29° \times 29°$ (total) and $9° \times 9°$ (the full-coding region) for IBIS and 4° in diameter (the full-coding region) for JEM-X.

We used the publicly accessible INTEGRAL calibration observations of the Cyg X-1 region performed in December 2002. Preliminary results of the analysis of the INTEGRAL observations for the pulsar SAX J2103.5+4545 were presented by Lutovinov *et al.* (2003).

The standard OSA-3.0 software package provided by the INTEGRAL Science Data Center (ISDC)[2] was used for the timing analysis of ISGRI data and the analysis of JEM-X data. A method described by Revnivtsev *et al.* (2004) was used to reconstruct the images and to construct the spectrum of the source from ISGRI data. An analysis of the observational data for the Crab Nebula indicates that the technique used allows the spectrum of the source to be accurately reconstructed; the systematic uncertainty is ~10% for the absolute normalization of the flux obtained and ~5% in each energy channel when reconstructing the spectrum of the source. The latter was added as a systematic uncertainty in the spectral analysis of the source in the XSPEC package.

[1] http://tucana.tuc.noao.edu/

[2] http://isdc.unige.ch

RXTE

For our comparative analysis of the INTEGRAL results, we used the simultaneous observations of the pulsar SAX J2103.5+4545 that were performed by the RXTE observatory (Bradt *et al.* 1993) in December 2002 (Obs. ID. 70082-02-43–70082-02-52) and that are publicly accessible.

The main instruments of the RXTE observatory are the PCA and HEXTE spectrometers that jointly cover the energy range 3–250 keV. The PCA spectrometer is a system of five xenon proportional counters. The PCA field of view is bounded by a circular collimator with a radius of 1° at half maximum, the operating energy range is 3–20 keV, the effective area at energies of 6–7 keV is $\sim$6400 cm^2, and the energy resolution at these energies is ~18%. The HEXTE spectrometer is a system of two independent packages of four phoswich NaI(Tl)/CsI(Na) detectors rocking with a period of 16 s for the observations of off-source areas at a distance of 1.°5 from the source. At each specific time, the source can be observed only by one of the two detector packages; thus, the effective area of the HEXTE detectors is $\sim$700 cm^2. The operating energy range of the spectrometer is ~15–250 keV.

The standard FTOOLS/LHEASOFT 5.3 software package was used to reduce the RXTE data. In our spectral analysis of the PCA data in the energy range 3–20 keV, we introduced a systematic uncertainty of 1%.

LOCALIZATION AND DETERMINATION OF THE OPTICAL COUNTERPART

Using INTEGRAL observations, we obtained an image of the sky region with the source in the energy range 18–60 keV (Fig. 1). The position of the source can be determined from these data with an accuracy of $\sim 1'$. This accuracy is too low to unambiguously determine the optical counterpart to the source. Reig *et al.* (2004) made an attempt to improve the localization accuracy using the overlapping BeppoSAX and INTEGRAL error regions.

Here, we used archival XMM-Newton (Obs.Id 0149550401) data to improve the position of SAX J2103.5+4545. During these observations, the telescope operated in fast-variability mode, in which information is read from the CCD array only along one of the axes. Compared to the standard modes, this mode allows the time resolution to be increased significantly, but at the same time, it has a shortcoming: there is no direct spatial information. To determine the celestial coordinates of the source, we used data from two detectors, MOS1 and MOS2, in which information is read along the mutually perpendicular directions. We used the following algorithm:

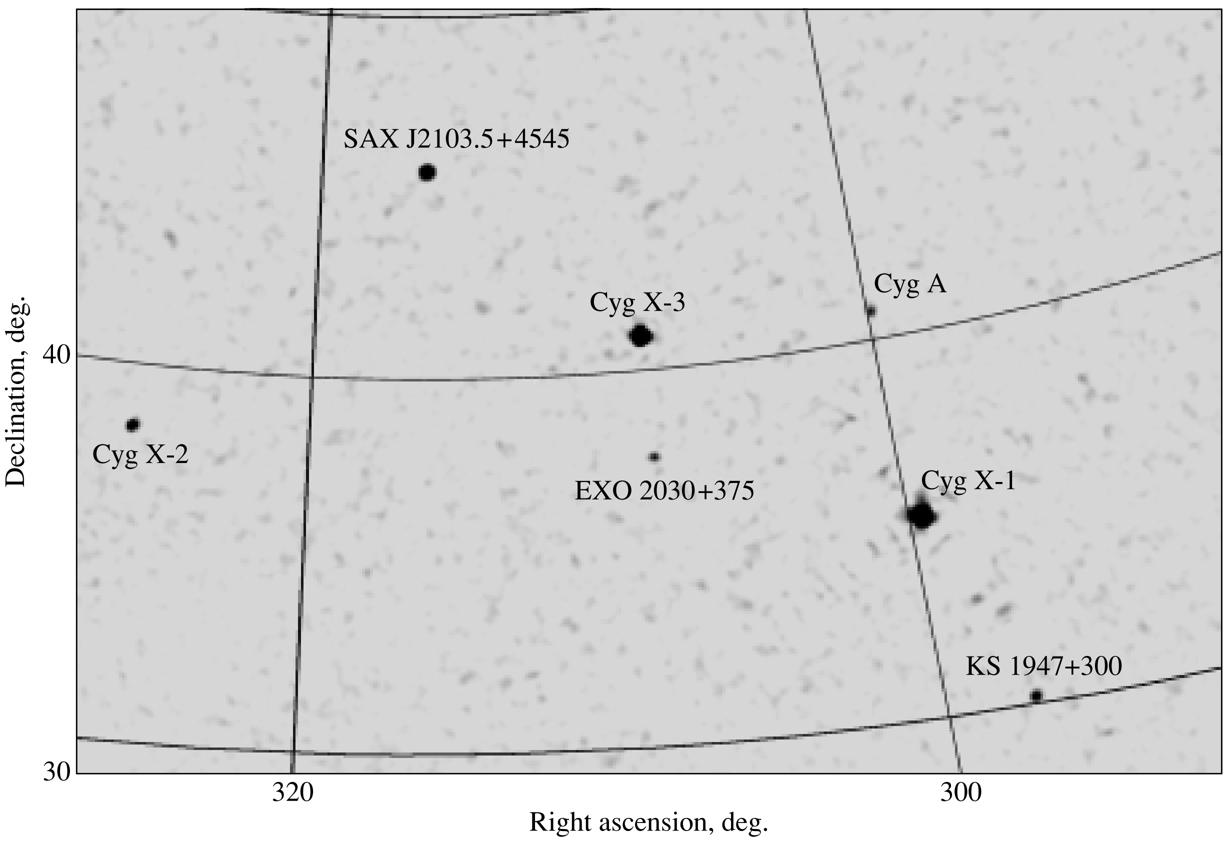

Fig. 1. The region of ISGRI observations of SAX J2103.5+4545 in the energy range 18–60 keV.

(1) We determined the detector coordinate of the centroid of the one-dimensional photon distribution for each of the detectors ($RAWX1_{src}$, $RAWX2_{src}$).

(2) We generated a set of celestial coordinates in the region where the source was presumably located. Subsequently, this set was transformed into two sets of detector coordinates (one for MOS1 and the other for MOS2) using the standard esky2det code from the Science Analysis System (SAS) of the XMM observatory.

(3) From the set of celestial coordinates, we chose those for which the detector coordinates (RAWX1, RAWX2) corresponded to those of the source ($RAWX1_{src}$, $RAWX2_{src}$).

As a result, we obtained the following coordinates of the source: $\alpha = 21^h03^m36^s$ and $\delta = 45^d45^m07^s$. The localization accuracy is determined by the response function of the telescope, the astrometric referencing accuracy, and the peculiarities of our coordinate determination procedure. We obtained $\sigma_{\rm RADEC} = 5''$ as an estimate of the total error.

The RTT-150 map of the sky region around the pulsar SAX J2103.5+4545 is shown in Fig. 2. The circles indicate the error regions determined from BeppoSAX and XMM-Newton data. It clearly follows from this figure that the optical counterpart to SAX J2103.5+4545 is determined with a high degree of confidence from the results of our analysis. It is the star shown in Fig. 2. This result agrees with that obtained by Reig *et al.* (2004). The RTT-150 measurements yield the magnitudes $R = 13.605$ and $V = 14.20$ for this star. The derived color is consistent with the emission from an O–B star at an interstellar reddening of $A_V = 3.12$.

TIMING ANALYSIS

Variability on Time Scales of the Orbital Period

Lutovinov *et al.* (2003) showed that the intensity of the source in the hard energy ranges 15–40 and 40–100 keV is highly variable and depends on the orbital phase. Figure 3a presents the light curve of the pulsar constructed from ISGRI data in the energy range 18–60 keV. Each point was obtained by averaging over five individual pointings and has an exposure time of ∼15 ks. To depict the dependence of the source's intensity more conveniently, orbital phases are plotted along the horizontal axis together with the time (the parameters of the binary were taken

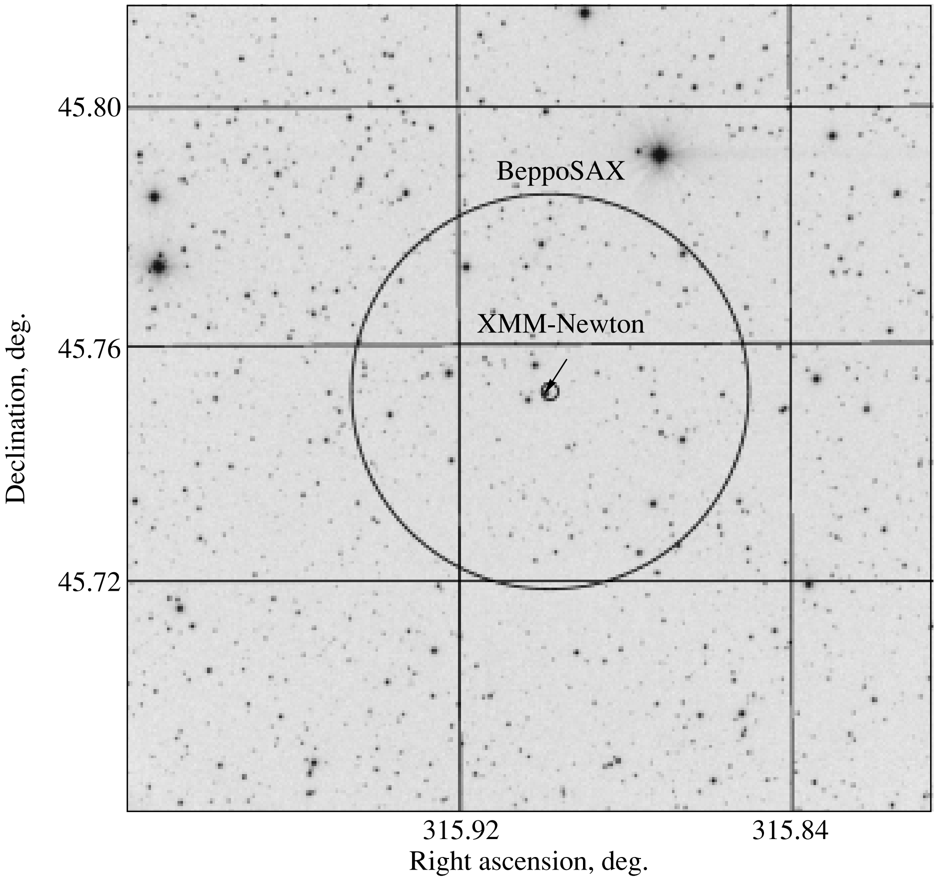

Fig. 2. The region of ground-based RTT-150 R-band observations of SAX J2103.5+4545. The arrow indicates the optical counterpart to the pulsar; its error region, determined here from XMM-Newton data, is highlighted.

from Baykal *et al.* (2000)). The flux from the binary is at a maximum (∼40–50 mCrab) near orbital phases of 0.55–0.75 and decreases to ∼10–20 mCrab at phases of 0.1–0.2. As was noted by Lutovinov *et al.* (2003), the observed hard X-ray light curve follows somewhat closely the light curve in the standard X-ray energy range (Baykal *et al.* 2000).

The variability of the source was also studied at optical wavelengths on time scales of the order of the orbital period, ∼12.6 days. For this purpose, the source's field was imaged in the R band (the band was chosen arbitrarily) in the second half of October and November 2003 on each night, where possible. The derived light curve is shown in Fig. 3b. We found no variability of the source related to its orbital motion in the binary; the upper limit on its amplitude is ∼1%.

Variability on Time Scales of the Pulsation Period

The periods of X-ray pulsars are known to be variable and subject to both long-term changes and small-scale fluctuations (see, e.g., Nagase 1989; Lutovinov *et al.* 1994; Bildsten *et al.* 1997). While monitoring SAX J2103.5+4545 during its 1999 outburst, Baykal *et al.* (2002) found a significant spin-up of the neutron star, with the observed spin-up rate being proportional to the flux from the source. Figure 4 shows the changes in the pulsar's period throughout the history of its observations by different observatories.

An epoch-folding technique was used to determine the pulsar's period during the INTEGRAL observations. The source's light curve in the energy range 20–100 keV with a time step of 40 s was constructed from ISGRI data using standard software and corrected for the orbital motion of the neutron star in the binary using known orbital parameters (Baykal *et al.* 2000). The pulsation period calculated in this way was 355.10 ± 0.04 s. Figure 5 shows the χ^2 periodogram for the source's light curve obtained by searching for flux pulsations from it. The error in the period was determined by the Monte Carlo method from an analysis of the simulated light curves.

Figure 6a shows the phase light curve for the pulsar SAX J2103.5+4545 constructed from INTEGRAL data in the energy range 20–100 keV.

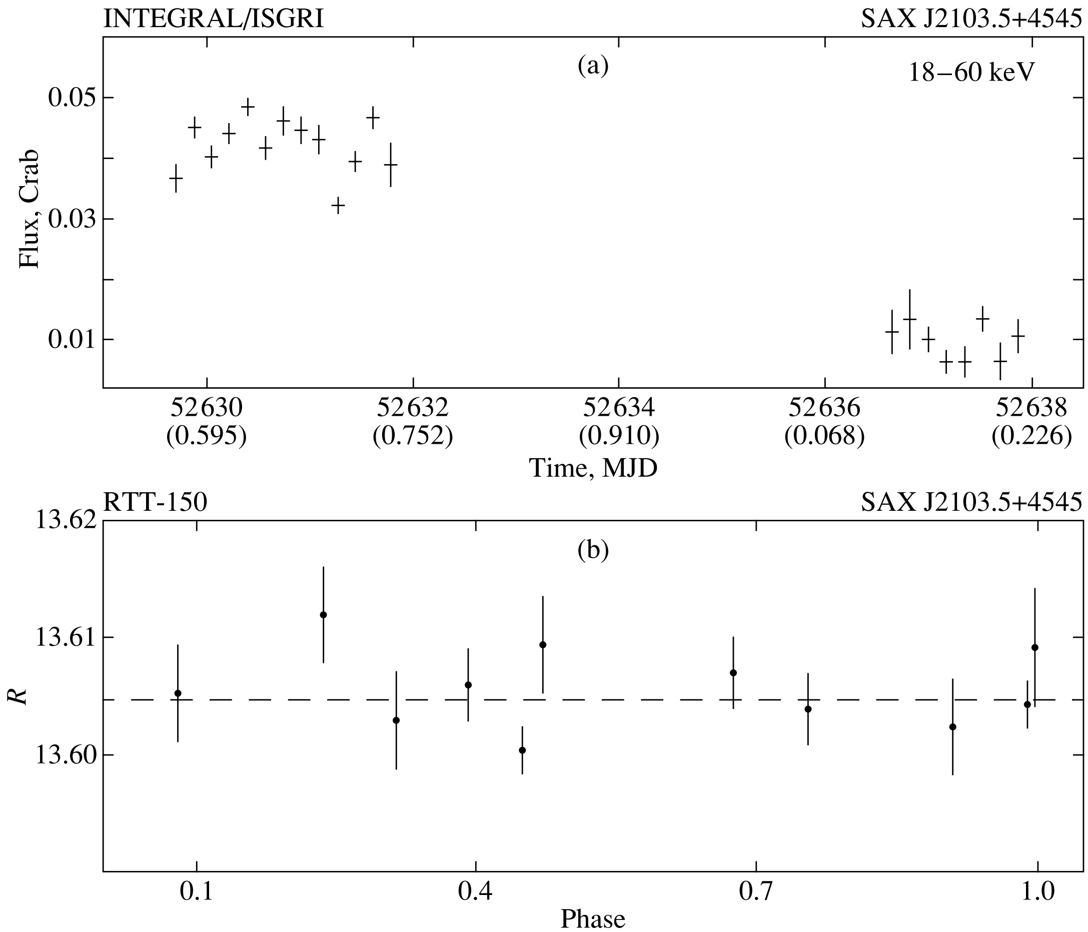

Fig. 3. Light curve of the pulsar SAX J2103.5+4545 on time scales of the orbital period: constructed from ISGRI data in the energy range 18–60 keV (a) and from ground-based RTT-150 R-band observations in October–November 2003 (b). For convenience, optical phases are plotted along the horizontal axis. The errors correspond to one standard deviation. The dashed line indicates the mean R magnitude of the star.

It has a single-peaked shape extended over the entire phase cycle of the pulsar's period. The intensity rapidly rises and smoothly decays. Baykal *et al.* (2000) and Inam *et al.* (2004) provided the source's pulse profiles for different soft X-ray energy ranges. Our hard X-ray pulse profile differs slightly from the previous soft X-ray profiles, whose peaks occupy only half of the cycle, and the rise in intensity is smoother than its decay. Based on the INTEGRAL data reduction results, we failed to estimate the pulse fraction in the hard energy range, because the standard software used to construct the light curves of sources does not properly estimate the contribution from the background radiation on the detector. Therefore, to estimate this pulse fraction, we used the HEXTE/RXTE data obtained over the same time interval as the INTEGRAL data. According to these data, the pulse fraction is $\sim$20 $\pm$5%. In the soft energy range 0.9–11 keV, the pulse fraction is 50.9 ± 0.3% (Inam *et al.* 2004).

The variability of the source on time scales of its X-ray pulsations was also studied at optical wavelengths, in an $H\alpha$ filter. Observations of such variability in other high-mass binaries with pulsars were reported previously (e.g., in the object X Persei; Mazeh *et al.* 1982). The $H\alpha$ observations of the source were performed on November 18, 2003 (52961 MJD), with the RTT-150 telescope. The observations were carried out for 1.1 h with a time resolution of $\sim$15 s.

Since the source has exhibited a nonuniform spin-up of the neutron star throughout the history of its observations, to calculate the expected period at the epoch of our optical observations, we have obtained a conservative estimate of the mean spin-up rate as follows. For all of the possible pairs of points in Fig. 4, we calculated the spin-up rate between

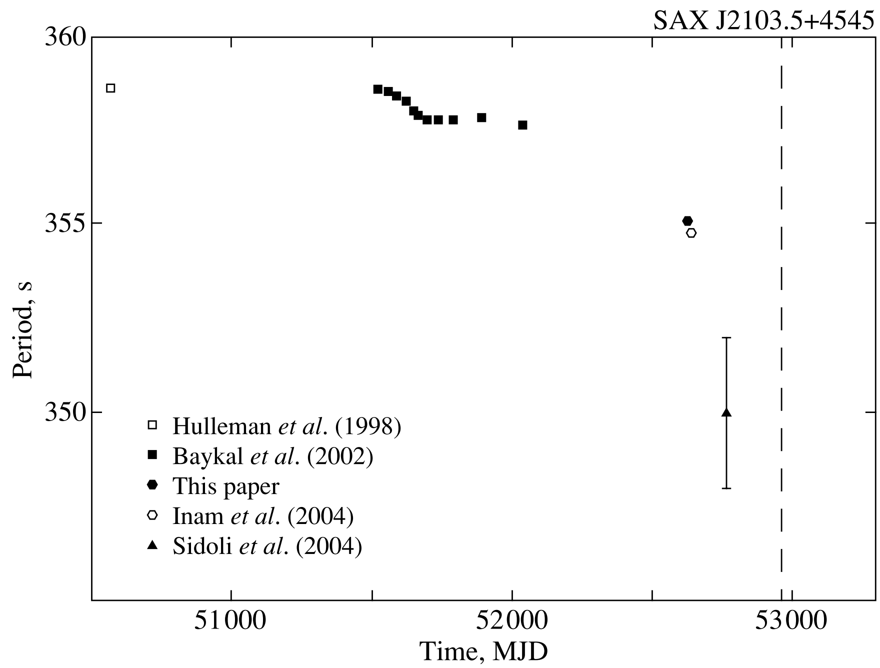

Fig. 4. Changes in the pulsation period of SAX J2103.5+4545 throughout the history of its observations by different observatories. The dashed line marks the epoch of optical observations.

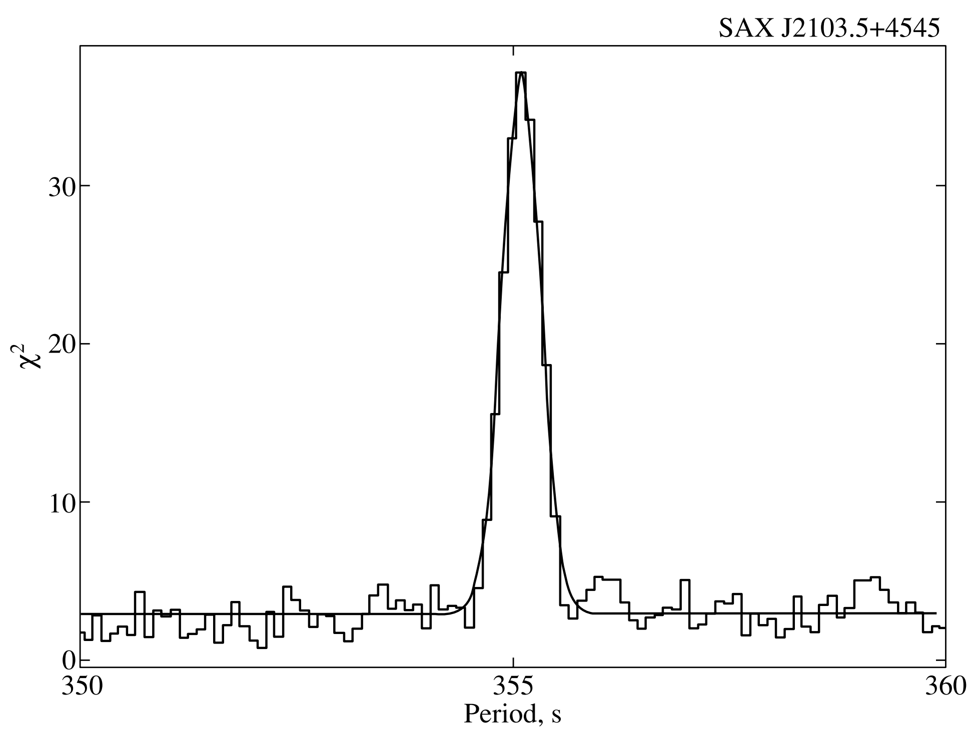

Fig. 5. χ^2 periodogram obtained by searching for flux pulsations from SAX J2103.5+4545 by the epoch-folding technique. The solid line indicates the Gaussian best fit.

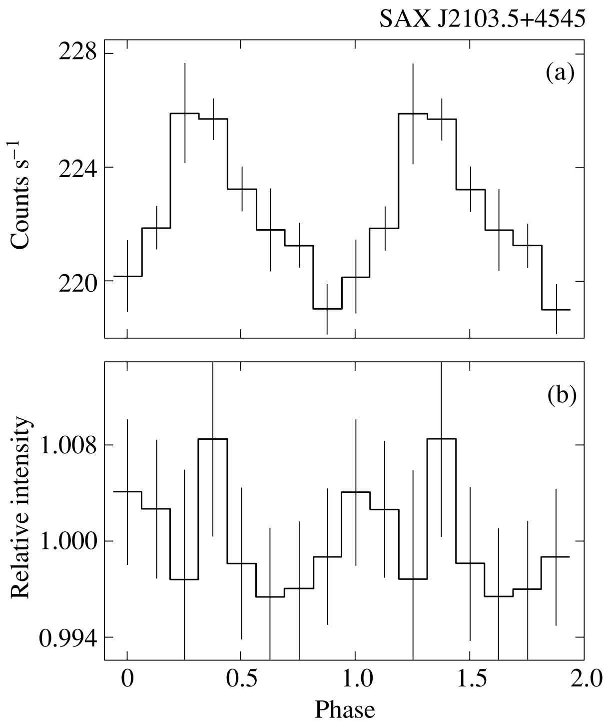

Fig. 6. Pulse profiles for the pulsar SAX J2103.5+4545 in the energy range 20–100 keV as constructed from IBIS/ISGRI data (the background was not subtracted) (a) and in an $H\alpha$ filter as constructed from the RTT-150 observations on November 18, 2003 (b).

them and then determined its mean value, $\dot{P}/P \sim 3.2 \times 10^{-3}$ yr^{-1}. In this procedure, we excluded the period measured by the INTEGRAL observatory in the series of observations in May–June 2003 (Sidoli *et al.* 2004). This decision was justified in part by the large uncertainty in the measure period at this epoch and by the fact that, if the presumed spin-up rate of the pulsar was estimated from our measurements and from the measurements by Inam *et al.* (2004) and Sidoli *et al.* (2004), then the value obtained would be several times higher than the maximum spin-up rate observed by Baykal *et al.* (2002) during the 1999 outburst. It is important to note that the 3–20 keV flux from the source in December 2003–April 2004 was comparable to its flux in 1999–2000. The ultimate answer to the question concerning the behavior of the spin-up rate of the neutron star in the binary SAX J2103.5+4545 may be given after analyzing the large set of RXTE observations of this object in 2003 that is not yet publicly accessible.

The presumed pulsation period at the epoch of our optical observations estimated by the method described above is 354.02 s. The $H\alpha$ light curve of the optical counterpart folded with this period is shown in Fig. 6b. We found no variability of the source in the $H\alpha$ band; the upper limit is $\sim$1%. The zero phase of the X-ray pulse profile and the presumed zero phase at the epoch of our optical observations calculated using the procedure described above were brought into coincidence.

SPECTRAL ANALYSIS

As we noted above, the intensity of the source varies greatly with the orbital motion of the neutron star in the binary. Therefore, we performed a spectral analysis of the pulsar emission for various orbital phases of the binary with the goal of finding the possible dependence of the source's spectrum on its intensity and its position in the orbit. Such an analysis was performed by Baykal *et al.* (2002) using RXTE data for the standard X-ray energy range 3–20 keV. In contrast, we investigated the behavior of the source over a wide energy range up to $\sim$100 keV using INTEGRAL and RXTE data.

We used JEM-X and ISGRI data to construct the spectrum of the source from its INTEGRAL observations in the energy ranges 6–20 and 20–100 keV, respectively. To test the validity of the normalization of the JEM-X spectra, we analyzed a series of spectra for the Crab Nebula. Where possible, we took observations when this object was within the same areas of the JEM-X field of view as our source. We found that the shape of the spectrum for the Crab Nebula is reconstructed satisfactorily, while the normalization proves to be underestimated by a factor of $\sim$1.6. This factor was used for the correction of the normalization of the JEM-X spectrum for the source. Our analysis of the source's spectrum at various orbital phases revealed no appreciable deviations of its shape over a wide energy range either. This allowed us to subsequently study the source's average spectrum shown in Fig. 7. For comparison, this figure also shows the pulsar's spectrum constructed from the RXTE observations performed over the same period as the INTEGRAL observations. We used PCA and HEXTE detector data for the energy ranges 4–20 and 20–70 keV, respectively.

The spectrum of the X-ray pulsar SAX J2103.5+4545 is typical of this class of objects and can be described by a simple power law with an exponential high-energy cutoff. This model has long and widely been used to fit the spectra of X-ray pulsars (White *et al.* 1983). Based on XMM-Newton data, Inam *et al.* (2004) measured the neutral hydrogen column density ($N_{\rm H}$). Depending on the model used to describe the pulsar's spectrum, this parameter varies over the range $N_{\rm H} = (0.6–0.9) \times 10^{22}$ atoms cm^{-2}, in agreement with our optical measurements (see above). Since there are no INTEGRAL data at energies below 6 keV in our

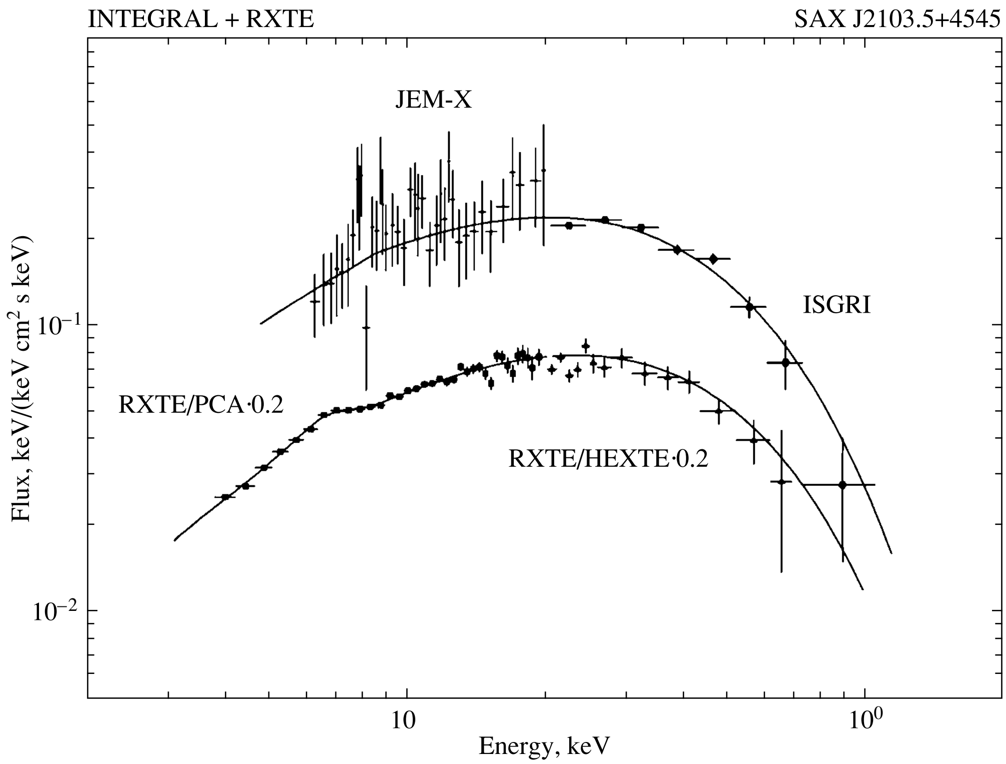

Fig. 7. Energy spectrum of the pulsar SAX J2103.5+4545 as constructed from INTEGRAL and RXTE data. The normalization of the RXTE spectrum was multiplied by 0.2. The lines indicate the model fits to the spectra with the best-fit parameters (see the table).

Best-fit parameters for the spectrum of the pulsar SAX J2103.5+4545

Parameters	Values
Derived from INTEGRAL data	
N_{H}, 10^{22} cm^{-2}	0.9 (fixed)
Photon index Γ	1.04 ± 0.15
Cutoff energy E_{cut}, keV	8.5 ± 2.4
e-folding energy E_{fold}, keV	21.37 ± 2.75
χ^2 (degree of freedom)	1.21
Derived from RXTE data	
N_{H}, 10^{22} cm^{-2}	0.9 (fixed)
Photon index Γ	0.979 ± 0.066
Cutoff energy E_{cut}, keV	6.97 ± 1.26
e-folding energy E_{fold}, keV	22.98 ± 1.73
Fe line center, keV	6.34 ± 0.32
Fe line width, keV	0.81 ± 0.21
Fe line intensity, photons cm^{-2} s^{-1}	$(1.2 \pm 0.4) \times 10^{-3}$
χ^2 (degree of freedom)	0.99

case and since the RXTE sensitivity is lower (than the XMM-Newton sensitivity) at soft energies, we fixed N_{H} at 0.9×10^{22} atoms cm^{-2} in the subsequent analysis.

The table gives the best-fit parameters for the model fit to the source's spectrum described above for the INTEGRAL and RXTE data. The derived parameters for the two data sets are in good agreement among themselves and with the values from Baykal *et al.* (2002) and Inam *et al.* (2004), except for the e-folding energy that proved to be slightly lower. This may be because we greatly extended the energy range under study. Note also that the RXTE spectrum of the source exhibits a neutral iron line at an energy of 6.4 keV (see the table).

CONCLUSIONS

The transient X-ray pulsar SAX J2103.5+4545 is a member of a high-mass Be binary with a moderate eccentricity and the shortest orbital period known to date among all such binaries. Identifying the optical counterpart of the binary plays one of the most important roles in understanding the nature of binaries with compact objects and the processes that take place in them.

We have been able to localize the pulsar with an accuracy of $5''$ and to firmly establish its nature: an emission-line O–B star. We performed optical observations of this object with the RTT-150 telescope with the goal of finding its possible variability. We found no variability of the optical counterpart on time scales of the orbital period and the spin period of the pulsar; the upper limit on its amplitude is about 1% in both cases.

The X-ray pulsar has exhibited spin-up almost throughout the history of its observations, with the spin-up rate depending on the luminosity of the source (Baykal *et al.* 2002). During the INTEGRAL observations, the pulsation period was 355.10 ± 0.04 s. The pulse fraction decreases with increasing energy and is $\sim$20% in the energy range 20–100 keV.

Our analysis of the INTEGRAL and RXTE observational data for the pulsar shows that the source is detected at a statistically significant level up to energies of $\sim$100 keV. As in the standard X-ray energy range, the intensity of the source in the hard energy range also depends on the orbital phase of the binary and peaks near the periastron. At the same time, the shape of the source's spectrum remains virtually unchanged over a wide energy range (3–100 keV) and can be described by the standard (for X-ray pulsars) model: a simple power law with a high-energy cutoff and low-energy absorption.

We detected no features in the 3–100 keV spectrum of the source that could be interpreted as cyclotron lines. Thus, we can impose lower and upper limits on the magnetic field strength of the source: $B > 10^{13}$ G and $B < 3.6 \times 10^{11}$ G, respectively. We know X-ray pulsars with a weak magnetic field ($B \sim 10^{11}$ G), for example, SMC X-1 (see, e.g., Lutovinov *et al.* (2004) and references therein) and GRO J1744–28 (Rappaport and Joss 1997). The detection of type II X-ray bursts from them provides evidence that the magnetic field in these sources is weak. No such bursts are observed from the pulsar SAX J2103.5+4545. Baykal *et al.* (2002) estimated the magnetic field from the relationship between the rate of change in the pulsar's period and its parameters (Ghosh and Lamb 1979): $B \sim 12 \times 10^{12}$ G. Thus, most of the arguments suggest that the neutron star in the binary under consideration has a strong magnetic field.

ACKNOWLEDGMENTS

We thank E.M. Churazov, who developed the algorithms for IBIS data analysis and provided the software. We also thank S.V. Molkov and S.S. Tsygankov for help in reducing the JEM-X and RXTE data. This work was supported by the Ministry of Industry and Science (Presidential grant no. NSh-2083.2003.2 and project no. 40.022.1.1.1102) and the Russian Foundation for Basic Research (project no. 04-02-17276). We are grateful to the INTEGRAL Science Data Center (Versoix, Switzerland) and the Russian INTEGRAL Science Data Center (Moscow, Russia). The results of this work are based on observations of the INTEGRAL observatory, an ESA project with the participation of Denmark, France, Germany, Italy, Switzerland, Spain, Czechia, Poland, Russia, and USA. We also used data retrieved from the High-Energy Astrophysics Archive, The Goddard Space Flight Center. A.A.L., M.G.R., R.A.B., and M.N.P. thank the International Space Science Institute (ISSI, Bern) for support.

REFERENCES

1. A. Baykal, M. Stark, and J. Swank, Astrophys. J. Lett. **544**, L129 (2000).
2. A. Baykal, M. Stark, and J. Swank, Astrophys. J. **569**, 903 (2002).
3. L. Bildsten, D. Chakrabarty, J. Chiu, *et al.*, Astrophys. J., Suppl. Ser. **113**, 367 (1997).
4. H. V. Bradt, R. E. Rothschild, and J. H. Swank, Astron. Astrophys., Suppl. Ser. **97**, 355 (1993).
5. N. Eismont, A. Ditrikh, G. Janin, *et al.*, Astron. Astrophys. **411**, L37 (2003).
6. P. Ghosh and F. Lamb, Astrophys. J. **234**, 296 (1979).
7. F. Hulleman, J. in't Zand, and J. Heise, Astron. Astrophys. **337**, L25 (1998).
8. S. Inam, A. Baykal, J. Swank, *et al.*, Astrophys. J. (2004, in press); astro-ph/0402221.
9. F. Lebrun, J. P. Leray, P. Lavocat, *et al.*, Astron. Astrophys. **411**, L141 (2003).
10. N. Lund, S. Brandt, C. Budtz-Joergesen, *et al.*, Astron. Astrophys. **411**, L231 (2003).
11. A. A. Lutovinov, S. A. Grebenev, R. A. Sunyaev, and M. H. Pavlinsky, Pis'ma Astron. Zh. **20**, 631 (1994).

12. A. A. Lutovinov, S. V. Molkov, and M. G. Revnivtsev, Pis'ma Astron. Zh. **29**, 803 (2003) [Astron. Lett. **29**, 713 (2003)].
13. A. A. Lutovinov, S. S. Tsygankov, S. A. Grebenev, *et al.,* Pis'ma Astron. Zh. **30**, 58 (2004) [Astron. Lett. **30**, 50 (2004)].
14. T. Mazeh, R. Treffers, and S. Vogt, Astrophys. J. **256**, L13 (1982).
15. F. Nagase, Publ. Astron. Soc. Jpn. **41**, 1 (1989).
16. A. Rappaport and P. Joss, Astrophys. J. **486**, 435 (1997).
17. R. Reig, I. Negueruela, J. Fabregat, *et al.*, Astron. Astrophys. **421**, 673 (2004).
18. M. G. Revnivtsev, R. A. Sunyaev, D. A. Varshalovich, *et al.,* Pis'ma Astron. Zh. **30**, 430 (2004) [Astron. Lett. **30**, 382 (2004)].
19. L. Sidoli, S. Mereghetti, S. Larsson, *et al.*, in *Proceedings of the 5th INTEGRAL Workshop* (2004, in press); astro-ph/0404018.
20. N. White, J. Swank, and S. Holt, Astrophys. J. **270**, 771 (1983).
21. C. Winkler, T. J.-L. Courvoisier, G. Di Cocco, *et al.*, Astron. Astrophys. **411**, L1 (2003).

Translated by V. Astakhov

Astronomy Letters, Vol. 30, No. 12, 2004, pp. 834–842. Translated from Pis'ma v Astronomicheskiĭ Zhurnal, Vol. 30, No. 12, 2004, pp. 915–923.

Optical Spectra and Redshifts of Radio Sources from the Zelenchuk Survey

V. R. Amirkhanyan[1*], V. L. Afanas'ev[2], S. N. Dodonov[2], A. V. Moiseev[2], and V. P. Mikhailov[2]

[1]*Sternberg Astronomical Institute, Universitetskiĭ pr. 13, Moscow, 119992 Russia*

[2]*Special Astrophysical Observatory, Russian Academy of Sciences, Nizhniĭ Arkhyz, 357147 Karachaĭ-Cherkessian Republic, Russia*

Received April 20, 2004

Abstract—We performed spectroscopic observations of 22 radio sources from the Zelenchuk survey (Sternberg Astronomical Institute) using the 6-m and 1-m Special Astrophysical Observatory telescopes. For 18 objects, we determined the redshifts. Ten, seven, and one of these objects were identified with quasars, elliptical galaxies, and a Seyfert galaxy, respectively. Four radio sources have a continuum spectrum, and three of them are BL Lac objects. We failed to classify one object. © *2004 MAIK "Nauka/Interperiodica"*.

Key words: *active galactic nuclei, quasars, radio sources, redshift.*

INTRODUCTION

Producing a complete sample of radio sources and a subsequent study of these objects at optical wavelengths is a fruitful method of obtaining a list of extragalactic objects on the basis of which both statistical analyses and studies of individual objects can be carried out. This is because the overwhelming majority of radio sources with fluxes of several tens of millijanskys or more are extragalactic objects. A successful identification of radio sources from the Zelenchuk survey with extragalactic objects was demonstrated by Amirkhanyan *et al.* (1993) and Chavushyan *et al.* (2000, 2001). In the last three years, this work has been intensified in connection with the design and production of a new (SCORPIO) spectrograph at the Special Astrophysical Observatory (SAO) (Afanas'ev *et al.* 2001). This is a multifunction instrument that allows low-resolution spectra to be obtained over the entire optical wavelength range at once. The instrument has a spectral quantum efficiency of 30% at the sensitivity maximum, which makes it possible to take the spectra of 18–20-mag. objects with the 6-m SAO telescope even at poor seeing (up to 4″–5″) and noticeable cloudiness. The full automation of the instrument has allowed us to formalize the observing and data reduction processes as much as possible by turning them into routine procedures.

In this paper, we present new optical spectra of 22 radio sources from the Zelenchuk survey, for most of which we have been able to measure the redshifts and to perform their spectral classification.

THE SAMPLE OF RADIO SOURCES

For our optical observations, we drew two samples of radio sources from the Zelenchuk survey. The first sample included objects in the declination range 6°–8° (Amirkhanyan *et al.* 1989). The survey was carried out at a frequency of 3900 MHz on the SOUTH + FLAT antenna system of the RATAN-600 radio telescope with a $1.2' \times 50'$ beam. The positions of the radio sources were improved by Amirkhanyan (1990), because the accuracy of the declinations (2′–10′) was too low to identify them with optical objects. We performed additional observations on the western sector of RATAN-600 at the survey frequency, which allowed us to achieve close accuracies in both right ascension (10″) and declination (15″). The sample included radio sources with 3900-MHz fluxes of no higher than 100 mJy.

The second sample is an unpublished part of the Zelenchuk survey at the RATAN-600 zenith. The observations were performed in October–November 1990 on the same antenna system with the third feed using the receiving equipment of the Sternberg Astronomical Institute (SAI). Two 3900- and 7500-MHz radiometers, produced at the SAI on the

*E-mail: amir@sao.ru

basis of the SATURN OBIKHOD and OBET receiving systems, worked simultaneously in the beam-switching mode. The observations were performed at five declinations spaced 6′ apart in the ranges of declinations 43°38′–44°02′ (epoch 1950) and right ascensions $0{-}24^{\rm h}$. Each section was viewed 8 to 10 times. In the range of hour angles $10{-}16^{\rm h}$, the number of observations was reduced to 4–6, because the antenna was repointed toward the Sun. The observations were reduced using the software package described by Amirkhanyan (1990). The mean sensitivity of the survey was 7.5 and 12.5 mJy at 3900 and 7500 MHz, respectively. The detection threshold was set at a 4.5σ level (σ is the current sensitivity of the channel). At the point of detection of a radio source at 3900 MHz, the threshold at 7500 MHz decreased to 3σ. The sample included objects detected at the two frequencies.

Although the beam at 7500 MHz is almost a factor of 2 narrower ($0.6' \times 26'$) than that at 3900 MHz, the accuracy of the declinations remains unsatisfactory for optical identifications. Therefore, we identified radio sources from the zenith survey with NVSS objects (Condon *et al.* 1998) and used the declinations of the latter for the identification with "optical" objects.

In addition, we obtained an optical spectrum of the object Z0524+03 that was first detected in the Zelenchuk survey (Amirkhanyan *et al.* 1981). This object varies rapidly in both the radio (Gorshkov *et al.* 2000) and optical ranges. Its optical spectrum turned out to be a purely continuum (Chavushyan *et al.* 2001), and it was classified by the authors as a BL Lac object. Our photometric observations of the object from January 1998 through January 2001 showed that its $R_{\rm c}$ magnitude varied between 17.85 and 19.45. Since the brightness of the object at the epoch of our spectroscopic observations was far from its maximum ($m_R = 18.9$), we hoped to find lines in its spectrum.

A preliminary optical identification of radio sources was performed using the "red" maps of the Palomar Sky Survey (DSS). From the optical objects within the error box, we chose the object closest to the position of the radio source for our spectroscopic observations. In the case of a failure (stellar spectrum), we observed the next closest object.

SPECTROSCOPIC OBSERVATIONS AND DATA REDUCTION

The spectra were taken with the 6-m (BTA) and 1-m (Zeiss-1000) SAO telescopes between October 2000 and June 2002 during the operation testing of the SCORPIO spectrograph. SCORPIO is a multipurpose reducer of the focal ratio of a telescope that allows objects to be observed sequentially in several different modes (direct imaging and long-slit, slitless, multiobject, and Fabry–Perot spectroscopy). A detailed description of the instrument is in preparation and is also accessible on the Internet at http://www.sao.ru/hq/moisav/. The SCORPIO optical system reduces the equivalent focal length of a telescope, so the final focal ratio was F/2.9 and F/9 for the observations with the 6-m and 1-m telescopes, respectively. The image scale with the TK1024 (1024×1024 pixels) CCD detector was 0.28 and 0.52″ per pixel, respectively. During the observations of radio sources, only a 1024×201-pixel part of the detector was read off. In the spectroscopy mode, we used a 300 lines mm^{-1} direct-vision prism that provided the spectral range 3500–9500 Å and a spectral resolution of about 15–20 Å at a reciprocal linear dispersion of about 5 Å per pixel. The slit width on different nights was 1″–1.5″ and 2″ for the BTA and Zeiss-1000 observations, respectively. A log of observations is given in Table 1. The sequence of observations consisted of the following steps. In direct-imaging mode in the $R_{\rm c}$ band, we identified the object and then pointed the spectrograph slit to it. Subsequently, SCORPIO was switched to spectroscopy mode, and accumulations were made. The interference of transmitted light ("moire") is observed for the CCD detector used at wavelengths longer than 7500 Å. Since intense night-sky lines are observed in this range, we used the following technique to subtract them more reliably: We took two identical exposures between which the object was displaced along the slit by 10″–15″. As a result, we obtained two spectra of the object shifted by 40–50 pixels across the detector field. Subsequently, we subtracted the "clean" spectrum of the sky taken from the same area of the CCD array, but on the shifted frame, from the spectrum of the object. The wavelength scale was calibrated using the spectrum of a He–Ne–Ar lamp. To reduce the spectra to an absolute energy scale, we observed a spectrophotometric standard star in slitless mode on each night.

The data obtained were reduced using the software package written by one of us (V.L. Afanas'ev) in the IDL environment.

The data reduction procedure included the following steps: bias subtraction, allowance for local irregularities and slit wedging (flat fielding), the subtraction of night-sky lines and moire interference based on the idea of the object's image displacements along the slit described above. After the conversion of the spectra to a wavelength scale, we extracted the spectrum of the object under study. Subsequently, we converted the spectrum to a absolute flux scale (erg s^{-1} cm^{-2} Å^{-1})

Table 1. Log of observations

Object name	Date of observations	Exposure time, s	Telescope	Seeing	Zenith distance
Z0108+43	Oct. 18, 2001	1000	Zeiss-1000	$2''.1$	45°
Z0134+43	Oct. 26, 2001	3600	Zeiss-1000	2.3	11
Z0137+43	Oct. 27, 2001	5400	Zeiss-1000	1.5	4
Z0204+06	Sep. 24, 2000	600	BTA	2.7	49
Z0206+07	Sep. 29, 2000	600	BTA	3.0	46
Z0216+43	Oct. 17, 2001	1200	BTA	3.7	43
Z0220+07	Sep. 29, 2000	600	BTA	1.9	51
Z0524+03	Oct. 28, 2001	3600	Zeiss-1000	1.7	40
Z0632+43	Oct. 28, 2001	3600	Zeiss-1000	1.2	26
Z0757+44	Oct. 18, 2001	600	BTA	1.8	13
Z1224+43	June 7, 2002	600	BTA	3.9	56
Z1426+07	Apr. 5, 2002	1200	BTA	2.7	41
Z1614+06	June 9, 2002	360	BTA	4.5	52
Z1714+43	June 7, 2002	600	BTA	3.9	16
Z2112+07	Nov. 4, 2000	360	BTA	1.6	39
Z2122+07	Nov. 4, 2000	600	BTA	1.3	39
Z2137+07	Sep. 24, 2000	360	BTA	2.0	38
Z2210+06	Sep. 24, 2000	600	BTA	1.7	37
Z2211+06	Sep. 24, 2000	600	BTA	1.6	38
Z2243+43	Oct. 18, 2001	600	BTA	3.3	55
Z2248+06	Sep. 24, 2000	600	BTA	2.5	37
Z2329+07	Sep. 25, 2000	600	BTA	1.4	37

using the spectral sensitivity curve constructed from the spectrum of a standard star and the mean atmospheric extinction curve for the SAO.

RESULTS

Our spectra are shown in the figure. Most of the spectra exhibit the absorption lines of atmospheric molecular oxygen at wavelengths of 6900 and 7600 Å.

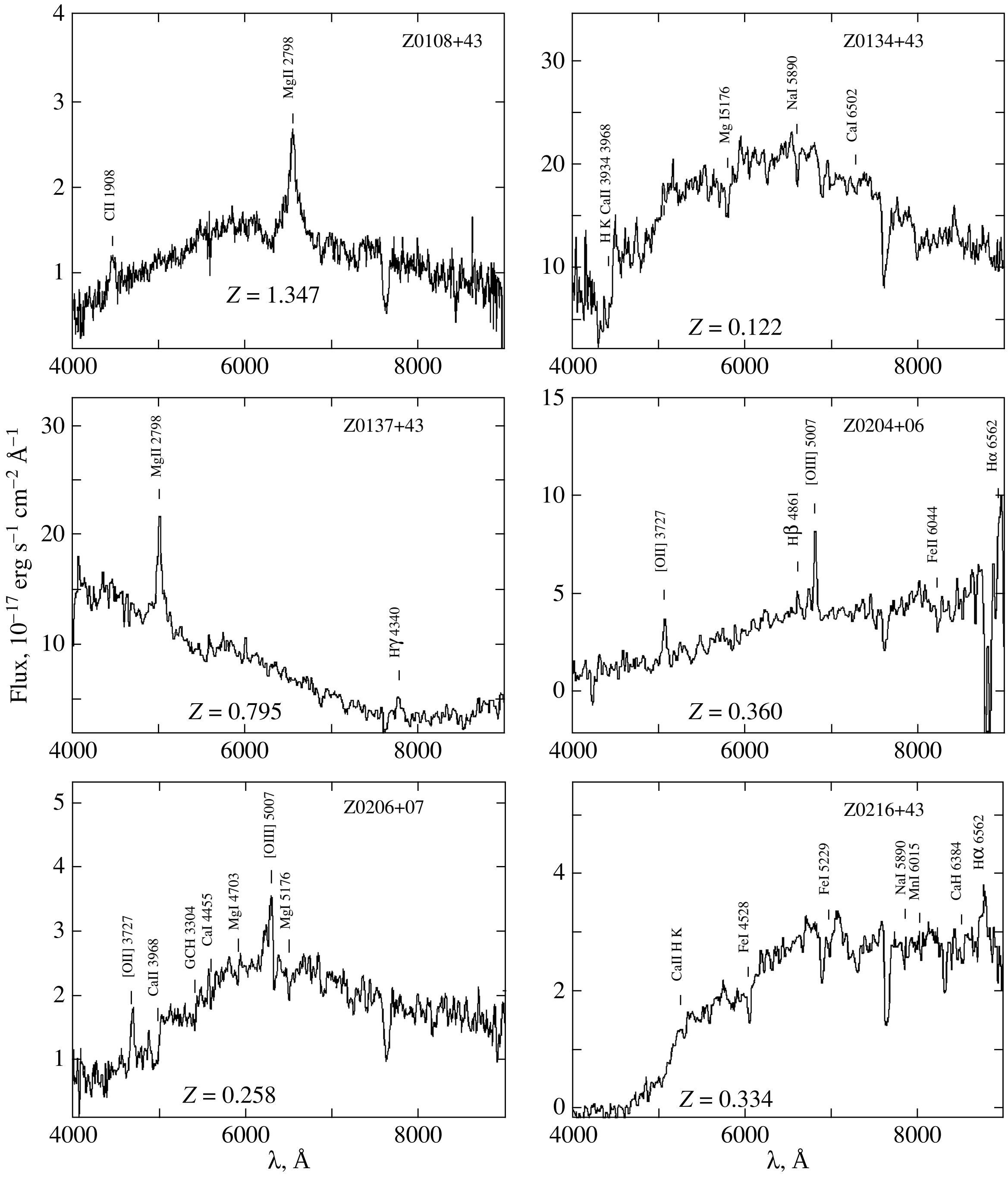

Fig. 1. Optical spectra of 22 radio sources.

The data reduction results are summarized in Table 2. Its columns give the following: (1) the object name in the Zelenchuk survey, (2) the object name in the survey in which it was first detected, (3) the optical coordinates of the object at the epoch 2000, (4) the lines identified in the object spectrum, (5) the redshift (for the object Z1714+43, we also give the value of z (in parentheses) taken from Veron-Cetty and Veron (2001)) and classification (EG—an elliptical galaxy, QSO—a quasar, and Sy—a Seyfert galaxy), (6) the estimated magnitude of the object obtained by folding the spectrum with the R_c band transmission curve corrected for the slit width, and (7) the spectral index ($S \propto \nu^{\alpha}$) and radio flux variability flag (var).

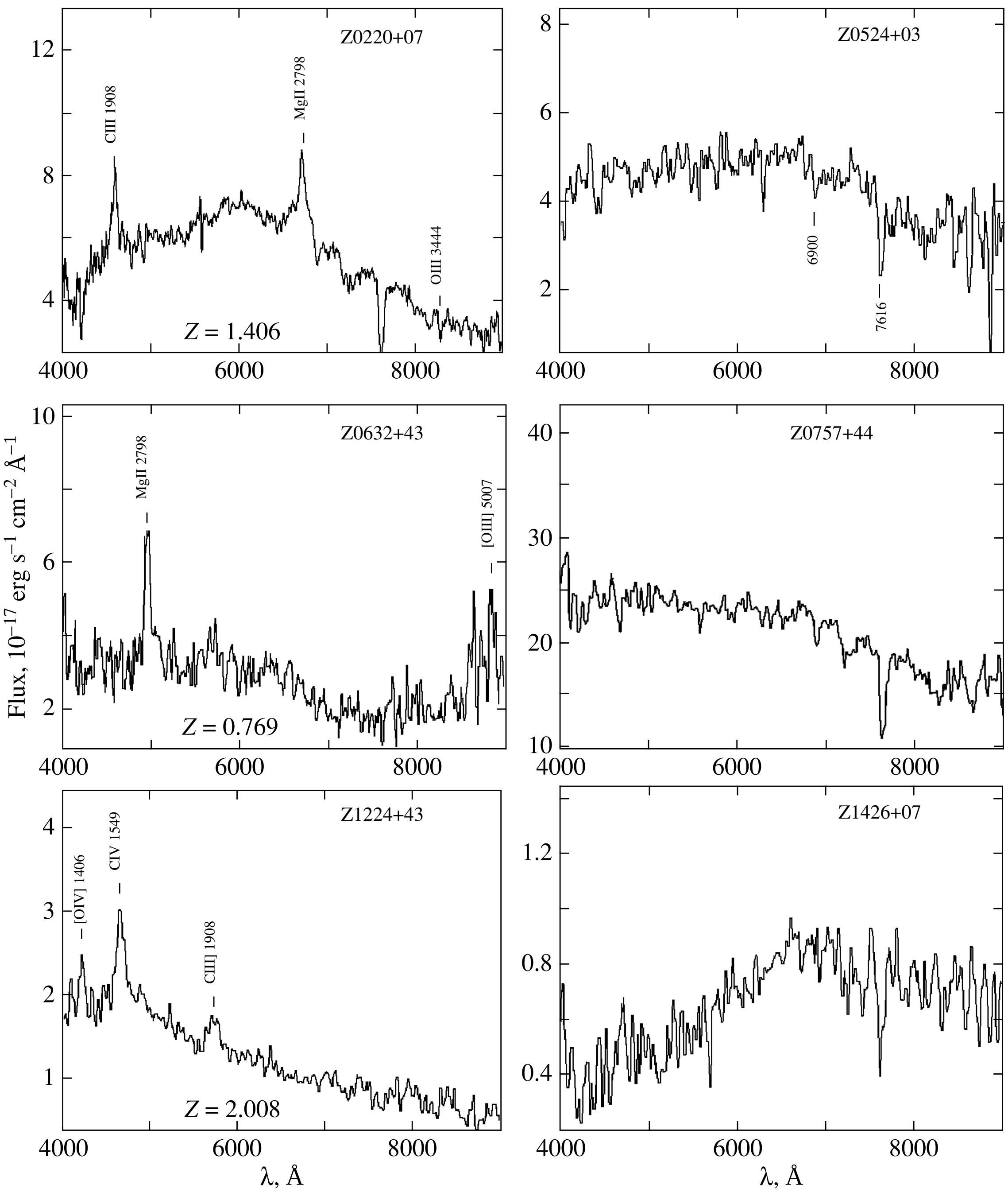

Fig. 1. (Contd.)

The information required for constructing the radio spectra and estimating the radio variability was taken from the CATS database at http://cats.sao.ru (Trushkin *et al.* 1996). The information about the structure of the radio sources was taken from the NVSS (Condon *et al.* 1998) and FIRST (Becker *et al.* 1995) surveys.

Below, we give comments to Table 2:

Z0108+43. A compact object, a quasar; the radio spectrum is normal.

Z0134+43. The direct image shows a starlike core surrounded by a faint halo. The optical spectrum implies that this is an absorption-line elliptical galaxy. The radio spectrum is normal up to 3 GHz. At higher frequencies, the spectrum is abruptly inverted ($\alpha =$

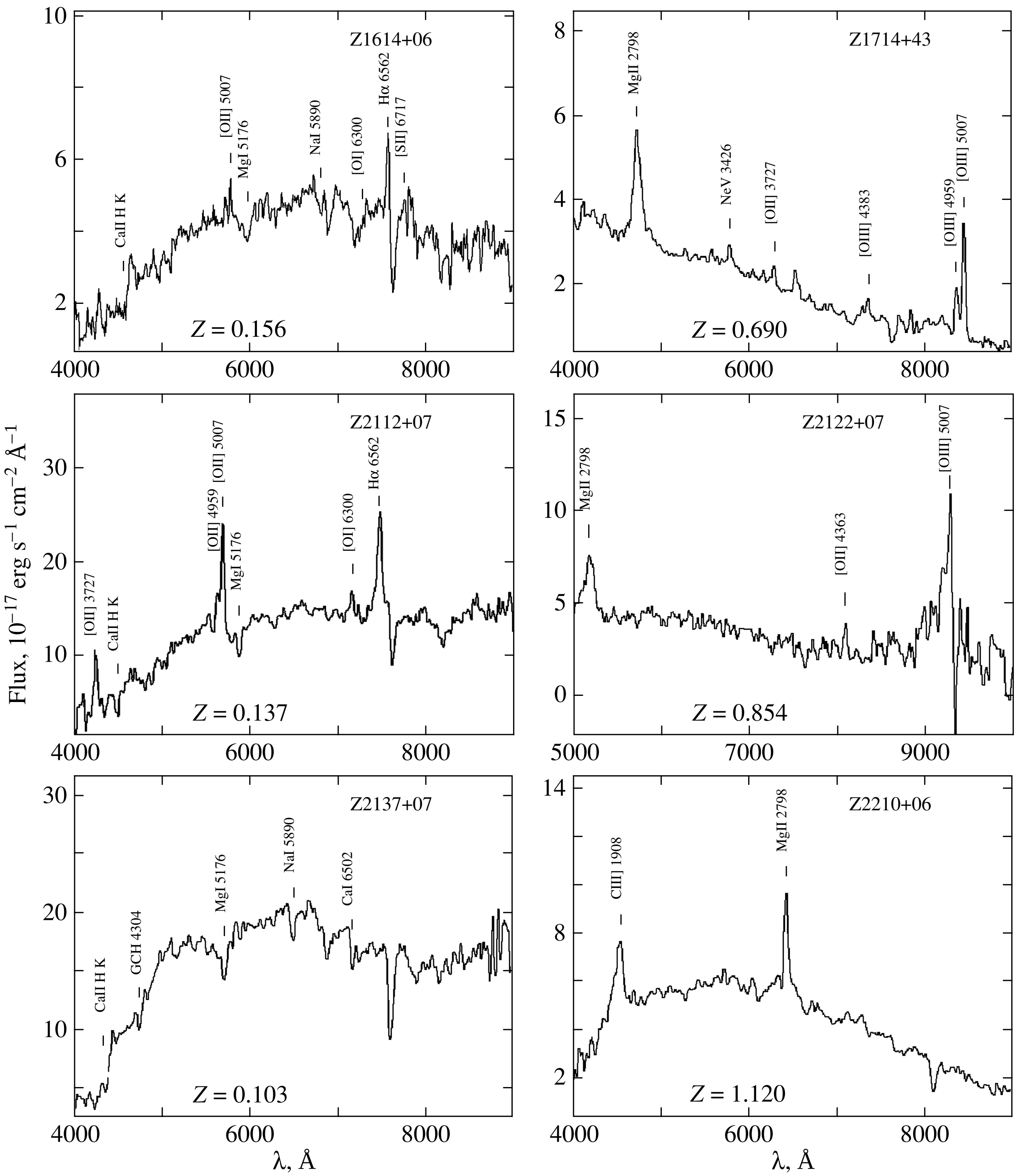

Fig. 1. (Contd.)

+0.17). The information on the radio variability is insufficient.

Z0137+43. A compact object, a quasar; the radio spectrum is flat from 100 MHz and higher. The large spread in fluxes is explained by its variability.

Z0204+06. A compact object, a quasar; the radio spectrum is normal.

Z0206+07. The core is embedded in a halo 7″ in diameter. This may be an emission-line elliptical galaxy. The slope of the radio spectrum in the frequency range 100 MHz–10 GHz is close to −0.8.

Z0216+43. A compact object; its spectrum is dominated by absorption lines. The identification of the lines for $z = 0.334$ seems to us most plausible. The radio spectrum is normal up to 1000 MHz. At

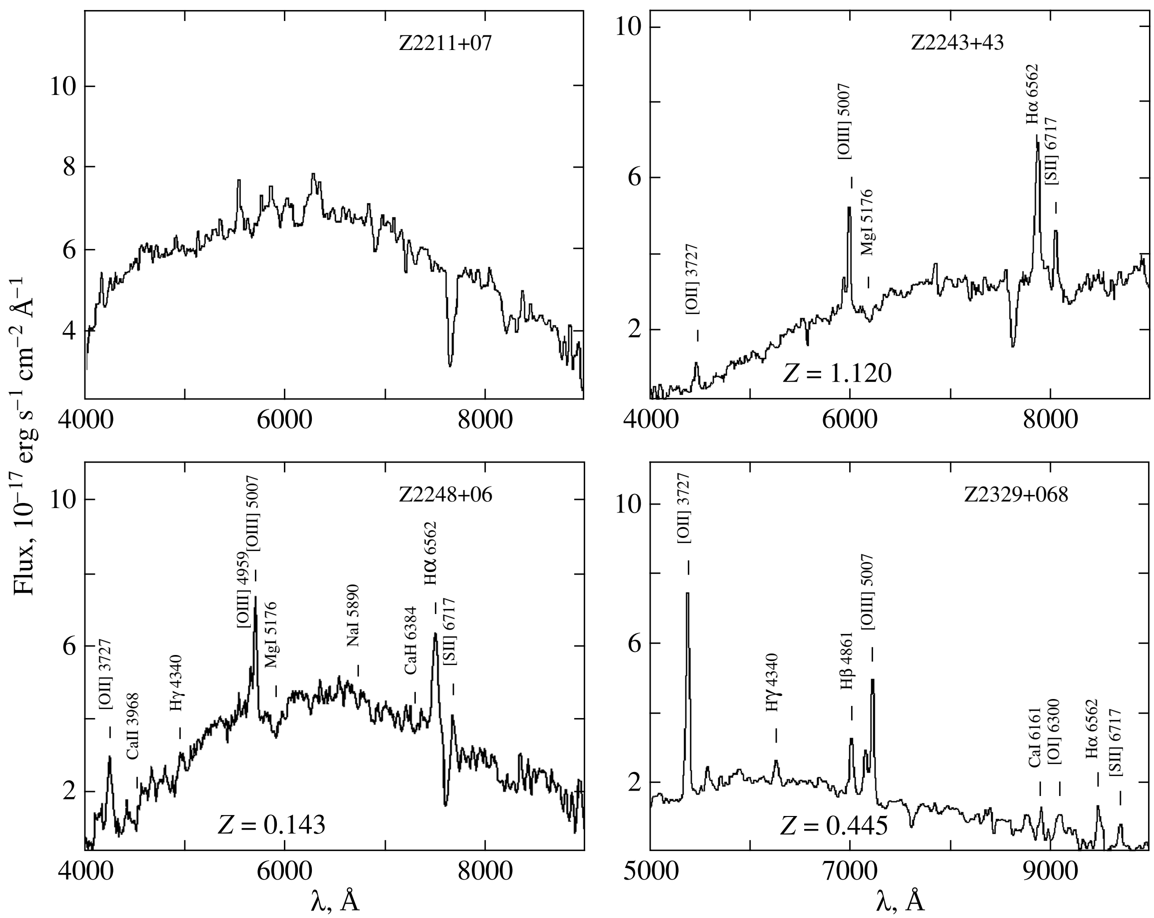

Fig. 1. (Contd.)

higher frequencies, the spectrum is inverted. The large spread in fluxes in this range is attributable to the variability of the object.

Z0220+07. A quasar. The radio spectrum is normal and stable. A classical double radio source with a maximum angular size of 10″.

Z0524+03. As in previous works, no lines could be detected in the object spectrum.

Z0757+44. In the optical range, this is a compact object with a continuum spectrum. In the frequency range 151–8400 MHz, it exhibits a flux variability and the corresponding variations in the spectral index between −0.2 and +0.3. The optical brightness of the object is probably also variable. It corresponds to the BL Lac class.

Z1224+43. A quasar. The radio spectrum is normal up to 1400 MHz. At higher frequencies, the spectrum flattens and may exhibit variability.

Z1426+07. In the optical range, it is a compact object. We failed to identify its spectrum. The extent of the radio structure (∼6″) and the stable normal radio spectrum do not allow us to classify this source as a BL Lac object.

Z1614+06. In the optical range, it is an extended object, Probably, an emission-line elliptical galaxy. The radio spectrum is normal, the structure is elongated and symmetrical about the central component ∼60″.

Z1714+43. A starlike object, a quasar. The radio spectrum is normal.

Z2112+07. A compact core is surrounded by a faint envelope. The spectrum is typical of an emission-line elliptical galaxy.

Z2137+07. In the optical range, it is a very extended object. The spectrum is typical of an absorption-line elliptical galaxy.

Z2211+06. A starlike object. The spectrum exhibits an intense continuum and weak lines that we could not identify. In the radio range, it exhibits large variability and an inverted spectrum. These features allow it to be classified as a BL Lac object.

Table 2. Optical and radio parameters of the objects studied

Object name	First survey	Coordinates 2000	Lines	Redshift	m_R	Spectral index
1	2	3	4	5	6	7
Z0108+43	B3 0108+433	$\alpha = 01\ 11\ 37.67$ $\delta = 43\ 35\ 31.7$	C III 1908, Mg II 2729	1.347 QSO	20.6	−0.6
Z0134+43	B3 0134+435	$\alpha = 01\ 37\ 11.97$ $\delta = 43\ 48\ 55.9$	Ca II 3968, Mg I 5176, Na I 5890, Ca I 6502	0.122 EG	17.6	−0.6
Z0137+43	Z0137+43	$\alpha = 01\ 40\ 54.74$ $\delta = 43\ 42\ 45.2$	Mg II 2798, O III 3341 O III 4363, Hγ 4340	0.795 QSO	19.0	+0.03 var.
Z0204+06	4C+06.09	$\alpha = 02\ 07\ 06.79$ $\delta = 06\ 59\ 01.6$	O II 3727, Ca II 3968, Hβ 4861, O III 4959, O III 5007, Fe II 6044	0.36 QSO	19.5	−0.67
Z0206+07	4C+07.07	$\alpha = 02\ 09\ 04.77$ $\delta = 07\ 50\ 04.7$	O II 3727, CaII 3968, O III 4959, O III 5007	0.258 QSO	20.1	−0.78
Z0216+43	Z0216+43	$\alpha = 02\ 20\ 07.12$ $\delta = 44\ 01\ 44.5$	Hα 6562 Mg I 5176	0.334 EG	19.9	+0.01 var.
Z0220+07	4C+06.10	$\alpha = 02\ 23\ 21.31$ $\delta = 06\ 39\ 31.6$	O III 1908, Mg 2798, O III 3444	1.406 QSO	19.0	−0.84
Z0524+03	Z0524+03	$\alpha = 05\ 27\ 32.70$ $\delta = 03\ 31\ 32.8$	–	– BL	19.2	∼0 var.
Z0632+43	TXS B0632+43	$\alpha = 06\ 35\ 56.30$ $\delta = 43\ 33\ 12.9$	Mg 2798, O III 4363	0.769 QSO	20	−0.6
Z0757+44	Z0757+44	$\alpha = 08\ 01\ 08.33$ $\delta = 44\ 01\ 09.3$	–	– BL	20.2	∼0 var.
Z1224+43	B3 1224+439	$\alpha = 12\ 26\ 57.96$ $\delta = 43\ 40\ 57.0$	O IV 1406, CIV 1550, C III 1909	2.008 QSO	20.3	∼0 var.
Z1426+07	Z1426+07	$\alpha = 14\ 28\ 29.61$ $\delta = 07\ 08\ 36.9$	–	–	20.9	−0.58
Z1614+06	4C+06.55	$\alpha = 16\ 17\ 13.4$ $\delta = 06\ 37\ 29.3$	O III 5007, Hα 6562	0.156 EG	18.3	−0.8
Z1714+43	MSL OT+424	$\alpha = 17\ 15\ 55.9$ $\delta = 43\ 40\ 16.4$	Mg 2798, O II 3727, O III 5007	0.69 (0.685) QSO	19.6	−0.82
Z2112+07	OX+020.5	$\alpha = 21\ 14\ 34.6$ $\delta = 07\ 53\ 02.0$	O II 3727, O III 5007, O I 6300, Hα 6562	0.137 EG	18.1	−0.6
Z2122+07	OX+037	$\alpha = 21\ 24\ 56.8$ $\delta = 07\ 57\ 20.7$	Mg 2798, O III 4363, O III 5007	0.854 QSO	19.6	−0.8
Z2137+07	Z2137+07	$\alpha = 21\ 40\ 03.8$ $\delta = 07\ 24\ 58.6$	GCH4304, Mg I 5176, Na I 5890, Ca I 6502	0.103 EG	17.8	−0.69
Z2210+06	Z2210+06	$\alpha = 22\ 12\ 50.8$ $\delta = 06\ 46\ 08.9$	C III 1908, Mg II 2798	1.12 QSO	19.4	−0.2 var.
Z2211+06	OY+019	$\alpha = 22\ 14\ 8.9$ $\delta = 07\ 11\ 42.4$	–	– BL	19.3	+0.1 var.
Z2243+43	Z2243+43	$\alpha = 22\ 45\ 50.03$ $\delta = 44\ 01\ 57.3$	O II 3727, O III 5007, Mg I 5176 S II 6717, Hα 6562	0.198 EG	19.2	−0.57 var.
Z2248+06	4C+06.75	$\alpha = 22\ 50\ 46.8$ $\delta = 07\ 02\ 05.3$	O II 3727, O III 5007, Hα 6562 S II 6717	0.143 EG	19.0	−0.6
Z2329+06	PKS 2329+06	$\alpha = 23\ 31\ 55.6$ $\delta = 07\ 05\ 41.5$	OII 3727, Hγ 4340 Hβ 4861, O III 5007, Hα 6562 S II 6717	0.445 Sy	20.2	−0.36 var.

Z2243+43. A compact core surrounded by a faint envelope. The spectrum is typical of an emission-line elliptical galaxy. The radio spectrum is normal up to 4 GHz. At higher frequencies, the spectrum is inverted. Flux variability may be observed.

Z2329+068. The optical spectrum exhibits broad emission lines of hydrogen and forbidden emission lines of oxygen. The radio spectrum is flat, and the flux is variable. We classify the object as a Seyfert galaxy.

CONCLUSIONS

We performed optical spectroscopic observations of 22 radio sources from the Zelenchuk survey with the 1-m and 6-m SAO telescopes. For 18 of these sources, we determined the redshifts. We classified the objects Z0108+43, Z0137+43, Z0204+06, Z0206+07, Z0220+07, Z0632+43, Z1224+43, Z1714+43, Z2122+07, and Z2210+06 as quasars, Z0134+43, Z0216+43, Z1614+06, Z2112+07, Z2137+07, Z2243+43, and Z2248+06 as elliptical galaxies, and Z2329+06 as a Seyfert galaxy. We classified Z0757+44 and Z2211+06 as BL Lac objects. Additional observations are probably required to reliably identify Z1426+07.

REFERENCES

1. V. L. Afanas'ev, A. V. Moiseev, É. B. Gazhur, *et al., SAO Report 1999–2000* (2001), p. 31.
2. V. R. Amirkhanyan, Astrofiz. Issled. **29**, 129 (1990).
3. V. R. Amirkhanyan, A. G. Gorshkov, A. A. Kapustkin, *et al., A Catalog of the Zelenchuk Survey Radio Sources with Declinations 0–14* (MGU, Moscow, 1989), p. 200.
4. V. R. Amirkhanyan, V. V. Vlasyuk, and O. I. Spiridonova, Astron. Zh. **70**, 923 (1993) [Astron. Rep. **37**, 466 (1993)].
5. R. H. Becker, R. L. White, and D. J. Helfand, Astrophys. J. **450**, 559 (1995).
6. V. Chavushyan, R. Mukhika, A. G. Gorshkov, *et al.,* Pis'ma Astron. Zh. **26**, 403 (2000) [Astron. Lett. **26**, 339 (2000)].
7. V. Chavushyan, R. Mukhika, A. G. Gorshkov, *et al.,* Astron. Zh. **78**, 99 (2001).
8. J. J. Condon, W. D. Cotton, E. W. Greisen, *et al.*, Astron. J. **115**, 1693 (1998).
9. A. G. Gorshkov, V. K. Konnikova, and M. G. Mingaliev, Astron. Zh. **77**, 188 (2000).
10. S. A. Trushkin, H. Andernach, A. Micol, *et al.*, in *Proceedings of the Third International Workshop on Advances in Databases and Information Systems* (Eng. Phys. Inst. Publ., Moscow, 1996), Vol. 2, p. 37.
11. M. P. Veron-Cetty and P. Veron, Astron. Astrophys. **374**, 92 (2001).

Translated by G. Rudnitskii

Astronomy Letters, Vol. 30, No. 12, 2004, pp. 843–847. Translated from Pis'ma v Astronomicheskiĭ Zhurnal, Vol. 30, No. 12, 2004, pp. 924–929.

Study of the Weakly Magnetic Star HD 116656

Yu. V. Glagolevskij*, V. V. Leushin, and G. A. Chuntonov

Special Astrophysical Observatory, Russian Academy of Sciences, Nizhniĭ Arkhyz, 357147 Karachaĭ-Cherkessian Republic, Russia

Received October 26, 2003; in final form, May 31, 2004

Abstract—We studied the spectroscopic binary HD 116656 (ζ^1 UMa) that has previously been suspected to be a Si-type chemically peculiar star. The magnetic field of each individual component was measured with a high accuracy, but none were found. The upper limit for each field was estimated as 20 G. The abundances of the chemical elements studied in both components proved to be the same. The pattern of their chemical anomalies suggests that they are more likely chemically peculiar Am stars than magnetic CP stars. The rotational velocities of the components slightly differ, 31.7 km s^{-1} for component A and 37.0 km s^{-1} for component B. Low rotational velocities are characteristic of both nonmagnetic metallic-line and magnetic chemically peculiar stars. © *2004 MAIK "Nauka/Interperiodica".*

Key words: *stars—variable and peculiar.*

INTRODUCTION

Until now, the interest of astrophysicists has concerned stars with strong magnetic fields, while weakly magnetized stars with fields $\leq$500 G have not been studied at all. Since a new technique using CCD detectors has increased the measurement accuracy by an order of magnitude, it is now possible to study stars with weak magnetic fields. In recent years, attempts have been repeatedly made to study such stars (see, e.g., Glagolevskij *et al.* 1989; Shorlin *et al.* 2002; Glagolevskij and Chuntonov 2002; Monin *et al.* 2002). The following main conclusions can be drawn from these results:

(1) Despite the increase in the measurement accuracy by an order of magnitude, no magnetic field has been detected around many chemically peculiar stars;

(2) Despite the absence of a field or its extreme weakness, many stars exhibit rather strong chemical anomalies and low rotational velocities.

These properties contradict the existing opinion that a fairly strong magnetic field is needed for the formation of chemical anomalies and that the low rotational velocities result from magnetic braking at early evolutionary stages. In addition, stars with weak magnetic fields are inconsistent with the well-known property that the degree of chemical anomalies is proportional to the magnetic field strength (Cramer and Maeder 1980; Glagolevskij 1994). It may be assumed that various deviations from the standard laws can arise for weak magnetic fields, when the transition from normal to magnetic stars is observed. This paper is devoted to one such star, HD 116656, in which chemical anomalies have been found by several authors.

BASIC PROPERTIES

The star HD 116656 is listed in the catalog of variable stars (Kukarkin *et al.* 1982) under the name NSV 06224. The star is a spectroscopic binary with an orbital period of $20\overset{d}{.}54$ (Pourbaix 2000).

HD 116656 (ζ^1 UMa) is absent from the list of chemically peculiar stars (Egret and Jashek 1981), but it is listed in the Bright Star Catalog (Hoffleit 1982) as an A1 VpSrSi-type object (see Table 1). Gray and Garrison (1987) classified it as an A1 V(Si) CP star, while Guiricin *et al.* (1984) classified its components as A1Vp+A1V with $v \sin i = 35$ and 35 km s^{-1}; i.e., one of the components was found to be chemically peculiar. Due to the orbital motion, the maximum difference between the radial velocities of the components is about 150 km s^{-1}.

However, a comparison of the spectrum for HD 116656 with the spectra of normal stars revealed no peculiarities (Shorlin *et al.* 2002). Edwards (1976) classified its components, also without any indication of a peculiarity: Sp(1) = Sp(2) = A2 V, $\Delta m = 0.0$.

The λ 5200 Å depression characteristic of CP stars is $\Delta a = 0.018$ for the combined spectrum of HD 116656 (Lebedev 1986). This value corresponds to magnetic stars with effective fields of $B_e \approx 300$ G, although the multicolor photometry parameter Z is

*E-mail: glagol@sao.ru

Table 1. Spectral classification of HD 116656 from different sources

Spectral classification	Source
Normal star	Egret and Jashek (1981)
Normal star	Shorlin *et al.* (2002)
A1VpSrSi	Bright Star Catalog
A1 VSi	Gray and Garrison (1987)
A1 Vp+A1 V	Guiricin *et al.* (1984)
A2 V+A2 V	Edwards (1976)

identical to that for normal stars (Glagolevskij and Chuntonov 2002). Given that, according to Guiricin *et al.* (1984), only one of the components is chemically peculiar, the depression should be doubled; it will then correspond to a field of ∼500–600 G.

The Balmer jump $D = 0.51$ that we estimated using data from the catalog by Kharitonov *et al.* (1978) corresponds to normal main-sequence stars. This jump and the continuum energy distribution are the same as those for α Lyr with $T_{\rm e} = 9553$ K (Ciardi *et al.* 2001). According to Geneva photometry (Palous and Hauck 1986), the temperature of the stars is $T_{\rm e} = 9200$ K, while according to the Strömgren photometry, their absolute magnitude is $M_{\rm v} = 1.07$ (the bolometric absolute magnitude is $M_{\rm b} = 1.0$), which corresponds to the luminosity class V ($\log g = 4.05$). Hummel *et al.* (1998) gave the following revised parameters: $M_{\rm b} = 0.91$ and $T_{\rm e} = 9000 \pm 200$ K, from which it follows that $\log g = 3.9$ (luminosity class V–IV).

The above review shows that both components are in the middle of the main-sequence strip. There is no agreement as to whether the binary is a chemically peculiar star. If one component is peculiar, while the other is normal, then the fields must be measured separately for both components. This is our prime objective.

THE MAGNETIC FIELD

Before our measurements, the mean effective field for HD 116656 was estimated most accurately by Shorlin *et al.* (2002): $B_{\rm e} = -9 \pm 16$ G; the field was measured with a slightly lower accuracy by Monin *et al.* (2002) (Table 2). These data show that the upper limit for the field does not exceed several tens of gauss. A single measurement cannot be reliable enough, because the field in CP stars is variable, thereby requiring additional measurements. In addition, measurements for each individual components are of considerable interest. With this in mind, we measured the field at the phase at which the separation between the components was close to its maximum value of $\Delta\lambda \approx 1$ Å. This phase occurred at JD = 2452657.58. The observational data were obtained with a CCD array using the Main Stellar Spectrograph of the 6-m telescope. The spectral range covered was 4400–4640 Å, and the dispersion was 0.115 Å per pixel. The CCD array was 2K × 2K. The lines of the components are clearly resolved to measure the field in each of them individually. We selected 15 unblended lines for our measurements.

We used the following technique to increase the measurement accuracy. The analyzer consisted of an achromatic phase quarter-wave plate in front of the slit and a polarizer (Savart plate) behind the slit. As usual, the polarizer yielded two Zeeman spectra, with right-hand polarization (rhp) and left-hand polarization (lhp). The phase plate was periodically turned through 90°, and the CCD spectrum was simultaneously moved by a given number of rows, back and forth across the dispersion. As a result of this turn, the right- and left-hand polarized spectra switched places. In this way, the first and the second pairs of Zeeman spectra were taken. As a result, we obtained four spectra: (1rhp–1lhp) and (2lhp–2rhp). The Zeeman shifts were determined by measuring the (1rhp)–(2lhp) and (1lhp)–(2rhp) shifts. Since the spectra were taken on the same CCD areas, the influence of nonuniform pixel sensitivity was reduced, and the unavoidable tilt of the spectrograph slit was compensated for. If the first and the second pairs of spectra were added from a large number of exposures taken in turn, the effects of instability in the image position on the slit are reduced.

A small portion of the processed spectrum is shown in Fig. 1. Figures 1a and 1b show, respectively, the spectra taken at the phases at which the lines of both components merged together and were separated. On average, the number of recorded electrons per pixel was 2.8×10^7, ensuring a high signal-to-noise ratio. The field strengths estimated from short-wavelength and long-wavelength lines are given in the last two rows of Table 2. Clearly, the magnetic field strength for each component of HD 116656 does not exceed 20–30 G. Thus, we have confirmed the absence of a detectable field in HD 116656. The rms field estimated from all of the data in Table 2 is $\langle B_e \rangle = 0 \pm 9$ G.

Table 2. Measurements and estimates of the magnetic field for the star HD 116656

JD	B_e, G	$\pm\sigma$, G	Source
Zeeman spectral measurements			
–	−9	16	Shorlin *et al.* (2002)
2 450 177.38	−91	82	Monin *et al.* (2002)
.44	26	61	Monin *et al.* (2002)
2 452 657.58	28	16	Our measurements of component 1
»	−13	13	Our measurements of component 2
Estimates from parameters (both stars together)			
–	300	–	Our estimate from 5200 Å depression
–	0	–	Our estimate from parameter Z
–	0	–	Our estimate from Balmer jump

CHEMICAL ANOMALIES

The star HD 116656 corresponds in temperature to CP SiSrCrEu stars. There are no sufficiently strong silicon, strontium, and europium lines in the wavelength range used to measure the magnetic field, and their abundances cannot be estimated for peculiarity. The strong lines belong to Fe, Cr, and Ti.

The spectra were taken with a high signal-to-noise ratio (>1000). They clearly show (Fig. 1b) that the short-wavelength components of the spectral lines are shallower but wider than the long-wavelength components. Using the method of synthetic spectra, we obtained the following estimates of the rotational velocities for the components from iron lines. The slowly and rapidly rotating components have $v \sin i = 31.7$ and 37.0 km s^{-1}, respectively. These differences were not noted in the references cited above. In these calculations, the iron abundance was taken to be $\log N(\mathrm{Fe})$ from Table 3.

Here, we estimated the chemical composition for both components from a spectrum with resolvable lines. The model atmosphere was computed with the parameters $T_e = 9200$ K and $\log g = 4.00$. The computations were performed using the SAMI code (Wright 1975) modified by Leushin and Topil'skaya (1985). The chemical composition of the models is solar. The line parameters for the chemical elements in Table 3 were taken from the VALD list (Ryabchikova *et al.* 1999).

The microturbulent velocity determined from the dependences of $\log N$ on W_λ was found to be, on average, 2.5 km s^{-1}. The derived atmospheric ele-

Table 3. Chemical composition of HD 116656

Element	$\log(N/N_{\mathrm{tot}})$	$\Delta \log(N/N_{\mathrm{tot}})$
Mg	−4.30	+0.16
Si	−4.35	+0.14
Ca	−5.90	−0.22
Sc	−10.00	−1.06 :
Ti	−6.80	+0.25
Cr	−6.20	+0.17
Fe	−4.35	+0.19
Ni	−5.50	+0.29
Zr	−8.80	+0.64
Ba	−8.85	+1.06

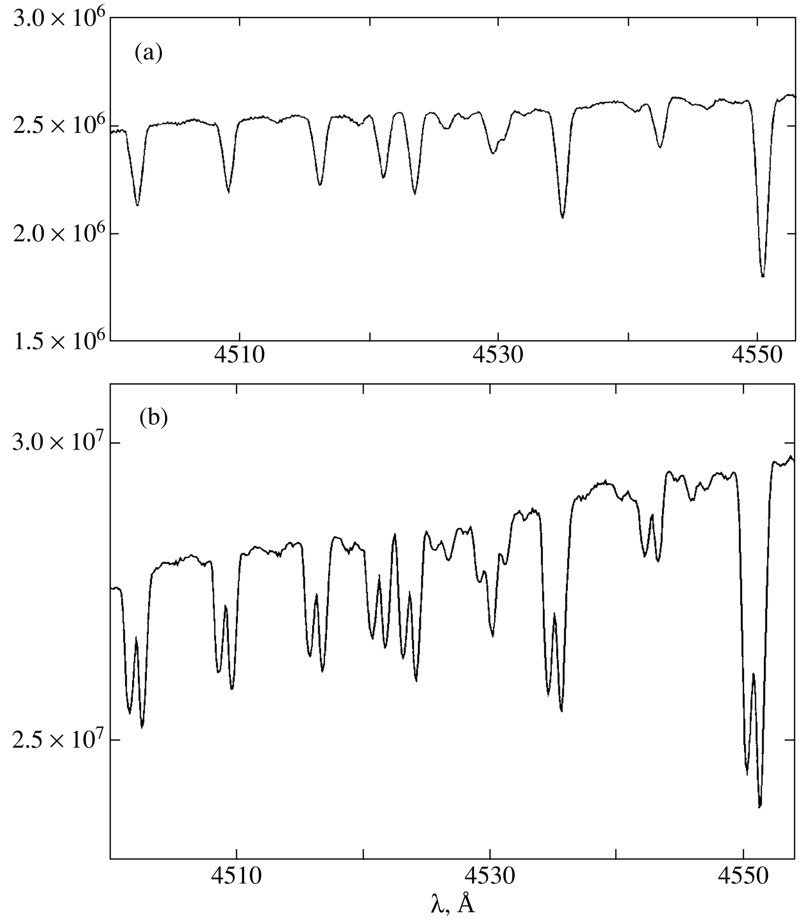

Fig. 1. (a) Part of the spectrum for HD 116656 at the phase at which the radial velocities of the components are equal; (b) the same part of the spectrum at the phase at which the difference between the radial velocities of the components is $\Delta\lambda \approx 1$ Å. The number of electrons per CCD pixel column is along the vertical axis.

mental abundances for both components are almost identical. The mean elemental abundances for both components, $\log(N/N_{\rm tot})$, are given in Table 3. Here, $N_{\rm tot}$ is the total abundance, and $\Delta\log(N/N_{\rm tot})$ is the deviation of the abundance from its solar value. The Ca and Sc abundances are lower than their solar values. Ca and Sc underabundances are characteristic of metallic-line stars. The remaining elements in the metallic-line stars that we studied are characterized by a small overabundance or underabundance of Mg and Si, an overabundance of iron-peak elements, and a large overabundance of Zr and Ba (Lyubimkov 1995). Based on their chemical peculiarities, both stars should be more likely classified as metallic-line stars rather than as Si stars. If this is the case, then the spectral classification is incorrect, and the absence of a magnetic field is normal.

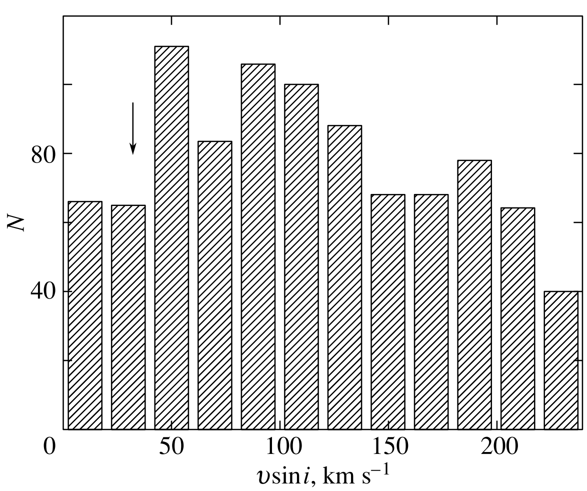

Fig. 2. Distribution (histogram) of normal, N, normal main-sequence stars in $v\sin i$. The arrow indicates the position of HD 116656.

CONCLUSIONS

(1) Thus, some of the physical properties of the spectroscopic binary HD 116656 more likely correspond to chemically peculiar, main-sequence Am stars than to Si stars, and its field, if it exists, does not exceed 20–30 G.

(2) Using HD 116656 as an example, we have confirmed the absence of magnetic fields in metallic-line stars with a high accuracy.

(3) As was noted above, our main objective was to study chemically peculiar stars with weak magnetic fields. One of the problems is that enhanced abundances of chemical elements and a low rotational velocity are observed for an absent or very weak magnetic field. It is generally believed that a low rotational velocity is explained by the loss of angular momentum involving a magnetic field. However, this hypothesis is not confirmed for HD 116656 and other CP and Am stars without a magnetic field. Figure 2 shows the distribution of normal main-sequence stars (Sp = A0–A5) in rotational velocity constructed from data of the catalog by Uesugi and Fucuda (1982). We clearly see that the bulk of the stars have rotational velocities within the range 50–200 km s^{-1}. The position of HD 116656 is indicated by the arrow, from which we see that the rotational velocities of both components are much lower than the mean value. There is a different opinion that the chemically peculiar stars are slow rotators from the outset (Abt and Morrell 1995; Glagilevskij and Chuntonov 2002; Glagolevskij and Gerth 2003). From this point of view, the slow rotation of the two components of HD 116656 is normal.

Both components of HD 116656 are far from the zero-age sequence and do not depart from the main sequence when chemical anomalies might be expected to appear or to disappear; instead, these stars are in the middle of the main-sequence strip. The example of HD 116656 also shows that a magnetic field is not a crucial factor in the development of chemical diffusion. It follows from our results that it is necessary to analyze the chemical composition of the star HD 116656 and other similar objects in more detail and to measure their magnetic fields more accurately.

ACKNOWLEDGMENTS

We wish to thank T.A. Ryabchikova for her helpful discussions and valuable advice. This study was supported by the federal Astronomy program.

REFERENCES

1. H. A. Abt and N. L. Morrell, Astrophys. J., Suppl. Ser. **99**, 135 (1995).
2. D. R. Ciardi, G. T. van Belle, R. L. Akeson, *et al.*, Astrophys. J. **559**, 1147 (2001).
3. N. Cramer and A. Maeder, Astron. Astrophys., Suppl. Ser. **41**, 111 (1980).
4. T. W. Edwards, Astron. J. **81**, 245 (1976).
5. D. Egret and M. Jashek, *Upper Main Sequence Chemically Peculiar Stars* (Inst. D'Astrophysique Univ. de Liege, Liege, 1981).
6. Yu. V. Glagolevskij, Astron. Zh. **71**, 858 (1994) [Astron. Rep. **38**, 764 (1994)].
7. Yu. V. Glagolevskij and G. A. Chuntonov, Astrofizika **45**, 408 (2002).
8. Yu. V. Glagolevskij and E. Gerth, Bull. Spec. Astrophys. Obs. **55**, 38 (2003).
9. Yu. V. Glagolevskij, I. I. Romanyuk, I. D. Naidenov, and V. G. Shtol', Izv. Spets. Astrofiz. Obs. **27**, 34 (1989).
10. R. O. Gray and R. E. Garrison, Astrophys. J., Suppl. Ser. **65**, 581 (1987).
11. G. Guiricin, F. Mardirossion, and M. Mezzetti, Astron. Astrophys. **135**, 394 (1984).
12. T. A. Hummel, D. Mozurkewich, J. T. Armstrong, *et al.*, Astron. J. **116**, 2536 (1998).
13. A. V. Kharitonov, V. M. Tereshchenko, and L. N. Knyazeva, *A Summary Photometric Star Catalogue* (Nauka KazSSR, Alma-Ata, 1978) [in Russian].
14. B. V. Kukarkin, P. N. Kholopov, and N. M. Artyukhina, *A New Catalog of Suspected Variable Stars* (Nauka, Moscow, 1982) [in Russian].
15. V. S. Lebedev, Izv. Spets. Astrofiz. Obs. **21**, 30 (1986).
16. V. V. Leushin and G. P. Topil'skaya, Astrofizika **22**, 121 (1985).
17. L. S. Lyubimkov, *Chemical Composition of Stars* (Astroprint, Odessa, 1995), p. 148 [in Russian].
18. D. Monin, S. Fabrika, and G. Valyavin, Astron. Astrophys. **396**, 131 (2002).
19. J. Palous and B. Hauck, Astron. Astrophys. **162**, 54 (1986).
20. D. Pourbaix, Astron. Astrophys., Suppl. Ser. **145**, 215 (2000).
21. T. L. Ryabchikova, N. E. Piskunov, H. C. Stempels, *et al.*, Phys. Scr. **83**, 162 (1999).
22. S. L. S. Shorlin, G. A. Wade, J.-F. Donati, *et al.*, Astron. Astrophys. **392**, 636 (2002).
23. A. Uesugi and I. Fucuda, *Revised Catalogue of Stellar Rotational Velocities* (Kyoto Univ. Press, Kyoto, 1982).
24. S. L. Wright, Comm. Univ. London Obs. **76**, 1 (1975).

Translated by N. Samus'

Astronomy Letters, Vol. 30, No. 12, 2004, pp. 848–853. Translated from Pis'ma v Astronomicheskiĭ Zhurnal, Vol. 30, No. 12, 2004, pp. 930–935.
Original Russian Text Copyright © 2004 by Bobylev.

Astrometric Control of the Inertiality of the Hipparcos Catalog

V. V. Bobylev*

Pulkovo Astronomical Observatory, Russian Academy of Sciences, Pulkovskoe sh. 65, St. Petersburg, 196140 Russia

Received March 1, 2004

Abstract—Based on the most complete list of the results of an individual comparison of the proper motions for stars of various programs common to the Hipparcos catalog, each of which is an independent realization of the inertial reference frame with regard to stellar proper motions, we redetermined the vector ω of residual rotation of the ICRS system relative to the extragalactic reference frame. The equatorial components of this vector were found to be the following: $\omega_x = +0.04 \pm 0.15$ mas yr^{-1}, $\omega_y = +0.18 \pm 0.12$ mas yr^{-1}, and $\omega_z = -0.35 \pm 0.09$ mas yr^{-1}. *© 2004 MAIK "Nauka/Interperiodica".*

Key words: *ICRS system, astronomical constants, astrometry.*

INTRODUCTION

A kinematic analysis performed previously (Bobylev 2004) revealed appreciable residual rotation of the stars of the Hipparcos catalog (ESA 1997) with respect to the inertial reference frame around the Galactic y axis with an angular velocity of -0.36 ± 0.09 mas yr^{-1} (milliarcseconds per year). A shortcoming of the method used is the absence of a rigorous criterion for separating the actual rotation of stars close to the Sun from the sought systematic rotation. The method of analyzing the proper-motion differences for stars of various programs common to the Hipparcos catalog, each of which is an independent realization of the inertial reference frame with regard to stellar proper motions, is free from this shortcoming. We call this method astrometric. Based on this method, Kovalevsky *et al.* (1997) found that all three components of the vector $\boldsymbol{\omega}$ of residual rotation of the Hipparcos catalog with respect to the extragalactic reference frame have no significant deviations from zero, with the error of this vector along the three axes being ± 0.25 mas yr^{-1}. The difficulties in applying this method stem from the fact that there are few VLBI observable radio stars, while photographic catalogs are not free from the magnitude dependence of the stellar proper motions (the magnitude equation). The goal of this study is to redetermine the vector $\boldsymbol{\omega}$ using the most complete list of the independent results from an individual comparison of the stellar proper motions.

*E-mail: vbobylev@gao.spb.ru

CHARACTERISTIC OF INDIVIDUAL SOLUTIONS

Based on the NPM photographic program of the Lick observatory (Klemola *et al.* 1987), two catalogs of absolute proper motions for northern-sky stars have been published: the NPM1 catalog of stars in 899 areas outside the Milky Way zone (Klemola *et al.* 1994) and the NPM2 catalog of stars in 347 areas of the Milky Way zone (Hanson *et al.* 2003). The areas of the NPM1 and NPM2 catalogs do not overlap. The results of a comparison of the proper motions for NPM1 and Hipparcos stars were described by Platais *et al.* (1998b) and designated as NPM(Yale) by Kovalevsky *et al.* (1997). An independent analysis of the proper-motion differences between the NPM1 and Hipparcos catalogs was also performed in Heidelberg; Kovalevsky *et al.* (1997) designated the results of this analysis as NPM(Heidelberg). All of the above authors agree that the component ω_z is difficult to determine using the NPM1 catalog, because there is a magnitude equation in the NPM1 proper motions that causes the NPM1−Hipparcos differences to be shifted by ≈ 6 mas yr^{-1} for the brightest ($\approx 8^m$) and faintest ($\approx 12^m$) stars. Kovalevsky *et al.* (1997) did not include the component ω_z determined from NPM1 stars in their final solution.

Zhu (2003) compared the proper motions of NPM2 and Hipparcos stars. This author found no appreciable magnitude dependence of the NPM2−Hipparcos differences.

Based on the SPM program of photographic observations of southern-sky stars (Platais *et al.* 1995), Platains *et al.* (1998a) publised the SPM2 catalog of absolute proper motions of stars in 156 southern-sky areas. The results of a comparison of the absolute proper motions of SPM stars in 63 areas with the Hipparcos catalog were described by Platais *et al.* (1998a). We designate these SPM stars as SPM1. Zhu (2001) compared the proper motions of SPM2 and Hipparcos stars.

Based on the combined photographic catalog GPM (Rybka and Yatsenko 1997a), Rybka and Yatsenko (1997b) published a list of proper motions for bright stars common to the Hipparcos catalog designated as GPM1. Kislyuk *et al.* (1997) compared the proper motions of GPM1 and Hipparcos stars. These authors concluded that there is a magnitude equation in the GPM1 catalog, and the parameters ω_x, ω_y, and ω_z determined only from faint comparison stars must be used.

Bobylev *et al.* (2004) determined the parameters ω_x, ω_y, and ω_z by comparing the Pulkovo photographic catalog PUL2 and Hipparcos and found no appreciable magnitude equation in the proper motions of PUL2 stars. Each of the GPM and PUL2 catalogs is an independent realization of the photographic plan by Deutch (1954); the centers of the areas coincide and correspond to the list of Deutch (1955).

The results of the well-known independent programs were presented by Kovalevsky *et al.* (1997). In addition, the results of the Potsdam program were presented by Hirte *et al.* (1996), and the Bonn program by Geffert *et al.* (1997) and Tucholke *et al.* (1997); the Earth Rotation Parameters (EOP) were analyzed by Vondrak *et al.* (1997); radio stars were analyzed by Lestrade *et al.* (1995), and the Hubble Space Telescope (HST) observations were analyzed by Kovalevsky *et al.* (1997).

The main difference between our approach and the approach of Kovalevsky *et al.* (1997) is that we included the following data:

(1) The results of a comparison of the proper motions for PUL2 and Hipparcos stars (Bobylev *et al.* 2004);

(2) The results of a comparison of the proper motions for SPM2 and Hipparcos stars (Zhu 2001);

(3) The results of a comparison of the proper motions for NPM2 and Hipparcos stars (Zhu 2003);

(4) The results of a comparison of the VLA absolute proper motions for radio stars and their Hipparcos proper motions.

Table 1 gives the components of the vector ω that we calculated using the absolute proper motions of 15 radio stars from Boboltz *et al.* (2003). These authors described in detail the project and the method of referencing the observations of radio stars to quasars and compared these stars with the Hipparcos catalog, but did not determine the components of the vector ω. We used the equations in the form that was proposed and used by Lindegren and Kovalevsky (1995):

$$\Delta\mu_\alpha \cos\delta = \omega_x \cos\alpha \sin\delta + \omega_y \sin\alpha \sin\delta - \omega_z \cos\delta, \quad (1)$$

$$\Delta\mu_\delta = -\omega_x \sin\alpha + \omega_y \cos\alpha, \quad (2)$$

where the Hipparcos catalog differences are on the left-hand sides of the equations. Here, $\sigma_\circ$ is the error per unit weight in the solution of Eqs. (1) and (2). The VLA (Boboltz *et al.* 2003) and VLBI (Lestrade *et al.* 1995, 1999) absolute proper motions are independent.

Our approach also differs from that of Kovalevsky *et al.* (1997) in that we used the results of a comparison of the NPM1 and Hipparcos stellar proper motions performed by the Heidelberg team, which were obtained from the data for 2616 stars, to determine ω_z. The random errors in ω_z, ω_y, and ω_z for the Heidelberg solution are given only for the sample of 1135 stars ($e_{\omega_x} = 0.25$ mas yr^{-1} and $e_{\omega_y} = e_{\omega_z} = 0.2$ mas yr^{-1}). The corresponding errors for the sample of 2616 stars are smaller by a factor of $\approx\sqrt{2616/1135}$. Since there are problems with the NPM1 catalog, we assumed the random errors to be 0.25 mas yr^{-1} for ω_x and 0.20 mas yr^{-1} for ω_y and ω_z in order not to overestimate this solution. Our choice of this solution was dictated by the fact that it was obtained in the magnitude range 10.5^m–11.5^m. As can be seen in Fig. 1c from Platais *et al.* (1998b), the Hipparcos–NPM1 proper-motion differences have a horizontal pattern near zero precisely in this magnitude range. In our opinion, the NPM1 proper motions are least affected by the magnitude equation in this magnitude range. In addition, we used only one of the available (not independent) results of a comparison of the SPM1 and Hipparcos catalogs, the YVA solution (Kovalevsky *et al.* 1997; Platais *et al.* 1998b).

DETERMINING THE VECTOR $\boldsymbol{\omega}$

We assigned a weight inversely proportional to the square of the error e in the corresponding quantities ω_x, ω_y, and ω_z to each comparison catalog, which was calculated using the formula

$$P_i = {e_{\rm kiev}}^2/{e_i}^2, \quad i = 1, \dots, 12, \quad (3)$$

where i is the number of individual sources, and $e_{\rm kiev}$, the random error of the GPM1 (Kiev) program. Table 2 contains the data used here. The second column of the table gives the weights calculated using formula (3). Not all of the authors use equations in the form (1) and (2). In such cases, we reduced the signs

Table 1. Components of the vector $\boldsymbol{\omega}$—ω_x, ω_y, and ω_z (in mas yr^{-1}) that we determined from the VLA–Hipparcos differences using data from Boboltz *et al.* (2003).

Number of stars	σ_0	ω_x	ω_y	ω_z
15 (all)	± 2.06	-0.97 ± 0.62	-1.59 ± 0.73	$+0.18 \pm 0.63$
12	± 1.63	-0.42 ± 0.56	-0.51 ± 0.64	$+0.20 \pm 0.57$

* The radio stars HD 50896 N, KQ Pup, and RS CVn were rejected.

Table 2. (Equatorial) components of the vector of residual rotation of the Hipparcos catalog with respect to extragalactic objects—ω_x, ω_y, ω_z (mas yr^{-1}).

	P_x, P_y, P_z	N_*	$N_{\rm area}$	ω_x	ω_y	ω_z
NPM2	16.00/4.62/8.16	3519	347	-0.11 ± 0.20	-0.19 ± 0.20	-0.75 ± 0.28
SPM2	22.15/9.43/28.44	9356	156	$+0.10 \pm 0.17$	$+0.48 \pm 0.14$	-0.17 ± 0.15
NPM1	10.24/4.62/16.00	2616	899	-0.76 ± 0.25	$+0.17 \pm 0.20$	-0.85 ± 0.20
SPM1	44.44/5.71/130.61	4067	63	$+0.44 \pm 0.12$	$+0.71 \pm 0.18$	-0.30 ± 0.07
PUL2	2.90/1.28/3.63	1004	147	-0.98 ± 0.47	-0.03 ± 0.38	-1.66 ± 0.42
Kiev(GPM1)	1.0/1.0/1.0	415	154	-0.27 ± 0.80	$+0.15 \pm 0.60$	-1.07 ± 0.80
Potsdam	2.37/0.74/2.78	256	24	$+0.22 \pm 0.52$	$+0.43 \pm 0.50$	$+0.13 \pm 0.48$
Bonn	5.54/2.96/5.88	88	13	$+0.16 \pm 0.34$	-0.32 ± 0.25	$+0.17 \pm 0.33$
VLBI	7.11/2.74/7.11	12		-0.16 ± 0.30	-0.17 ± 0.26	-0.33 ± 0.30
VLA+PT	2.04/0.45/1.97	12		-0.42 ± 0.56	-0.51 ± 0.64	$+0.20 \pm 0.57$
HST	0.08/0.08/0.05	46		-1.60 ± 2.87	-1.92 ± 1.54	$+2.26 \pm 3.42$
EOP	8.16/2.36/–			-0.93 ± 0.28	-0.32 ± 0.28	–
Mean 1				$+0.04 \pm 0.15$	$+0.18 \pm 0.12$	-0.35 ± 0.09
Mean 2				-0.19 ± 0.16	$+0.08 \pm 0.11$	-0.43 ± 0.15

Note: $N_\star$ is the number of common comparison stars, and $N_{\rm area}$ is the number of comparison areas common to the photographic catalogs. Mean 2 was calculated without SPM1.

of the quoted quantities (Zhu 2001, 2003) to the same form.

The lower part of Table 2 gives the weighted means of ω_x, ω_y, and ω_z. Mean 1 was calculated using all of the available data in Table 2. The SPM1 and SPM2 catalogs are not independent, but the methods of obtaining the solutions differ. The SPM1 solution (Platais *et al.* 1998b) was obtained only from the differences in $\mu_\alpha \cos\delta$ (e.g., only from Eq. (1)). The SPM2 solution (Zhu 2001) was obtained by simultaneously solving Eqs. (1) and (2); the author pointed out that there is a color equation in the SPM2 catalog, which was not eliminated, and it is more pronounced in the μ_δ differences. We calculated Mean 2 without using the SPM1 solution in order to analyze only independent sources. In this case, the SPM proper motions also have the largest weight when calculating the component ω_z, as can be seen from the table. A comparison of Means 1 and 2 reveals no significant differences between these two solutions, with ω_z being an appreciable component. The errors of the vector ω along the three axes $e_\omega = \sqrt{e_{\omega_x}{}^2 + e_{\omega_y}{}^2 + e_{\omega_z}{}^2}$ are ±0.21 and ±0.25 mas yr^{-1} for Mean 1 and 2 solutions, respectively. Our solutions for the components ω_x and ω_y do not differ significantly from the final solutions of Kovalevsky *et al.* (1997) based on both Lindegren's and Kovalevsky's methods. At the same time, there is a significant difference in the determination of ω_z, which we found to differ significantly from zero. The figure shows the projections of the individual solutions for the vector $\boldsymbol{\omega}$ onto the xy, xz, and yz planes based on the data from Table 2. Also shown in the figure are the components of our Mean 1 solution.

DISCUSSION

The effects of the actual motions of stars in the differences between the catalogs under consideration are ruled out. Therefore, the causes of the rotation ω_z found are the following:

(1) Inaccurate realization of the ICRS or, in other words, residual rotation of the Hipparcos catalog with respect to the ICRF (Ma *et al.* 1998), and, in this case, the rotation found is of a "technical" nature;

(2) Residual rotation of the ICRF itself with respect to the extragalactic reference frame. The ICRF is based on ground-based VLBI observations of extragalactic radio sources. It may be assumed that, in this case, the rotation ω_z found is precessional in nature and depends on the accuracy of the constants used. Given the form of the proper-motion differences and the signs on the right-hand sides of Eqs. (1)–(2), we can write

$$\omega_y = -\Delta p_1 \sin\varepsilon, \tag{4}$$

$$\omega_z = \Delta p_1 \cos\varepsilon - \Delta E, \tag{5}$$

where Δp_1 is the correction to the adopted constant of lunisolar precession in longitude, ΔE is the sum of the corrections to the rate of planetary precession and the motion of the zero point of right ascensions, and ε is the inclination of the ecliptic to the equator. Using only Eq. (5) and setting $\Delta E = 0$, we obtain from our Mean 1 solution

$$\Delta p_1 = -0.38 \pm 0.10 \ \text{mas yr}^{-1}. \tag{6}$$

This value agrees with the result of our previous work (Bobylev 2004), where we found $\Delta p_1 = -0.42 \pm 0.10$ mas yr^{-1} from a kinematic analysis of the proper motions for distant Hipparcos stars. In our opinion, a comparison of the residual rotations around the ecliptic axis found by two independent methods is most justifiable.

Since Ma *et al.* (1998) adopted the correction $\Delta p_1 = -2.84 \pm 0.04$ mas yr^{-1} to the IAU (1976)

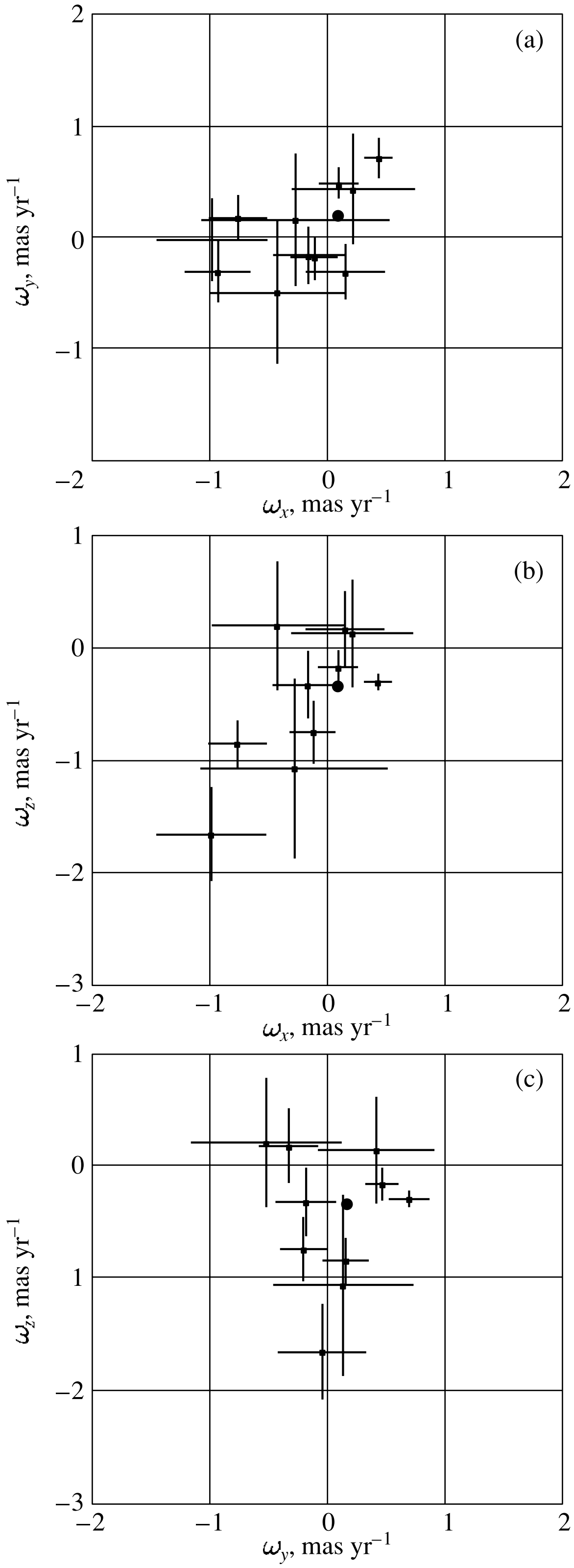

Fig. 1. Projections of the individual solutions (without HST) for the vector $\boldsymbol{\omega}$: (a) onto the xy plane; (b) onto the xz plane, and (c) onto the yz plane. The filled circle indicates the components of our Mean 1 solution.

constant of lunisolar precession in longitude, it may be assumed that Δp_1 was underestimated. Since the ICRS was constructed with precisely this value, solution (6) yields an "addition" to this correction. In this case, the correction to the IAU (1976) constant of lunisolar precession in longitude is

$$\Delta p_1 = -3.22 \pm 0.11 \text{ mas yr}^{-1}. \quad (7)$$

Solution (7) is in satisfactory agreement with the most recent results from the laser ranging of the Moon, $\Delta p_1 = -3.02 \pm 0.03$ mas yr^{-1} (Chapront *et al.* 2002), and with the results of an analysis of radio interferometric observations, $\Delta p_1 = -3.011 \pm 0.003$ mas yr^{-1} (Fukushima 2003).

On the other hand, if we assume that the lunisolar precession has no effect on the construction of ICRS and ICRF, then $\Delta E \neq 0$. In this case, we find from Eq. (5) that

$$\Delta E = +0.38 \pm 0.10 \text{ mas yr}^{-1}. \quad (8)$$

The residual rotation of the Hipparcos catalog that we found is small. An analysis of the radio-interferometric observations (Boboltz *et al.* 2003) performed 9.69 years after (epoch 2000.94) the construction of ICRS (epoch 1991.25) revealed no significant effect in the coordinates of radio stars. However, the rotation components obtained by Boboltz *et al.* (2003) from the coordinate differences for 18 radio stars (Kovalevsky *et al.* 1997) are of considerable interest:

$$\varepsilon_{0x} = +0.2 \pm 2.9 \text{ mas}, \quad (9)$$

$$\varepsilon_{0y} = +1.9 \pm 3.2 \text{ mas}, \quad (10)$$

$$\varepsilon_{0z} = -2.3 \pm 2.8 \text{ mas}. \quad (11)$$

We changed the signs of the components of the vector ε inferred by Boboltz *et al.* (2003) in order to have Hipparcos catalog differences comparable with those analyzed. To compare results (9)–(11), for example, with the Mean 1 solution, the quantities $\varepsilon_{0x,y,z}$ must be divided by the epoch difference. Thus, the difference ε_{0z}, which is determined with the smallest random error, is largest among quantities (9)–(11), thereby confirming our ω_z value. In general, quantities (9)–(11) agree well with the Mean 1 solution.

Our analysis of the available individual sources for controlling the ICRS inertiality shows that they are of little use for analyzing future projects, such as GAIA, SIM, etc., in which a microacrsecond accuracy is expected to be reached (Kovalevsky *et al.* 1999). The idea that the inertiality must be controlled using quasar observations from a spacecraft directly during its flight (Metz and Geffert 2004) seems most promising.

CONCLUSIONS

We have confirmed that the error in referring the ICRS to the inertial reference frame is very small and does not exceed ± 0.25 mas yr^{-1} (along the three axes).

We showed that the equatorial component $\omega_z = -0.35 \pm 0.09$ mas yr^{-1} of the vector of residual rotation of the ICRS with respect to the inertial reference frame differs significantly from zero. This confirms the result of a kinematic analysis of the proper motions for stars of the ICRS catalogs (Bobylev 2004).

ACKNOWLEDGMENTS

This work was supported by the Russian Foundation for Basic Research (project no. 02-02-16570).

REFERENCES

1. D. A. Boboltz, A. L. Fey, K. J. Johnston, *et al.*, Astron. J. **126**, 484 (2003).
2. V. V. Bobylev, Pis'ma Astron. Zh. **30**, 289 (2004) [Astron. Lett. **30**, 251 (2004)].
3. V. V. Bobylev, N. M. Bronnikov, and N. A. Shakht, Pis'ma Astron. Zh. **30**, 519 (2004).
4. J. Chapront, M. Chapront-Touzé, and G. Francou, Astron. Astrophys. **387**, 700 (2002).
5. A. N. Deutch, Trans. IAU **8**, 789 (1954).
6. A. N. Deutch, V. V. Lavdovskii, and N. V. Fatchikhin, Izv. Gos. Astron. Obs. **154**, 14 (1955).
7. T. Fukushima, Astron. J. **126**, 494 (2003).
8. M. Geffert, A. R. Klemola, M. Hiesgen, *et al.*, Astron. Astrophys. **124**, 157 (1997).
9. R. B. Hanson, A. R. Klemola, B. F. Jones, *et al., Lick Northern Proper Motion Program: NPM2 Catalog*, http://www.ucolick.org/~npm/NPM2/ (2003).
10. *The HIPPARCOS and Tycho Catalogues,* ESA SP-1200 (ESA, 1997).
11. S. Hirte, E. Schilbach, and R.-D. Scholz, Astron. Astrophys., Suppl. Ser. **126**, 31 (1996).
12. V. S. Kislyuk, S. P. Rybka, A. I. Yatsenko, *et al.*, Astron. Astrophys. **321**, 660 (1997).
13. A. R. Klemola, R. B. Hanson, and B. F. Jones, *Galactic and Solar System Optical Astrometry,* Ed. by L. V. Morrison and G. F. Gilmore (Cambridge Univ. Press, Cambridge, 1994), p. 20.
14. A. R. Klemola, B. F. Jones, and R. B. Hanson, Astron. J. **94**, 501 (1987).
15. J. Kovalevsky, *JOURNÉES 1999,* Ed. by M. Soffel and N. Capitane (Obs. de Paris, Paris, 1999), p. 103.
16. J. Kovalevsky, L. Lindegren, M. A. C. Perryman, *et al.*, Astron. Astrophys. **323**, 620 (1997).
17. J.-F. Lestrade, D. L. Jones, R. A. Preston, *et al.*, Astron. Astrophys. **304**, 182 (1995).
18. J.-F. Lestrade, R. A. Preston, D. I. Jones, *et al.*, Astron. Astrophys. **344**, 1014 (1999).
19. L. Lindegren and J. Kovalevsky, Astron. Astrophys. **304**, 189 (1995).

20. C. Ma, E. F. Arias, T. M. Eubanks, *et al.*, Astron. J. **116**, 516 (1998).
21. M. Metz and M. Geffert, Astron. Astrophys. **413**, 771 (2004).
22. I. Platais, T. M. Girard, V. Kozhurina-Platais, *et al.*, Astron. J. **116**, 2556 (1998a).
23. I. Platais, T. M. Girard, W. F. van Altena, *et al.*, Astron. Astrophys. **304**, 141 (1995).
24. I. Platais, V. Kozhurina-Platais, T. M. Girard, *et al.*, Astron. Astrophys. **331**, 1119 (1998b).
25. S. P. Rybka and A. I. Yatsenko, Kinemat. Fiz. Neb. Tel **13**, 70 (1997a).
26. S. P. Rybka and A. I. Yatsenko, Astron. Astrophys., Suppl. Ser. **121**, 243 (1997b).
27. H.-J. Tucholke, P. Brosche, and M. Odenkirchen, Astron. Astrophys., Suppl. Ser. **124**, 157 (1997).
28. J. Vondrák, C. Ron, and I. Pešek, Astron. Astrophys. **319**, 1020 (1997).
29. Zi Zhu, Publ. Astron. Soc. Jpn. **53**, L33 (2001).
30. Zi Zhu, Presentation at *JOURNÉES 2003* (Obs. de Paris, Paris, 2003).

Translated by A. Dambis

Astronomy Letters, Vol. 30, No. 12, 2004, pp. 854–862. Translated from Pis'ma v Astronomicheskiĭ Zhurnal, Vol. 30, No. 12, 2004, pp. 936–945.

Effects of Stellar Wind, Dynamical Friction, and Star Mergers on the Dynamical Evolution of Multiple Stars

A. V. Rubinov, A. V. Petrova, and V. V. Orlov*

Sobolev Astronomical Institute, St. Petersburg State University, Universitetskiĭ pr. 28, St. Petersburg, Peterhof, 198504 Russia

Received March 9, 2004

Abstract—The dynamical evolution of small stellar groups composed of $N = 6$ components was numerically simulated within the framework of a gravitational N-body problem. The effects of stellar mass loss in the form of stellar wind, dynamical friction against the interstellar medium, and star mergers on the dynamical evolution of the groups were investigated. A comparison with a purely gravitational N-body problem was made. The state distributions at the time of 300 initial system crossing times were analyzed. The parameters of the forming binary and stable triple systems as well as the escaping single and binary stars were studied. The star-merger and dynamical-friction effects are more pronounced in close systems, while the stellar-wind effects are more pronounced in wide systems. Star mergers and stellar wind slow down the dynamical evolution. These factors cause the mean and median semimajor axes of the final binaries as well as the semimajor axes of the internal and external binaries in stable triple systems to increase. Star mergers and dynamical friction in close systems decrease the fraction of binary systems with highly eccentric orbits and the mean component mass ratios for the final binaries and the internal and external binaries in stable triple systems. Star mergers and dynamical friction in close systems increase the fraction of stable triple systems with prograde motions. Dynamical friction in close systems can both increase and decrease the mean velocities of the escaping single stars, depending on the density of the interstellar medium and the mean velocity of the stars in the system. © *2004 MAIK "Nauka/Interperiodica"*.

Key words: *celestial mechanics, stellar dynamics*.

INTRODUCTION

Observations of star-forming regions and young T Tauri stars suggest that a large fraction of the stars are probably formed in small groups (see, e.g., Larson (2001) and references therein). Recent numerical experiments on the fragmentation of molecular clouds have shown that this process can produce nonhierarchical stellar systems with different numbers of components (see, e.g., Boss 1993; Truelove *et al.* 1998). The gravitational interaction between the members of a group can cause it to break up. According to the hypothesis of van Albada (1968), the breakup of young multiple nonhierarchical stellar systems can give rise to observable wide binary and multiple stars.

Investigating the dynamical evolution of nonhierarchical multiple stellar systems is also of considerable interest in studying the evolution of open stellar clusters. Numerical simulations of the formation of open stellar clusters (Bonnell *et al.* 2003) suggest that a possible scenario for their formation is the hierarchical fragmentation of a molecular cloud. In this case, the distribution of protostars in the cloud is nonuniform. They form low-multiplicity groups that contain from several to several tens of stars. Subsequently, the groups merge together to form a single cluster in a time of $\sim 3 \times 10^5$ yr. The local number density of stars $\rho_{\rm loc}$ (within the volume containing the ten nearest stars for a selected star) during the formation of stellar groups was estimated by the authors to be, on average, $\sim 10^5$ pc^{-3}, with its maximum values being $\sim 10^7 - 10^8$ pc^{-3}. This corresponds to group sizes of $\sim 10^2 - 10^4$ AU. Numerical simulations of the dynamical evolution of nonhierarchical multiple systems show that their half-life is less than (for close groups) or comparable to (for wide groups) the formation time of a single cluster through group mergers. These estimates suggest that both unevolved groups and groups whose dynamical evolution is near completion will merge. Thus, the results of dynamical studies of low-multiplicity stellar groups are applicable in studying the formation of open stellar clusters.

It should be noted that, apart from the gravitational interaction between stars, the dynamical evolution of low-multiplicity groups can also be affected by other factors. Nascent stars are embedded in a gaseous medium that exerts dynamical friction

*E-mail: `vor@astro.spbu.ru`

on the system's objects. In addition, young stars can lose their mass through stellar wind (up to $\sim 10^{-8} M_{\odot}$ yr^{-1}; see, e.g., the book by Surdin 1997). When stars approach one another at distances comparable to their sizes, star mergers can take place. The accretion of gas onto protostars can play an important role. In this paper, we estimate the effects of the dynamical friction of stars against the interstellar medium, stellar mass loss through stellar wind, and star mergers on the dynamical evolution of nonhierarchical multiple stars.

Only a few published works are devoted to simulating the dynamical evolution of stellar systems with $N > 3$ stars. The first works were done in the late 1960s–early 1970s by van Albada (1968) and Harrington (1975) for a few sets of initial conditions. In the mid 1990s, Sterzik and Durisen (1998) analyzed the distributions in final states and parameters of the binaries formed through the decay of nonhierarchical multiple systems composed of $N =$ 3, 4, 5 components for several initial mass functions. We can note several papers devoted to studying the parameters of the single stars expelled from a system during its evolution (Sterzik and Durisen 1995; Kiseleva *et al.* 1998). The authors of these papers considered a fairly wide range of initial conditions for nonhierarchical multiple systems.

Sterzik and Tokovinin (2002) compared the relative orbital orientations of the internal and external binaries, their period ratios, and the component mass ratios in stable triple systems that resulted from the dynamical evolution of small groups for a wide range of initial parameters with observable stable triple systems. Note also the paper by Sterzik and Durisen (2003) whose authors investigated the parameters of the binary brown dwarfs formed through the decay of nonhierarchical multiple systems ($N =$ 3–10) and compared them with observational data.

Delgado-Donate *et al.* (2002) investigated the dynamical evolution of nonhierarchical protostellar systems at early accretion phases. In this case, the bulk of the cloud is concentrated not in stars, but in gas. The presence of a gaseous component leads to the accretion of gas onto protostars and to the dynamical friction of protostars against the interstellar medium. Since much computational time is required to trace the evolution of the cloud until the end of the accretion stage, the number of sets of initial conditions considered is small. Nonetheless, the above authors performed a statistical analysis of the distribution in final states and parameters of the forming binary, triple, quadruple, and single stars.

Previously (Rubinov *et al.* 2002), we investigated the dynamical evolution of nonhierarchical multiple stellar systems with star mergers for various initial numbers of components N. We performed our simulations at fixed initial values of the system's size R and virial coefficient k for two mass functions. We considered the parameters of the escaping single stars as well as the forming binary and stable triple systems. Rubinov (2004) analyzed the dependence of the results of the dynamical evolution of nonhierarchical multiple systems on R and k for three different mass functions.

In this paper, we investigate the effects of the dynamical friction of stars against the interstellar medium, stellar mass loss in the form of stellar wind, and star mergers on the dynamical evolution of nonhierarchical multiple stellar systems.

NUMERICAL SIMULATIONS

We simulated the dynamical evolution of nonhierarchical multiple systems within the framework of the gravitational problem of N point masses. The numerical simulation technique and the algorithm of allowance for star mergers were described in our previous paper (Rubinov *et al.* 2002). In this paper, we point out the most important features of the method and consider its modifications required to incorporate additional effects.

We performed our simulations by numerically integrating regularized equations of motion using the chain regularization method proposed by Mikkola and Aarseth (1993). We fixed the escapes of single and binary stars when they recede sufficiently from the center of mass of the remaining bodies and when they are isolated from the remaining components of the group.

The dynamical evolution was traced over a period of $300T_{\mathrm{cr}}$, where

$$T_{\mathrm{cr}} = \frac{G}{(2|E|)^{\frac{3}{2}}} \sum_{i<j} m_i m_j \sqrt{\sum_{k=1}^{N} m_k} \qquad (1)$$

is the initial mean system crossing time. Here, G is the gravitational constant, E is the total energy of the system, and m_i is the mass of star i. If the initial system decayed to a binary, the integration was also ceased.

A fourth-order Runge–Kutta integrator with an automatically chosen step was used to numerically solve the equations of motion. When the equations of motion allowed the existence of integrals of motion, the latter were used to check the computational accuracy. In this case, the relative errors of the energy and area integrals did not exceed 10^{-5} over the computational time, while the integrals of motion for the center of mass were conserved with a higher accuracy.

The initial conditions were specified as follows. The simulations were performed for systems that initially consisted of $N = 6$ stars. The stars at the initial time were assumed to be distributed uniformly and randomly within a sphere of radius R. The velocities of the stars were chosen in such a way that the system was in virial equilibrium; the velocity distribution was assumed to be isotropic.

We analyzed the dependence of the dynamical evolution results on the system's initial mass function. For this purpose, we considered three different mass functions: equal masses (the mass of each stars was equal to the solar mass); a Salpeter mass function (Salpeter 1955):

$$f(m) \sim m^{-2.35}, \quad m \in [0.4; 10]M_{\odot}; \tag{2}$$

and a power-law mass function with an index of -1.5,

$$f(m) \sim m^{-1.5}, \quad m \in [0.9; 10]M_{\odot}. \tag{3}$$

The latter initial mass function was chosen for the following reasons. This mass function is intermediate in index between the Salpeter mass function and the case of equal masses. In addition, the cores of the molecular clouds out of which stars are formed may have a clumpy fractal structure. The fragment mass distribution within the cloud can then be described by a power law with an index from -2.0 to -1.5 (see, e.g., Elmegreen and Falgarone 1996).

The stellar mass loss in the form of stellar wind was taken into account as follows. At each integration step, the mass m_i of each star in the system decreased by $\Delta m_i = \dot{m}\Delta t$, where $\dot{m}$ is the mass loss rate, and Δt is the integration step. Since the intensity of the stellar wind was low, we considered the evolution of wide systems ($R = 100, 1000$ AU) in which much of the system's mass could be carried away into the interstellar medium over the evolution time. We performed our analysis both for overestimated intensities of the stellar wind ($\dot{m} = 10^{-6} m_* \text{ yr}^{-1}$) and for real young stars ($\dot{m} = 10^{-8} M_{\odot} \text{ yr}^{-1}$). Here, m_* is the current stellar mass.

The effect of the dynamical friction of stars against a gaseous medium implies that the gravitational interaction of stars with gas particles decreases the stellar velocity. To describe this effect, we used a formula from the paper by Chandrasekhar (1943) (see also the book by Binney and Tremaine 1987) by assuming the velocity distribution of the gas particles to be Maxwellian:

$$\frac{d\overline{V}_j}{dt} = -\frac{4\pi \ln \Lambda G^2 \rho m_j}{V_j^3} \tag{4}$$

$$\times \left[\operatorname{erf}\left(\frac{V_j}{\sqrt{2\sigma}}\right) - \frac{2V_j}{\sqrt{2\pi\sigma}} e^{-\frac{V_j^2}{2\sigma}}\right]\overline{V}_j,$$

$$\operatorname{erf}(X) = \frac{2}{\sqrt{\pi}} \int_0^X e^{-t^2} dt, \tag{5}$$

$$\Lambda = \frac{b_{\max} V_0^2}{G m_j}, \tag{6}$$

where $\overline{V}_j$ is the velocity vector of the star with mass m_j, V_0 is the typical stellar velocity in the system, $b_{\max}$ is the maximum distance at which the gas particles have a significant effect on the star, σ is the gas particle velocity dispersion, and ρ is the density of the gaseous cloud.

If the squares of the stellar velocities are comparable to the gas velocity dispersion, then we may use an approximation of formula (4) that is simpler in form:

$$\frac{d\overline{V}_j}{dt} = -\frac{16\pi^2}{3} \frac{\ln \Lambda G^2 \rho m_j \overline{V}_j}{(2\pi\sigma)^{3/2}}. \tag{7}$$

Since the dynamical friction is enhanced as the velocity of the system's stars increases, its effect will be stronger in close systems. We investigated the effect of dynamical friction (formula (4)) on the evolution of nonhierarchical multiple systems with radii of $R = 3$, 10, and 100 AU. At $R = 100$ AU, we considered two gas densities, 5×10^{-20} and 10^{-16} g cm^{-3}. For the remaining values of R, we considered only a high gas density, $\rho = 10^{-16}$ g cm^{-3}.

Since the probability of collisions between stars in close systems is higher than that in wide systems, we investigated the effect of star–star collisions on the dynamical evolution of nonhierarchical multiple systems only for small values of the parameter $R = 3, 10$ AU.

For each set of parameters, we considered 500 sets of initial conditions.

SIMULATION RESULTS

The Distribution in States

By analyzing the distribution in states at the end of the integration, we can determine what systems and with what probability are formed through the dynamical decay of nonhierarchical multiple stars. As in our previous papers (Rubinov *et al.* 2002; Rubinov 2004), we distinguished the following states: a binary with a negative total energy, a binary with a positive total energy (two single stars), a stable triple system, an unstable triple system, and a system of higher multiplicity. The triple systems were separated into stable and unstable ones by using an analytical criterion proposed by Golubev (1967). When using this criterion, the term "stability" should be understood as the stability against the exchange of a component of

Distribution in states as a function of the system's initial size at time $300T_{cr}$

Additional effects	R, AU	Mass function	Final binaries	Two singles	Stable triples	Unstable triples	Higher multiplicity
No	3	PM	0.56	0.01	0.15	0.18	0.10
No	3	SM	0.55	0.02	0.18	0.15	0.10
No	3	EM	0.56	0.06	0.15	0.08	0.15
Dynamical friction	3	PM	0.55	0.02	0.07	0.23	0.13
Dynamical friction	3	SM	0.48	0.02	0.11	0.23	0.16
Dynamical friction	3	EM	0.47	0.02	0.09	0.17	0.25
Mergers	3	PM	0.47	0.02	0.08	0.27	0.16
Mergers	3	SM	0.51	0.01	0.11	0.21	0.16
Mergers	3	EM	0.45	0.02	0.08	0.19	0.26
Dynamical friction	100	PM	0.74	0.02	0.10	0.10	0.04
Dynamical friction	100	SM	0.80	0.02	0.09	0.05	0.04
Dynamical friction	100	EM	0.72	0.07	0.04	0.06	0.11
Stellar wind	100	PM	0.54	0.02	0.14	0.19	0.11
Stellar wind	100	SM	0.60	0.01	0.11	0.16	0.12
Stellar wind	100	EM	0.58	0.04	0.13	0.08	0.17
Mergers	100	PM	0.57	0.02	0.19	0.11	0.11
Mergers	100	SM	0.55	0.02	0.18	0.18	0.07
Mergers	100	EM	0.57	0.07	0.06	0.15	0.15
Stellar wind	1000	PM	0.53	0.00	0.09	0.15	0.23
Stellar wind	1000	SM	0.36	0.00	0.07	0.16	0.41
Stellar wind	1000	EM	0.35	0.02	0.07	0.09	0.47
Mergers	1000	PM	0.55	0.02	0.16	0.17	0.10
Mergers	1000	SM	0.56	0.02	0.17	0.15	0.10
Mergers	1000	EM	0.55	0.05	0.15	0.08	0.17

the internal pair for the distant component, i.e., the preservation of the hierarchy.

The table gives the distribution in states both with allowance for the mutual gravitational attraction between the stars alone and with allowance for the dynamical friction, star mergers, and stellar wind for various initial mass functions. If the mass loss is taken into account, the stellar wind intensity is $\dot{m} = 10^{-6} m_* \text{ yr}^{-1}$; if the dynamical friction effect is taken into account, the gas density is $\rho = 10^{-16}$ g cm^{-3}. In the table, PM, SM, and EM denote the systems with the initial mass function (3), the Salpeter mass function, and the case of equal masses, respectively.

A comparison of the state distribution for two samples consisting of 500 sets of the same initial size and mass function for a purely gravitational problem showed that the uncertainty of these distributions is about 0.03.

Let us highlight the properties of systems that do not depend on the stellar-wind density, the gas density, and the star merger rate. In general, the dynamical evolution ends with the formation of a final binary system. The formation probability of a stable triple system is also rather high (5–20%). Not all of the nonhierarchical systems complete their dynamical evolution in 300 T_{cr}, as illustrated by the last column of the table.

Analyzing the last columns of the table, we conclude that dynamical friction speeds up the dynamical evolution of wide nonhierarchical multiple systems

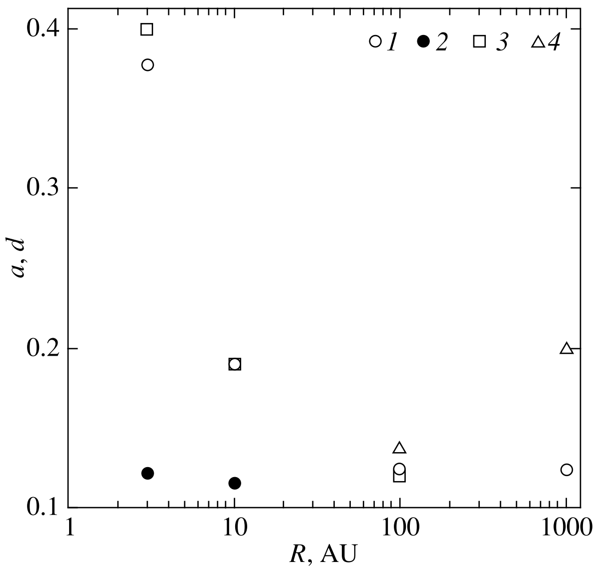

Fig. 1. Median semimajor axes of the final binaries versus initial system radius R for the mass function (3): the calculations with mergers (*1*), without mergers (*2*), with dynamical friction and mergers (*3*), and with stellar wind and mergers (*4*). The semimajor axes are given in units of the system mean initial size (8).

($R = 100$ AU), with the number of stable triple systems decreasing. The decrease in the stellar velocities due to dynamical friction probably causes the probability of close encounters with intense energy exchange between the stars to increase. The increase in the rate of energy exchange between the stars generally causes the rate of star dissipation from the system to increase, which speeds up the dynamical evolution of nonhierarchical multiple systems. In closer systems, dynamical friction has no significant effect on the rate of dynamical evolution. This may be because the stellar velocities in close systems are, on average, higher than those in wide systems. The gas density is too low to significantly decrease the stellar velocities and, thereby, to increase the probability of close encounters.

In wide systems ($R = 1000$ AU), the stellar mass loss in the form of stellar wind generally slows down the dynamical evolution. This is probably attributable to a reduction in the effect of gravitational focusing and, hence, to a decrease in the probability of close binary and multiple encounters and, possibly, to an overall expansion of the system. In closer systems, the stellar-wind intensity is too low to significantly change the masses of the system's components over the time of its dynamical evolution. The stellar wind in such systems causes no significant slowdown in the dynamical evolution.

We see from the table that including star mergers causes the dynamical evolution of the system to slow down. This is probably attributable to a decrease in the number of close binary and multiple encounters, causing the stellar velocities to increase, and, accordingly, to an increase in the mean time of star dissipation from the system. One possible reason is that the probability of a merger during very close encounters can be higher than the probability of survival of the encountering stars and the kinetic energy redistribution between them.

Final Binaries

Studying the parameters of the final binaries is of considerable interest, because the dynamical evolution of nonhierarchical multiple systems ends with the formation of a final binary in more than half of the cases.

In Fig. 1, the median semimajor axes of the final binaries, in units of the system's mean initial size d, are plotted against the system's initial size for virial equilibrium and the initial mass function (3). The system's mean initial size d was calculated using the formula

$$d = \frac{G}{2|E|}\sum_{i<j} m_i m_j. \qquad (8)$$

The stellar-wind intensity and the gas density were taken to be the same as those in the previous section.

We see that, in general, the semimajor axes of the binaries account for several tenths of the system's initial size. The final binaries become closer as the initial size of nonhierarchical systems increases. This may be explained by the reduction in the fraction of close binaries resulting from the merging of their components and the overall expansion of groups due to the stellar wind. Star mergers in close systems and stellar wind in wide systems lead to the formation of wider final binaries (naturally, the binaries become wider in physical units; see Rubinov, 2004). The dynamical friction of stars against the interstellar medium has virtually no effect on the semimajor axes of the final binaries. These trends are maintained for all of the initial stellar mass functions considered.

Figure 2 shows the eccentricity distributions of the final binaries for the initial mass function (3) and $R = 3$ AU. The solid line represents the law $f(e) = 2e$ that was first obtained by Ambartsumyan (1937) for an equilibrium distribution of binaries in the stellar field. A similar law was obtained by Monaghan (1976) when studying the breakup of triple systems. We see that best agreement between the model and theoretical eccentricity distributions of the final binaries is achieved in a purely gravitational problem (the white columns of the histogram). Star mergers and the dynamical friction of stars against the interstellar medium cause the fraction of the final binaries with

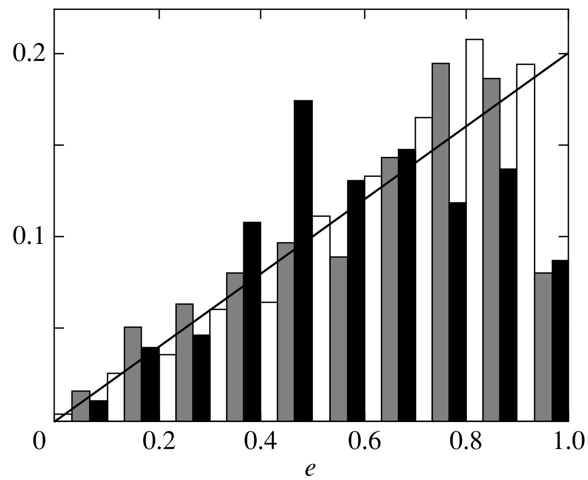

Fig. 2. Eccentricity distributions of the final binaries for the system's initial size $R = 3$ AU and mass function (3). The white, gray, and black columns of the histogram correspond to a purely gravitational problem, a problem with possible mergers, and a problem with possible mergers and dynamical friction. The solid line represents the law $f(e) = 2e$.

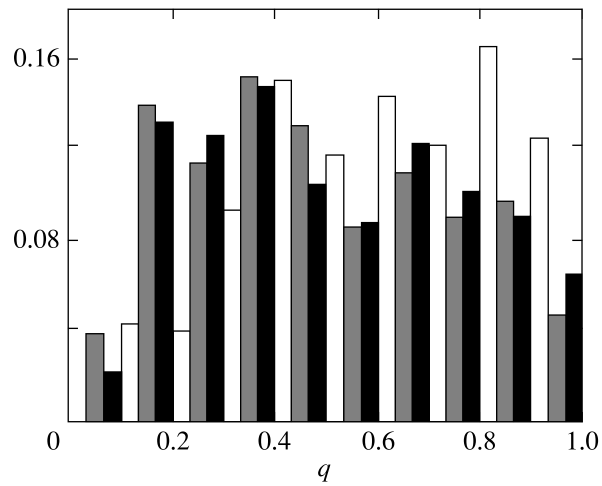

Fig. 3. Distributions of the component mass ratios for the final binaries for the system's initial size $R = 3$ AU and mass function (3). The notation is the same as that in Fig. 2.

eccentric orbits to decrease. This is probably because the probability of mergers in eccentric close binaries increases, particularly at the orbital periastron. These trends are also observed for the Salpeter mass function. In the case of equal masses, dynamical friction results in higher mean and median eccentricities of the final binaries than in the case of allowance for star mergers alone.

In wider systems, the effects of mergers and dynamical friction on the eccentricities of the final binaries are less pronounced. The stellar mass loss in the form of stellar wind causes no significant change in the mean and median eccentricities of the final binaries.

Figure 3 shows the distributions of the binary component mass ratio $q = m_1/m_2$ for the initial mass function (3) and $R = 3$ AU. Here, m_2 is the mass of the heavier component, and m_1 is the mass of the lighter component. We see that star mergers and dynamical friction in close systems generally cause the binary component mass ratio to decrease. A similar trend is also observed for the Salpeter mass function. Stellar wind has virtually no effect on the distribution of the component mass ratios for the final binaries.

Stable Triples

Analysis of the distribution in states indicates that the formation probability of stable triple systems is fairly high. It is of interest to study how star mergers, dynamical friction, and stellar wind affect the parameters of stable triple systems. We represent a triple system as a superposition of two binaries: internal and external. The internal binary is formed by the two closest stars of the system, while the external binary is formed by an object with the mass of the internal binary placed at its center of mass and the distant component of the system.

Analysis of the simulation results indicates that, in general, the semimajor axes of the internal binaries are one or two orders of magnitude smaller than the system's initial size, while the semimajor axes of the external binaries are comparable in order of magnitude to the system's initial size.

The behavior of the mean semimajor axes for the internal and external binaries as the system's initial size changes is similar to the behavior of the semimajor axes for the final binaries (see Fig. 1): star mergers in close systems and stellar wind in wide systems lead to the formation of wider internal and external binaries in stable triple systems.

Figure 4 shows the eccentricity distributions of the internal binaries for the initial mass function (3) in a purely gravitational problem, a problem with mergers, and a problem with dynamical friction and mergers. The system's mean initial size R is 3 AU. The solid line indicates the law $f(e) = 2e$. As for the final binaries (Fig. 2), the best agreement between the model and theoretical distributions is achieved for a purely gravitational problem. An increase in the probability of mergers in close eccentric internal binaries leads to a deficit of eccentric systems.

The eccentricities of the external binaries are, on average, lower than those of the internal binaries (the corresponding mean values are $\overline{e_{\rm ex}} \approx 0.5$ and $\overline{e_{\rm in}} \approx 0.7$). Star mergers and dynamical friction cause no

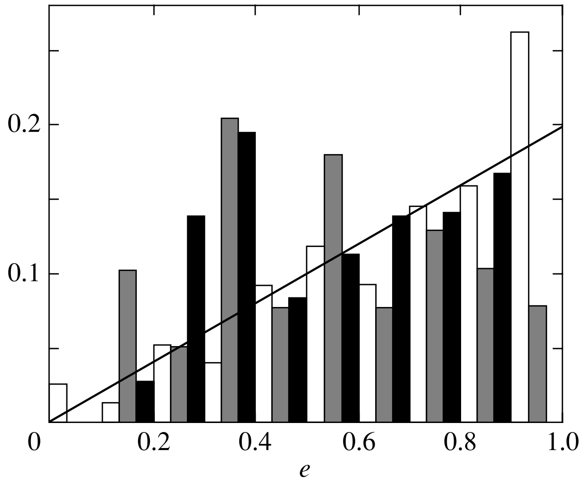

Fig. 4. Eccentricity distributions of the internal binaries in stable triple systems for the system's initial size $R = 3$ AU and mass function (3). The notation is the same as that in Fig. 2.

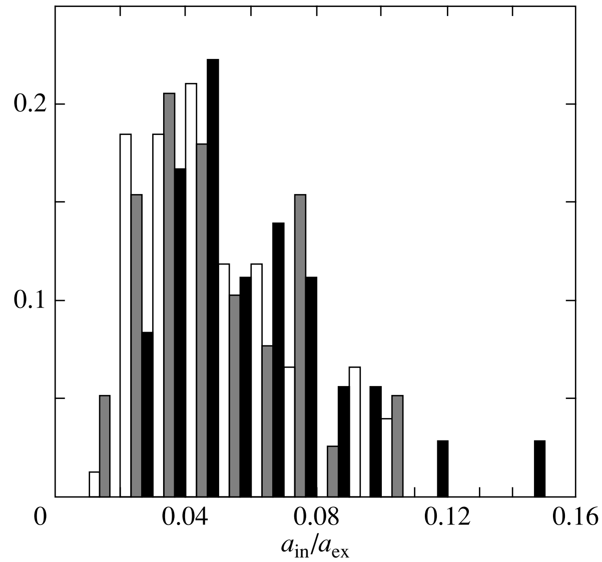

Fig. 5. Distributions of the ratios of the semimajor axes for internal and external binaries for the system's initial size $R = 3$ AU and the mass function (3). The notation is the same as that in Fig. 2.

change in the mean and median eccentricities of the external binaries. The stellar mass loss in the form of stellar wind has no strong effect on the orbital eccentricities of the external binaries.

The hierarchy of stable triple systems is rather strong, irrespective of the effects of additional factors. Figure 5 shows the distributions of the ratios of the semimajor axes for internal and external binaries in a purely gravitational problem, a problem with mergers, and a problem with dynamical friction and mergers. The ratio of the semimajor axes of the internal and external binaries is, on average, 1 : 20. This ratio is within the range 0.01 to 0.15.

Figure 6 shows the distributions of the angles between the orbital angular momentum vectors of the internal and external binaries in stable triple systems for the initial mass function (3) and the system's initial size $R = 3$ AU. We see that the distributions are similar in shape (unimodal) with the law $f(i) = \frac{1}{2}\sin i$ that corresponds to a random orientation of the orbital angular momentum vectors (solid line). However, the distributions for the model systems are skewed toward prograde motions. This is probably because the components must be more isolated for triples with retrograde motions to be stable according to Golubev's criterion. Star mergers and dynamical friction in close systems as well as stellar wind in wide groups generally cause no substatial decrease in the angle i. Dynamical friction increases the probability of star mergers and, thus, causes the mean angle i to decrease. This trend is observed in the case of equal stellar masses and the mass function (3). For the Salpeter initial mass function, it is indistinct. Stellar wind causes no significant change in the distribution of the angles between the orbital angular momentum vectors of the internal and external binaries.

As for the final binaries, star mergers and dynamical friction in close systems generally cause the component mass ratios of the internal binary, $q_1 = m_1/m_2$, and the external binary, $q_2 = m_3/(m_1 + m_2)$, in stable triple systems to decrease. Here, m_3 is the mass of the distant component of the triple, and m_1 and m_2 have the same meaning as that for the final binaries, but applied to the internal binary. Stellar wind in wide systems generally causes the parameter q_1 to slightly increase, but has virtually no effect on the parameter q_2.

Escaping Single Stars

Single and binary stars can escape from the system during the dynamical decay of nonhierarchical multiple stars. In this section, we consider some of the parameters of these objects.

In Fig. 7, the median velocities of the escaping single stars are plotted against the system's initial size for the mass function (3). Note that the median escape velocities increase with decreasing initial size of the system. The possible causes of this trend were discussed previously (Rubinov 2004). In addition, we see that dynamical friction for $R = 3$ AU slightly decreases the median escape velocities. At the same time, the reverse is true for $R = 10$ AU. This trend can be explained as follows. The stellar velocities in close systems are, on average, higher than those in wide systems due to an abundance of close

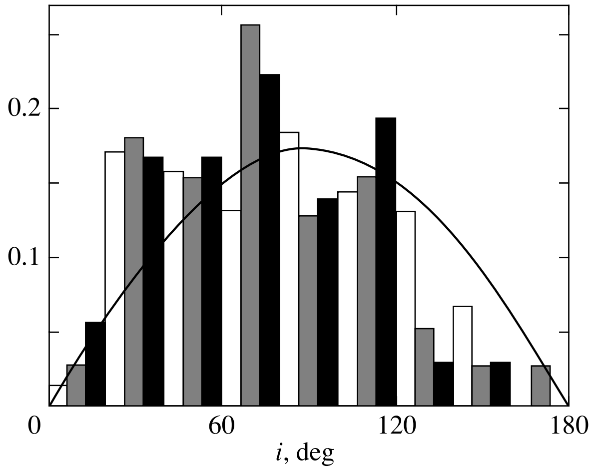

Fig. 6. Distributions of the angles between the orbital angular momentum vectors of the external and internal binaries for the system's initial size $R = 3$ AU and mass function (3). The notation is the same as that in Fig. 2. The solid line represents the law $f(i) = \frac{1}{2}\sin i$.

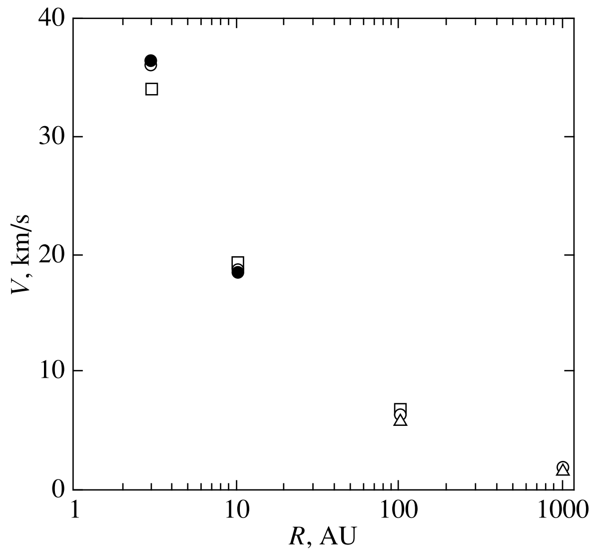

Fig. 7. Median velocities of the escaping single stars versus the system's initial size R for the initial mass function (3). The notation is the same as that in Fig. 1.

binary and multiple encounters. Since the dynamical friction is proportional to the stellar velocity (7), it will slow down the stellar motions in close systems more strongly than in wide systems. However, slowing down the stellar motions, dynamical friction increases the probability of close encounters and, hence, the velocities of the escaping stars. The stellar velocities in a system with $R = 3$ AU are, on average, higher than those in a system with $R = 10$ AU, and dynamical friction causes no large increase in the probability of close encounters. Here, the prevailing factor is the slowdown of the stellar motions through dynamical friction. For $R = 10$ AU, the stellar velocities in a system are lower, and the speedup of the stars through close encounters dominates over their slowdown through dynamical friction. This trend is also observed for the other mass functions considered.

Stellar wind in wide systems causes the mean and median velocities of the escaping stars to decrease slightly. Star mergers in close systems ($R = 3$ AU) generally cause a small decrease in the velocities of the escaping stars.

Similar trends are observed for the velocities of the escaping binaries, with their velocities being, on average, a factor of 1.5–2 lower than those of the single escaping stars.

CONCLUSIONS

Observations of star-forming regions and numerical simulations of star formation show that a fairly large number of stars can be formed within low-multiplicity groups (see, e.g., Larson 2001; Adams and Myers 2001). There may be an evolutionary stage of such systems when the gravitational attraction between the stars has a crucial effect on the subsequent evolution of the system. In this case, numerical integration of the equations for the gravitational N-body problem can be used for the study. However, apart from the gravitational interaction between the stars, the dynamics of the systems can also be affected by such factors as the dynamical friction of stars against the interstellar medium, the mass loss in the form of stellar wind, and star mergers. Here, we have investigated the dynamical evolution of systems affected by the above additional factors.

The following salient features of the dynamical evolution of nonhierarchical multiple systems can be noted:

(1) In general, the evolution of a system ends with the formation of a binary. The fraction of the stable triple systems is rather high, 5–20%. Star mergers in close systems and stellar wind in wide systems slow down the dynamical evolution. In moderately close systems ($R = 100$ AU), dynamical friction speeds up the dynamical evolution.

(2) Star mergers in close systems and stellar wind in wide systems increase the mean semimajor axes of the final binaries and those of the internal and external binaries in stable triple systems.

(3) The eccentricity distributions for the final binaries and internal binaries in stable triple systems can be described by the law $f(e) = 2e$. Star mergers and dynamical friction in close systems decrease the fraction of the binaries with eccentric orbits.

(4) Star mergers and dynamical friction increase the fraction of the final binaries as well as the internal

and external binaries in stable triple systems with components that differ widely in mass compared to a purely gravitational problem.

(5) In stable triple systems, the eccentricities of the external binaries are, on average, lower than those of the internal binaries ($\overline{e_{ex}} \approx 0.5$ and $\overline{e_{in}} \approx 0.7$).

(6) Stable triple systems have a rather strong hierarchy (the ratio of the semimajor axes of the internal and external binaries is, on average, 20 : 1).

(7) Triple systems with prograde motions dominate.

(8) Dynamical friction in close systems can both increase and decrease the mean velocities of the escaping single stars, depending on the density of the interstellar medium and the mean stellar velocities in the system.

ACKNOWLEDGMENTS

We wish to thank the Foundation for Support of Leading Scientific Schools (project no. 1078.2003.02), the Russian Foundation for Basic Research (project no. 02-02-17516), and the Universities of Russia Program of the Education Ministry of the Russian Federation (project no. UR.02.01.027) for financial support. A.V. Rubinov also wishes to thank the RF Ministry of Education's Program for the Support of Postgraduate Research at institutions of Higher Education (projects A03-2.9-403 and M03-2.3K-220). We are grateful to the referees for their valuable comments.

REFERENCES

1. F. C. Adams and P. C. Myers, Astrophys. J. **553**, 744 (2001).
2. V. A. Ambartsumyan, Astron. Zh. **14**, 207 (1937).
3. J. Binney and S. Tremaine, *Galactic Dynamics* (Princeton Univ. Press, Princeton, 1987).
4. I. A. Bonnell, M. R. Bate, and S. G. Vine, Mon. Not. R. Astron. Soc. **343**, 413 (2003).
5. A. P. Boss, Astrophys. J. **410**, 157 (1993).
6. S. Chandrasekhar, Astrophys. J. **97**, 255 (1943).
7. E. J. Delgado-Donate, C. J. Clarke, and M. R. Bate, Mon. Not. R. Astron. Soc. **342**, 926 (2002).
8. B. G. Elmegreen and E. Falgarone, Astrophys. J. **471**, 816 (1996).
9. V. G. Golubev, Dokl. Akad. Nauk SSSR **174**, 767 (1967).
10. R. S. Harrington, Astron. J. **80**, 1081 (1975).
11. L. Kiseleva, J. Colin, B. Dauphole, *et al.*, Mon. Not. R. Astron. Soc. **301**, 759 (1998).
12. R. B. Larson, *IAU Symp. No. 200: The Formation of Binary Stars*, Ed. by H. Zinnecker and R. D. Mathieu (2001), p. 93.
13. S. Mikkola and S. J. Aarseth, Cel. Mech. Dyn. Astron. **57**, 439 (1993).
14. J. J. Monaghan, Mon. Not. R. Astron. Soc. **176**, 63 (1976).
15. A. V. Rubinov, Astron. Zh. **81**, 50 (2004) [Astron. Rep. **48**, 45 (2004)].
16. A. V. Rubinov, A. V. Petrova, and V. V. Orlov, Astron. Zh. **79**, 1044 (2002) [Astron. Rep. **46**, 942 (2002)].
17. E. E. Salpeter, Astrophys. J. **121**, 161 (1955).
18. M. F. Sterzik and R. H. Durisen, Astron. Astrophys. **304**, L9 (1995).
19. M. F. Sterzik and R. H. Durisen, Astron. Astrophys. **339**, 95 (1998).
20. M. F. Sterzik and R. H. Durisen, Astron. Astrophys. **400**, 1031 (2003).
21. M. F. Sterzik and A. A. Tokovinin, Astron. Astrophys. **384**, 1030 (2002).
22. V. G. Surdin, *The Birth of Stars* (URSS, Moscow, 1997) [in Russian].
23. J. K. Truelove, R. I. Klein, C. F. McKee, *et al.*, Astrophys. J. **495**, 821 (1998).
24. T. van Albada, Bull. Astron. Neth. **19**, 479 (1968).

Translated by V. Astakhov

Astronomy Letters, Vol. 30, No. 12, 2004, pp. 863–868. Translated from Pis'ma v Astronomicheskiĭ Zhurnal, Vol. 30, No. 12, 2004, pp. 946–952.

Unidentified Cometary Emission Lines as the Photoluminescence of Frozen Hydrocarbon Particles

I. A. Simonia*

Abastumani Astrophysical Observatory, Georgian Academy of Sciences, Tbilisi, 380060 Georgia

Received April 12, 2004

Abstract—We discuss the possible nature of unidentified cometary emission lines. We propose a model of the ice particles in cometary halos as a mixture of frozen polycyclic aromatic hydrocarbons (PAHs) and acyclic hydrocarbons. We describe the general properties of frozen hydrocarbon particles (FHPs) and suggest interpreting some of the unidentified cometary emission lines as the photoluminescence of FHPs. We compare the positions of unidentified emission lines in the spectrum of Comet 122P/de Vico with the positions of quasi-lines in the photoluminescence spectrum of PAHs that were dissolved in acyclic hydrocarbons at a temperature of 77 K and that constituted a polycrystalline solution. We estimate the detectability of FHP photoluminescence in cometary spectra. © *2004 MAIK "Nauka/Interperiodica".*

Key words: *Solar system—planets, comets, small bodies, heliosphere; unidentified cometary emission lines; frozen hydrocarbon particles; polycyclic and acyclic hydrocarbons; photoluminescence.*

INTRODUCTION

The problem of unidentifiable cometary emission lines in the optical and other parts of the cometary spectrum is known to remain of great interest. Emission lines of this kind defy any numerical or comparative identification and are generally collected in separate tables or lists (Brown *et al.* 1996; A. Cochran and W. Cochran 2002). Successful identification of these emission lines is associated with the upgrading of spectroscopic data acquisition and processing methods, the accumulation of laboratory comparative material, and the study of other excitation mechanisms for the corresponding emission lines. Of course, unidentified emission lines can arise within the framework of the standard resonance–fluorescence mechanism through transitions from higher levels of the corresponding atoms and molecules of cometary gases. However, the possibility that the photoluminescence of solid cometary matter is excited by solar ultraviolet radiation (Churyumov and Kleshchonok 1999; Simonia 1999) should be taken into account. The probability of this process is high, particularly if the presence of an appreciable amount of an organic component in cometary ices is taken into account. Polycyclic aromatic hydrocarbons (PAHs) are known to be among the most important classes of chemical compounds encountered in various bodies in space. Their presence in cometary matter is also beyond question (Ehrenfreund and Charnley 2000).

In our view, the ices of cometary nuclei can contain mixtures of PAHs and acyclic hydrocarbons. Consequently, the ice particles of the halo that surrounds a cometary nucleus can be composed entirely of these mixtures or contain appreciable amounts of them. Solar ultraviolet radiation will excite the photoluminescence of ice particles in the halo. The low albedo of the particles composed of these mixtures and the high quantum yields of photoluminescence for PAHs ensure the detectability of the corresponding luminescent emissions.

Under low temperatures, PAHs and acyclic hydrocarbons, as well as other possible components, will be in a frozen state. We propose calling the particles of this kind frozen hydrocarbon particles (FHPs). Let us consider the FHPs and their luminescence in more detail.

FHP LUMINESCENCE

Here, we first provide information about the quantum yields of luminescence for organic compounds. Witt and Vijh (2004) point out that the quantum yield of luminescence for many organic compounds is about 50%. They also distinguish PAHs from other materials by their highly efficient luminescence and note that, in certain cases, PAHs and their ions exposed to far ultraviolet radiation are capable of emitting several luminescent photons with a total quantum yield as high as 100% after a single excitation event.

*E-mail: `iraklisimonia@yahoo.com`

D'Hendecourt *et al.* (1986) noted that the quantum yield for PAH molecules could reach 50%.

Gudipati *et al.* (2003) believe that the quantum yield for small grains containing frozen organic mixtures can vary within the range 90–100%. The aforesaid suggests that PAHs have highly efficient, intense luminescence when exposed to ultraviolet radiation. Mixtures of frozen PAHs and acyclic hydrocarbons may be contained in the ices of cometary nuclei. We assume that these mixtures are solid solvent–material solutions where by the material and the solvent we mean PAHs and acyclic hydrocarbons, respectively. In other words, the PAHs dissolved in acyclic hydrocarbons constitute a single solid solution with it. The optical properties of the solution are determined by the properties of the solvent, the solution crystallization conditions, the presence of a luminescent component (luminogen), the pattern of interaction between the components of the solution, and the content of the admixtures in the solution.

The presence of polycrystalline solutions in cometary ices is quite probable. Patashnick *et al.* (1974) and Smoluchowski (1981) showed, in particular, that amorphous ice in comets transforms into a crystal with a cubic lattice at a temperature of about 140 K. The surface layers of an ice cometary nucleus are the sources of variously sized frozen hydrocarbon particles ejected and carried away into the circumnuclear region as the heliocentric distance of the comet decreases. These ice particles of various sizes and fragment symmetry form an ice halo at the corresponding heliocentric distances. Fernandes and Jockers (1983) believe that an ice cometary halo at a heliocentric distance of $r = 1$ AU can have a radius as large as 500 km. This value is debatable, particularly if the density of the solid particles under consideration is taken into account, but it is quite acceptable for a general order-of-magnitude estimate of the halo radius. At the same time, it should be noted that space missions to comets have not yet confirmed the presence of ice halos around them. Therefore, the existence of halos of icy particles around cometary nuclei is still open to question and is considered as a hypothesis. In our view, the FHP sizes can vary from microns to millimeters. FHPs will have the color characteristic of a frozen mixture of PAHs and acyclic hydrocarbons. For low concentrations of the admixtures, the FHPs will be gray ice particles. Thus, the cometary nuclei may be surrounded by halos in the form of FHP layers. Under actual conditions, apart from FHPs, the halos may contain silicate dust and fine carbonaceous particles. When exposed to solar ultraviolet radiation and solar wind particle streams, FHPs will intensely luminesce in the wavelength range 3800–6700 Å. Other constituents of the halo (e.g., inorganic dust grains) will also luminesce, but with a lower quantum yield. The FHP luminescence spectrum will be determined by the specific chemical composition of the mixture, the PAH concentration in the polycrystalline solution, the presence or absence of admixtures, the particle temperature, the phase of solar activity, and other factors. The most important factors are the chemical composition of the specific FHP and its temperature. For chemically different FHPs with different temperatures, solar ultraviolet radiation will excite luminescence of different spectral composition. Pringsheim (1949) noted, in particular, that the diffuse spectral bands of many crystalline organic compounds at a liquid oxygen temperature of 54.3 K are resolvable into groups of narrow bands or lines. This is very important for FHPs and suggests that the ice particles of cometary halos may have luminescence spectra of at least two types: (1) spectra composed of broad diffuse bands and (2) spectra in the form of a series of narrow bands or lines. A close correlation between the types of spectra for actual FHPs and their temperatures can be found only experimentally by comparing observational and laboratory data.

Let us now describe some of the FHP properties in the temperature range 60–80 K. For this purpose, we here provide data on the laboratory FHP substance analogs. Teplitskaya *et al.* (1978) produced polycrystalline solutions of the above chemical composition to study the luminescence of PAHs at a temperature of 77 K. They showed that normal paraffins were convenient solvents for obtaining discrete PAH luminescence and absorption spectra. For compounds with a linear structure (polyacens, polyphenyls, diphenylpolyenes, etc.), the sharpest spectra are observed when the linear sizes of the solvent molecules are close to those of the PAH molecules.

Experiments indicate that highly structured hydrocarbon spectra with line widths within the range 0.15–0.47 Å can be obtained when aromatic hydrocarbon solutions are excited by laser light into the (0–0) band at $T = 4.2$ K. This is true for most of the crystallizable and vitrifiable (when frozen) solvents that are chemically neutral with respect to the molecules dissolved in them and optically transparent in the absorption and emission ranges of PAH molecules.

Experiments also indicate that the luminescence spectrum of the mixture in certain solutions at a low PAH concentration consists of a series of bands, but a series of lines can appear as the PAH concentration increases. The luminescence spectrum for pyrene with a concentration of 10^{-4} mol l^{-1} in n-pentane contains no narrow lines. Shpol'skiĭ (1962) showed that when PAHs were dissolved in special hydrocarbon (e.g., n-pentane) solvents at a temperature of 77 K or lower, a frozen mixture of these materials had a luminescence spectrum in the form of a series of many narrow lines. Such spectra are called quasi-line luminescence spectra. The positions of these lines on the wavelength scale and their mutual arrangement and relative intensities are characteristic for each molecular structure. These data can be an indicator of a normal electronic–vibrational state of the corresponding molecular structures. We assume that the FHPs of cometary halos whose chemical composition is almost identical to that of the laboratory analogs can also have quasi-line luminescence spectra when exposed to ultraviolet radiation.

At the same time, it should be noted that the quasi-line luminescence spectra of FHPs under actual astrophysical conditions can differ slightly from laboratory ones, due to the peculiar temperature and pressure conditions in cometary comas, charged particle bombardment, and collisions with the gaseous neutrals of cometary atmospheres. The width of each line in the FHP luminescence spectrum must probably be a function of the heliocentric distance, because the temperature of the cometary matter varies with heliocentric distance. The lines in the quasi-line luminescence spectra of FHPs can broaden at temperatures $T > 80$ K and low PAH concentrations. A gradual broadening of the lines in the luminescence spectra of ice particles with decreasing heliocentric distance will be observed as the FHP volatile component is depleted. Thus, for example, if the FHP material is composed of PAHs and n-hexane, the depletion begins by the time an ice particle is heated to temperature $T \approx 290$ K at which n-hexane begins to evaporate intensely. Naturally, the luminescence spectrum of the corresponding FHP will change in this case. Thus, FHPs can be produced as sources of short-lived luminescence. Short-lived emission lines of this kind are commonly detected in cometary spectra. They are often unidentified. Thus, the pattern of the FHP luminescence spectrum for cometary halos must depend on the following factors: (1) the chemical composition of the frozen mixture, (2) the PAH concentration, (3) the heliocentric distance of the comet, and (4) the dynamical peculiarities of the halo. The role of the exciting radiation whose wavelength range and intensity will differ markedly from the laboratory ones should also be noted. The ice particles that constitute the halo will be exposed to short-wavelength solar radiation of a wide range and to solar wind charged particle streams.

The photoprocessing of FHPs by solar ultraviolet radiation will change the FHP luminescence spectrum both in composition and in intensity distribution of the luminescent emission lines in series. Note that these changes will take place during a certain period that may be designated as the FHP photoprocessing period. For each class of FHP, these periods at various heliocentric distances can vary between several hundred seconds and several years.

As we see, the picture is complex and changeable; it is determined by the ice particle temperature, the PAH concentration and composition, and the composition of the exciting radiation. However, for different comets at the same heliocentric distances (e.g., $r = 1$ AU), assuming the halo ice particles to be chemically identical, similar emission lines of a photoluminescent nature will be observed in the spectra of these comets. Thus, similar, previously unidentified emission lines can be observed in the spectra of different comets. We therefore suggest interpreting some of the unidentified emission lines in cometary spectra as the photoluminescence of FHPs. We calculated the ratio of the photoluminescence flux to the scattered solar radiation flux $F_{\text{lum}}/F_{\text{sc}}$ for typical conditions of actual cometary halos composed of millimeter-size FHPs. The calculation was performed for the following conditions: the FHP is composed of phenanthrene ($C_{14}H_{10}$) + n-hexane at $T = 77$ K, and the phosphorescence line is $\lambda = 4602$ Å (Teplitskaya *et al.* 1978). We considered an FHP that scattered solar radiation with a wavelength of $\lambda = 4602.17$ Å.

According to A. Cochran and W. Cochran (2002), an unidentified emission line was observed in the spectrum of Comet 122P/de Vico at $\lambda = 4602.17$ Å.

We performed our calculations using Planck's formula and the expression for the energy exposure $E = \dfrac{(w/s)}{r^2}$ (I. Simonia and T. Simonia 2003) for $w = Ft$ (F is the flux, and t is the time), where w is the total energy of the radiation at the corresponding wavelength, s is the surface area of a halo with a radius of $R = 500$ km, and r is the heliocentric distance (1 AU). We assumed that the FHP luminescence yield was 50%, the FHP albedo was A = 0.1, and the wavelength of the exciting ultraviolet solar radiation was 2930.25 Å (the phenanthrene absorption range).

We obtained $F_{\text{lum}}/F_{\text{sc}} = 2.344$, implying that the luminescent signal lies above the scattered solar continuum as a weak but detectable emission line. Such relatively weak unidentified emission lines are widely encountered in the atlas by A. Cochran and W. Cochran (2002). The error within ±0.17 Å is small, particularly if the broadening of the corresponding lines described above is taken into account. The high quantum yield of luminescence for PAHs and the use of fast instruments and high-resolution spectrographs ensure that the luminescent signal is recognizable. We also calculated $F_{\text{lum}}/F_{\text{sc}}$ for a different millimeter-size FHP: the FHP was composed of 1.2–5.6 dibenzanthracene ($C_{22}H_{14}$) + n-hexane at $T = 77$ K, while the phosphorescence line was $\lambda = 6135$ Å (Teplitskaya *et al.* 1978); the FHP scattered solar radiation with a wavelength of $\lambda = 6135$ Å. According to A. Cochran and W. Cochran (2002), an unidentified line was observed in the spectrum of the same comet at $\lambda = 6135$ Å. We assumed that the FHP luminescence yield was 50%, the FHP albedo was A = 0.3, and the wavelength of the exciting solar radiation was $\lambda = 3660$ Å (the absorption range of 1.2–5.6 dibenzanthracene ($C_{22}H_{14}$)). Using the same formulas, we obtained $F_{\rm lum}/F_{\rm sc} = 1.552$. As we see, the luminescent signal also lies above the scattered solar continuum as a weak but detectable emission line.

COMPARATIVE ANALYSIS

We compared the laboratory luminescence spectra of FHP substance analogs with the observed cometary spectrum containing a set of unidentified emission lines. We used an atlas of quasi-line luminescence spectra for aromatic molecules (Teplitskaya *et al.* 1978) as the laboratory data and a high-resolution atlas for Comet 122P/de Vico (A. Cochran and W. Cochran 2002) as the observational data. The results obtained are summarized in the table[1]. It gives the PAH names and formulas (column 1), the solvent names (column 2), the wavelengths of the luminescent emission lines of the corresponding polycrystalline solutions (column 3), and the wavelengths of unidentified cometary emissions from the spectrum of Comet de Vico (column 4). We performed our comparative analysis with an accuracy of ±1 Å.

DISCUSSION

Having described the concept of FHP and having performed a comparative analysis of the observational and laboratory data, the results of which are summarized in the table, we conclude that at least 28 aromatic hydrocarbons that constitute a polycrystalline solution with a number of acyclic hydrocarbons may be contained in the FHPs of the ice halo of Comet de Vico as the main mixture. Naturally, the FHPs will also contain admixtures in small amounts. In fact, the ice halo of Comet de Vico may be a complex of FHPs of various chemical compositions. A cloud of variously sized FHPs with different chemical compositions exposed to ultraviolet solar radiation will be a source of luminescent emission lines within a wide wavelength range, 3800–6700 Å. The laboratory comparison data used here covered both the fluorescence and phosphorescence of hydrocarbons. The polycrystalline solutions, chemical FHP analogs, demonstrated intense fluorescence and phosphorescence under laboratory conditions.

In an actual space environment, the FHPs of cometary halos can have different afterglow periods for different excitation conditions; i.e., they can have fluorescence or phosphorescence spectra. The laboratory comparison database used here contained 100 aromatic molecules. The selection criterion that consisted in the match between the wavelengths of the corresponding emission lines to within ±1 Å completely excluded 72 molecules and about 10% of the emission lines of the 28 selected aromatic molecules. The presence of PAHs in comets was discussed by a number of authors. In particular, Moreels *et al.* (1994) showed that phenanthrene exists in the inner coma of Comet P/Halley. This aromatic hydrocarbon was detected by the above authors in the near ultraviolet range of the cometary spectrum. The authors pointed out the stability of PAHs in a space environment and a possible connection between the PAHs contained in Solar-system bodies and interstellar PAHs. Crovisier and Bockelée-Morvan (1999) believe that the presence of PAHs in comets has not yet been conclusively proven. In their extensive review, Ehrenfreund and Charnley (2000) point out the detection of PAHs and aliphatic hydrocarbons in cometary matter.

Naturally, aromatic hydrocarbons can exist in comets in both condensed and gas phases. The described FHPs of the corresponding chemical composition are the carriers of a number of previously unidentified photoluminescent emission lines. At the same time, it is quite clear that all of the unidentified emission lines cannot arise from the photoluminescence of FHPs. A significant fraction of the unidentified emission lines (perhaps most of them) are of a resonance–fluorescence nature. The sources of these emission lines are the corresponding daughter molecules and ions. Newer comparative molecular emission line databases are required for their precise identification. Thus, only a small fraction of the unidentified cometary emission lines arise from the photoluminescence of FHPs. The nature of a large number of unidentified cometary emission lines remains unknown. It is highly likely that the gaseous components of cometary atmospheres are the sources of these emission lines (Wyckoff *et al.* 1994). When calculating the ratio $F_{\rm lum}/F_{\rm sc}$, we assumed the albedos of comets to be within the range 0.1–0.3. These values were suggested by Fernandes and Jockers (1983) and several other authors. Our calculations indicate that the luminescent signal will lie above the solar continuum at various albedos due to the high quantum yield of luminescence

[1]The table is published in electronic form and is accessible via ftp cdsarc.u-strasbg.fr/pub/cats/J (130.79.128.5) or http://cdsweb.u-strasbg.fr/pub/cats/J.

Luminescence of cometary FHPs: The results of our comparative analysis

PAH			PAH			PAH		
solvent	λ, Å	λ, Å	solvent	λ, Å	λ, Å	solvent	λ, Å	λ, Å
Pyrene $C_{16}H_{10}$			Anthracene $C_{14}H_{10}$				3925	3924.82
n-Hexane	3929	3929.28	n-Hexane	3950	3950.02		3929	3929.28
	5894	5893.85		3963	3963.11		4005	4005.94
	6027	6026.66		3985	3985.44		4038	4037.93
	6036	6036.42		4011	4011.44		4041	4041.94
	6346	6346.78		4023	4023.07		4046	4046.36
	6413	6413.07		4075	4075.98		4069	4069.03
	6509	6508.71		4248	4248.06		4070	4069.97
1,2–3,4 Dibenzanthracene $C_{22}H_{14}$				4264	4263.07		4095	4094.78
n-Octane	3862	3862.07		4292	4291.73		4098	4098.31
	3936	3936.23		4490	4489.90		5910	5909.17
	3949	3949.15		4519	4519.09		5935	5935.42
	4069	4069.03	n-Heptane	3867	3867.16	1,2–5,6 Dibenzanthracene $C_{22}H_{14}$		
	4091	4090.99		3967	3967.51	n-Hexane	3936	3936.23
n-Hexane	3034	3934.90		3987	3987.26		3950	3950.02
	3955	3955.13		4002	4001.97		3953	3953.19
	3981	3981.64		4025	4024.93		4044	4044.38
	4055	4054.64		4064	4064.46		4045	4045.35
	4067	4067.35		4094	4093.94		4148	4148.93
Pycene $C_{22}H_{14}$				4295	4294.88		4195	4194.46
n-Hexane	3863	3863.16		4541	4540.82		5542	5542.40
	3871	3871.63		4573	4572.97		5942	5942.25
	3989	3989.37	Tetraphene $C_{18}H_{12}$				6013	6012.37
	3999	3999.89	n-Hexane	3884	3884.72		6096	6096.48
	4186	4186.75		3886	3886.61		6135	6135.00
1,2 Benzpyrene $C_{20}H_{12}$				3934	3934.90	1,2–4,5 Dibenzpyrene $C_{24}H_{14}$		
n-Hexane	3862	3862.07		3956	3956.48	n-Hexane	3936	3936.23
	3960	3960.05		3961	3960.05		3950	3950.02
	3959	3959.12		3963	3963.11		3953	3953.19
	4074	4073.30		3999	3999.89		4002	4001.97
	4088	4087.97		4034	4034.01		4062	4062.86
	4103	4102.98		4044	4044.38		4186	4186.75
	4195	4194.46		4047	4046.74		4621	4620.97
	4212	4212.69		4063	4062.87		4657	4656.89
	4310	4310.10		4085	4084.85		4696	4695.85
	4324	4324.09		4096	4095.93		4809	4809.87
	5366	5366.02		6415	6415.14		4888	4888.45
	5349	5349.22		6439	6438.24	Diphenil $C_{12}H_{10}$		
	5479	5479.25		6510	6509.91	n-Hexane	4371	4371.16
	5718	5718.11		6638	6638.21		4570	4570.12
	5754	5753.51	n-Octane	3891	3891.48	Fluoren $C_{13}H_{10}$		
	6016	6015.19		3909	3908.67	n-Hexane	4239	4238.71
	6351	6351.65		3912	3912.14		4525	4525.13
							4552	4552.25

for PAHs. The use of fast instruments and high-resolution spectrographs ensures the detectability of FHP photoluminescence. In fact, A. Cochran and W. Cochran (2002) and Brown *et al.* (1996) were able to detect this photoluminescence.

Caution should be exercised in interpreting unidentified cometary emission lines as the photoluminescence of FHPs, because the quasi-line spectra of polycrystalline solutions have a peculiar feature: in several cases, a group of lines (multiplets) that are often repeated over the entire spectrum corresponds to each electronic–vibrational transition in the spectrum. The existence of several types of emitting centers in different local conditions, which causes the electronic levels to shift while the positions of the vibrational sublevels remain unchanged, may be responsible for the emergence of multiplets. In addition, some of the multiplet components may be associated with the presence of closely spaced levels for the same emitting center. The pattern of the multiplet also depends on the concentration of the dissolved material, the presence of admixtures, and the solution temperature and crystallization conditions.

Here, we have not considered the formation of a frozen mixture of PAHs and acyclic hydrocarbons. We intend to devote a separate paper to this subject. It is also important to consider the bombardment of FHPs by charged particle streams. Undoubtedly, the interaction of particles with cometary FHPs will have a serious effect on the pattern of their luminescence spectrum. We also intend to adapt the concept of FHP to the interstellar medium, i.e., to consider FHPs as the particles contained in such objects as reflection nebulae, complexes of gas and dust, etc.

CONCLUSIONS

We have presented the concept of FHP and described the salient features of their photoluminescence. We suggest interpreting at least some of the unidentified cometary emission lines as the photoluminescence of FHPs. We compared the spectra of laboratory FHP analogs with the observed spectrum of Comet de Vico containing several thousand unknown cometary emission lines. The results of our comparative analysis indicate that at least 28 aromatic molecules may be contained in the ice particles of the halo of this comet.

The results of our comparative analysis are summarized in the table. In our view, it would be appropriate to devote a series of separate laboratory studies to the modeling of FHPs and the excitation of their photoluminescence and to compile a database of unidentified cometary emission lines using several atlases and catalogs of cometary spectra. We realize that this paper is only the first step in this direction, and we will attempt to develop it by continuously upgrading our methods and improving our results.

REFERENCES

1. M. E. Brown, A. H. Bouchez, H. Spinrad, and C. M. Johns-Krull, Astron. J. **112**, 1197 (1996).
2. K. I. Churyumov and V. V. Kleshchonok, Odessa Astron. Publ. **12**, 258 (1999).
3. A. Cochran and W. Cochran, Icarus **157** (2), 297 (2002).
4. J. Crovisier and D. Bockelée-Morvan, Space Sci. Rev. **90**, 19 (1999).
5. P. Ehrenfreund and S. B. Charnley, Annu. Rev. Astron. Astrophys. **38**, 427 (2000).
6. J. A. Fernandes and K. Jockers, Preprint MPAE W-82-12 (1983).
7. L. B. d'Hendecourt, A. Leger, G. Olofsson, and W. Schmidt, Astron. Astrophys. **170**, 91 (1986).
8. M. S. Gudipati, J. P. Dworkin, X. D. F. Chiller, and L. J. Allamandola, Astrophys. J. **583**, 514 (2003).
9. G. Moreels, J. Clairemidi, P. Hermine, *et al.*, Astron. Astrophys. **282**, 643 (1994).
10. H. Patashnick, G. Rupprecht, and D. W. Schuerman, Nature **250**, 313 (1974).
11. P. Pringsheim, *Fluorescence and Phosphorescence* (Intersci., New York, 1949; Inostr. Lit., Moscow, 1951).
12. E. V. Shpol'slkiĭ, Usp. Fiz. Nauk **77**, 250 (1962).
13. I. Simonia, *Comments on Modern Physics. Comments on Astrophysics* (1999), Vol. 1, Part E, p. 25.
14. I. Simonia and T. Simonia, Astron. Astrophys. Trans. **22** (1), 55 (2003).
15. R. Smoluchowski, Astrophys. J. Lett. **244**, L31 (1981).
16. T. A. Teplitskaya, T. A. Alekseeva, and M. M. Val'dman, *An Atlas of Quasi-Line Spectra of Aromatic Molecules* (MGU, Moscow, 1978) [in Russian].
17. A. N. Witt and U. P. Vijh, ASP Conf. Ser. (2004, in press).
18. S. Wyckoff, R. Heyd, and A. Ferro, Bull. Am. Astron. Soc. **26**, 1418 (1994).

Translated by V. Astakhov